

Thin film growth of isotropically and
anisotropically interacting particles with lattice
KMC simulations

Dissertation

der Mathematisch-Naturwissenschaftlichen Fakultät
der Eberhard Karls Universität Tübingen
zur Erlangung des Grades eines
Doktors der Naturwissenschaften
(Dr. rer. nat.)

vorgelegt von
Eelco Empting
aus Borken

Tübingen
2022

Gedruckt mit Genehmigung der Mathematisch-Naturwissenschaftlichen Fakultät
der Eberhard Karls Universität Tübingen.

Tag der mündlichen Qualifikation: 04.11.2022

Dekan: Prof. Dr. Thilo Stehle

1. Berichterstatter: Prof. Dr. Martin Oettel
2. Berichterstatter: Prof. Dr. Roland Roth

Declaration of collaborative publications

Lattice gas study of thin-film growth scenarios and transitions between them: Role of substrate

E. Empting, M. Klopotek, A. Hinderhofer, F. Schreiber, and M. Oettel
Phys. Rev. E 103, 023302 (2021)

For this paper, I performed all the presented simulations. M. Klopotek was responsible for guiding the research and helping with research questions. A. Hinderhofer and F. Schreiber were responsible for the section regarding the comparison to experimental results. The rest of the thesis was co-written by M. Oettel and me.

Thin film growth of phase-separating phthalocyanine-fullerene blends: A combined experimental and computational study

B. Reisz, E. Empting, M. Zwadlo, M. Hodas, G. Duva, V. Belova, C. Zeiser, J. Hagenlocher, S. Maiti, A. Hinderhofer, A. Gerlach, M. Oettel, and F. Schreiber
Phys. Rev. Mat. 5, 045601 (2021)

For this paper, M. Oettel performed the presented simulations and B. Reisz performed the experiments. I analyzed the simulation data and together with M. Oettel wrote the part of the manuscript regarding the simulation results. The other authors supported B. Reisz in the experimental part of the paper.

Interplay of orientational order and roughness in simulated thin film growth of anisotropically interacting particles

E. Empting, N. Bader, and M. Oettel
Phys. Rev. E 105, 045306 (2022)

For this paper, I performed most of the presented simulations. The simulations of the equilibrium system were performed by N. Bader. M. Oettel and I co-wrote the manuscript.

Abstract

We performed the simulation studies presented in this thesis with the goal of better understanding the behavior of a thin film growing on a substrate. We used the Kinetic Monte Carlo (KMC) method to simulate cubic particles on a cubic lattice using two different approaches: One in which neighboring particles interact isotropically and one where nearest-neighbor interactions were anisotropic.

The KMC method is widely used to study the temporal evolution of non-equilibrium systems. Here we use it first to study the growth of a film when cubic particles are deposited onto a substrate comprised of a different material. Specifically, we compare two models: The well-known solid-on-solid (SOS) model, in which no cavities are allowed to form inside the film, and a newly developed colloidal growth model (CGM). In the CGM, particles are allowed to desorb from the film into the gas phase, and possibly re-adsorb at a different site, leading to the formation of cavities and overhangs.

We find that in the intermediate regime ($\mathcal{O}(10)$ monolayers), the systems will show one of several growth modes, depending sensitively on the ratios of inter-particle interaction to substrate interaction and diffusion speed to deposition rate. Specifically, the film can initially either wet the substrate or desorb from it. The point of the transition between these two modes is shifted with respect to the equilibrium value, hence we call this a dynamic layering transition. At longer times, the roughness of an initially dewetting film will decrease. The main difference between the models is whether the film will become completely smooth or retain a constant roughness. For $t \rightarrow \infty$, each film will eventually roughen, independent of the initial growth mode. Finally, we tie these findings together into a global phase diagram denoting the possible growth modes and the conditions for their occurrences. Comparison to experimental data shows a good qualitative agreement in the general growth modes.

The main goal of such simulations is the comparison to experimental results. Since the previous model is extremely simplified (isotropic particles and interactions), it is not suitable to explain many phenomena occurring during the growth of films of anisotropic organic molecules, e.g. ordering of particles. Thus we extend the model by implementing anisotropic interactions between particles. Each particle now had an internal orientation, and the interaction strength now depended on the orientations and relative positions of neighboring particles. These interactions can be implemented to either model disc-shaped molecules (e.g. benzene) or rod-shaped molecules (e.g. pentacene).

Here we find two new ordering transitions upon increasing η , the strength of the anisotropy, with the film first going from an unordered phase to one in which two orientations dominate, and finally to one in which the third species starts dominating. The point of the first transition is close to the equilibrium value, while the second transition is a non-equilibrium one. At low values of η , before the second transition, the ordering

behavior of the film is independent of the film growth mode, which depends on the energetic and kinetic parameters. For strong values of η , the change in ordering coincides with a very strong roughening of the film, which is due to the occurrence of long needles perpendicular to the substrate. We again tie these results together in a dynamic phase diagram, and comparison to experimental results now shows good agreement concerning the ordering behavior of many real-world molecules.

Finally, we explore the behavior of mixed films consisting of particles of two species: An anisotropically and an isotropically interacting one. These simulations were performed specifically to model the behavior of a 1:1 mixed film of CuPC and C₆₀.

Zusammenfassung

Die in dieser Dissertation vorgestellten Simulationsstudien wurden durchgeführt, um das Verhalten wachsender dünner Filme auf einem Substrat zu untersuchen. Mithilfe kinetischer Monte-Carlo-Simulationen (KMC) wurden würfelförmige Teilchen auf einem kubischen Gitter modelliert, jeweils mit isotropen und anisotropen Wechselwirkungen.

KMC-Simulationen sind ein häufig genutztes Werkzeug zur Untersuchung des dynamischen Verhaltens von Nichtgleichgewichtssystemen. In diesen Simulationen nutzten wir sie, um zu untersuchen, wie ein Dünnsfilm wächst, wenn würfelförmige Teilchen auf ein Substrat bestehend aus einem anderen Material aufgedampft werden. Wir konzentrieren uns hier auf zwei Modelle: Das klassische, vielgenutzte *solid-on-solid*-Modell (SOS), in dem weder Überhänge noch Löcher im Film erlaubt sind, und ein neuartiges Modell, das *colloidal growth model* (CGM). Im CGM können Teilchen vom Film desorbieren, in der Gasphase diffundieren und eventuell an anderer Stelle auf dem Film wieder adsorbieren. Dies führt zur Entstehung von überhängen und Löchern im Film.

Bei der Untersuchung mitteldicker Filme ($\mathcal{O}(10)$ Monolagen) zeigt sich, dass solche Filme in verschiedenen Wachstumsmodi wachsen können, abhängig von den energetischen und kinetischen Parametern. Zum Einen kann der wachsende Filme anfänglich entweder das Substrat benetzen oder Inseln auf diesem bilden. Der Punkt, an dem der Übergang zwischen diesen beiden Wachstumsmodi stattfindet, ist verglichen mit dem Gleichgewichtswert verschoben. Aus diesem Grund nennen wir dies eine *dynamic layering transition*. Für längere Depositionszeiten wird die Rauigkeit eines rau wachsenden Films zunächst wieder sinken. Der Hauptunterschied zwischen den beiden Modellen ist hier, ob der Film komplett glatt wird oder zu einem konstanten Rauigkeitswert geht. Wenn die Zeit $t \rightarrow \infty$, wird jeder wachsende Film aufrauen, unabhängig von der ursprünglichen Wachstumsart. Die hier aufgezählten Befunde vereinigen wir schließlich in einem globalen Phasendiagramm der unterschiedlichen Wachstumsmodi und zeigen auf, unter welchen Bedingungen diese auftreten. Im Vergleich mit experimentellen Befunden zeigen sich gute qualitative Übereinstimmungen bei den möglichen Wachstumsmodi.

Das Ziel solcher Wachstumssimulationen ist üblicherweise der Vergleich mit experimentellen Befunden. Da das bisher verwendete Modell sehr vereinfacht ist (isotrope Teilchen mit isotropen Wechselwirkungen), ist es nicht geeignet, um komplexere Phänomene, die während des Wachstums eines Films von anisotropen organischen Teilchen auftreten, zu beschreiben. Zu solchen zählt z.B. langreichweitige Ordnung der Teilchen. Aus diesem Grund erweiterten wir das Modell um anisotrope Wechselwirkungen zwischen Teilchen. Jedes Teilchen hatte nun einen internen Orientierungsvektor, und die Stärke der Wechselwirkung zwischen zwei Teilchen hing von ihren Orientierungen und relativen Positionen ab. Die Anisotropie wurde so gewählt, dass entweder scheibenförmige (z.B. Benzen) oder stäbchenförmige (z.B. Pentacen) Moleküle abgebildet werden konnten.

In diesen Simulationen fanden wir zwei neue Ordnungsübergänge, welche auftreten, wenn η , die Stärke der Anisotropie, erhöht wird. Zunächst ist der Film ungeordnet, dann dominieren zwei Orientierungen und schließlich dominiert die dritte Orientierung. Der erste Übergang ist nah am Gleichgewichtsübergang, während der zweite ein deutlicher Nicht-Gleichgewichtsübergang ist. Bei niedrigen Werten von η , vor dem zweiten Übergang, ist das Ordnungsverhalten der Teilchen unabhängig vom Wachstumsmodus. Für starke η geht jedoch die Änderung der Ordnung mit einem starken Anstieg der Rauigkeit einher. Dies geschieht aufgrund der Bildung langer Nadeln senkrecht zum Substrat. Abschließend vereinigen wir die Ergebnisse in einem dynamischen Phasendiagramm und zeigen, dass diese sehr gut zu den experimentellen Befunden passen.

Abschließend untersuchen wir das Verhalten gemischter Filme, bestehend aus einer anisotrop und einer isotrop wechselwirkenden Spezies. Diese Simulationen wurden speziell durchgeführt, um einen 1:1 gemischten Film bestehend aus CuPC und C₆₀ zu modellieren.

Contents

1. Introduction	1
1.1. Motivation	1
1.2. Overview of film growth simulation models	2
1.3. Experimental methods and materials	4
1.4. Structure	5
2. Theory of thin film growth	7
2.1. Sub-monolayer growth	8
2.2. Film growth modes	11
2.2.1. Equilibrium growth modes	12
2.2.2. Kinetic growth modes	13
2.3. Asymptotic roughening	15
2.4. Concluding remarks	16
3. Monte Carlo methods	17
3.1. Lattice gas	17
3.2. General Monte Carlo principles	18
3.3. Metropolis Monte Carlo	19
3.4. Kinetic Monte Carlo	20
4. Wetting and phase transitions	25
4.1. The Ising model	25
4.2. The wetting transition	25
4.3. Landau theory	27
5. Isotropic interactions	31
5.1. Models	31
5.2. Observables	33
5.3. Parameter scaling	34
5.4. Results	37
5.4.1. Dynamic layering transition	37
5.4.2. Flattening transition	43
5.4.3. Asymptotic growth behavior	48
5.4.4. Non-zero E_{ES}	49
5.4.5. Global growth mode diagram	51
5.5. Comparison to experiments	53
5.6. Conclusion	54

6. Anisotropic interactions	57
6.1. Model	57
6.2. Effective Ehrlich-Schwoebel barrier	59
6.3. Observables	60
6.4. Mean-field calculations	60
6.4.1. 3D	61
6.4.2. 2D	64
6.5. Simulations	67
6.5.1. Growth modes	69
6.5.2. Equilibrium transition	70
6.5.3. Non-equilibrium transition	72
6.6. Model variations	77
6.6.1. Strongly interacting substrate	77
6.6.2. Rod-like interactions	78
6.7. Comparison to experiments	79
6.8. Conclusion	81
7. Binary systems	83
7.1. Species-dependent Ehrlich-Schwoebel barrier	84
7.2. Anisotropic interactions - preliminary results	88
7.3. Conclusions and outlook	92
8. Outlook	97
8.1. Rejection-free KMC	97
8.2. No hop restrictions	97
8.3. Anisotropic particles	98
8.4. Post-growth effects	99
9. Summary and conclusion	101
Appendices	103
A. Very strong anisotropies in model B	105
B. Binary system snapshots	107
C. Landau theory for a three-component system in 2D with an external field	111
Bibliography	113

Chapter 1.

Introduction

1.1. Motivation

Film growth occurs when particles are deposited on top of a substrate, forming a continuous surface. The exact conditions and materials used in such experiments can vary wildly, hence the range of applications of such grown films is very large, from solar cells to coatings and electronic circuits. Specifically, we will be interested in thin films consisting of organic molecules. Such organic thin films have been a topic of great interest in the last decades. Due to the semiconducting nature of many organic molecules, they are suitable for a wide array of applications, ranging from organic solar cells to organic LEDs[1]. While such devices are inferior to their inorganic counterparts in terms of e.g. efficiency and stability, they are cheaper to produce and can be manufactured to be e.g. semi-transparent or flexible[2, 3].

The properties of such grown films (e.g. the solar cell efficiency or conductivity) depend sensitively on the morphology and composition, hence the ability to precisely control these is a research area of significant interest. The structural properties of the film, in turn, depend on the growth conditions (substrate temperature, deposition rate) and materials (of both film and substrate) employed.[4]

Predicting the final morphology of a growing film for a certain set of growth conditions is no easy task. Such films are many-particle systems, typically consisting of millions of particles, and are grown under non-equilibrium conditions. Analytical descriptions of processes during film growth so far have been mainly limited to either the use of rate equations to describe the sub-monolayer regime (described in more detail further down) or to scaling arguments for sub-monolayers and very thick films. Scaling arguments are used to describe how observables, e.g. the height-height correlation function or island densities, are proportional to powers of other variables, e.g. temperature or deposition speed. While these are invaluable tools for the study of short- and long-term behavior, their use in predicting the behavior of films for intermediate thicknesses is limited. There are some models using rate equations to study thin films in this regime[5], however, these can be only applied to specific systems (in this case, homoepitaxial growth) and do not yield any structural information.

Apart from these analytical studies, there is of course a large corpus of experimental and simulation work. From previous experiments, one can then empirically predict how a film will grow under certain conditions. In experiments, however, it is difficult to (1) systematically study the influence of microscopic parameters and (2) investigate the

in-situ evolution of certain observables. In simulations, these problems are relatively easy to solve. However, when developing a simulation model for a real-world system, simplifications need to be made. This might mean e.g. using unrealistic kinetic conditions or the omitting of critically important system properties, leading to behavior completely different from that observed in the real system. If the necessary care is exercised, however, these simplified models can yield crucial insights into the growth process.

The focus in such simulation studies has again been mainly on sub-monolayer or on long-term behavior, not on the intermediate growth regime. This regime is however of critical importance for the final morphology, since during this time particles will form clusters (or domains in binary systems), the size and shape of which then influences the behavior of particles arriving afterwards. In this work, we present a generic model for deposition of particles on a substrate of a different material. This model is then compared to experimental results for film growth of organic semiconductors. We will focus mostly on the intermediate regime, trying to understand the processes at play during structure formation and categorize the phenomena.

1.2. Overview of film growth simulation models

As already indicated, it is no easy task to formulate a microscopic theory for films larger than the sub-monolayer. It is therefore no surprise that simulation studies of thin film growth have been an invaluable tool in furthering the understanding of the general principles of film growth[6]. In this section, we try to give an overview of the evolution of film growth models. Note that this section is by no means exhaustive.

The simplest realization a film growth model (apart from the sub-monolayer models) is one in which the simulation box is divided into discrete lattice cells forming a simple cubic lattice. Films are then grown by assuming the lowest layer to be filled, forming a substrate, and successively inserting new particles from the top into the simulation box and letting them diffuse down. These are usually called ballistic deposition models[7].

Ballistic deposition models can (as far as the author is aware) be traced back to the works of Vold[8, 9] in the 1950s. In the simplest realization of these models, new particles are inserted at the top of the box and diffuse down until they either reach the substrate or land on an already settled particle. Since in such models the individual columns are independent of each other, the roughness σ of the film will grow as $\sigma \propto \Theta^{1/2}$ [10], where Θ is the number of deposited monolayers and σ is defined as

$$\sigma = \sqrt{1/N \sum_{i=1}^N (h_i - \bar{h})^2} \quad (1.1)$$

with N being the number of lattice sites, h_i the film height at lattice site i and \bar{h} the average height of the film. Films produced in this way are compact, i.e. each particle is supported by either another particle or the substrate. Such a model is called a *solid-on-solid model*. A slightly more involved (off-lattice) model is the one used by Vold, where downward diffusing particles come to rest as soon as they come into contact with

1.2. Overview of film growth simulation models

any other particle, not only if they land on top of one. In contrast to the solid-on-solid models, it is here possible for cavities to occur inside the film. This is called a *ballistic aggregation model*; the most famous of these is probably the Eden model[11]. As a variation of these models, it is also possible for particles to not diffuse downward perpendicularly to the substrate, but at an angle θ [12], leading to shadowing of columns by other columns blocking the flux.

All of these models have in common that particles will remain at their initial position after coming to rest. In real films, however, particles will usually diffuse around after deposition, either due to the kinetic energy of the downwards motion or general thermal diffusion. Thus it is necessary to extend these models. An early extension was the Wolf-Villain model[13, 14], where particles will diffuse for some distance immediately after deposition before becoming immobilized. This is a useful approximation for the processes occurring e.g. during molecular beam epitaxy of metallic thin films, where particles arrive at the substrate with a considerable kinetic energy. Similarly, in models with different lattice geometries (e.g. fcc), a particle would need multiple particles in the layer below to fully support it. Consequently, in such models an often invoked mechanism is downward funneling[15], where a particle which is not fully supported after deposition will diffuse downward until it reaches a site where all supporting sites are occupied. This leads to films growing in a much smoother fashion than those grown under a simple cubic geometry. As an aside, this model has also been modified such that downward diffusing particles can also be trapped at the sides of protrusions, leading to overhangs and eventually cavities inside the film, making this more akin to a ballistic aggregation model[16].

The next logical extension of film growth models is to incorporate particle diffusion not only immediately after deposition, but as long as a particle is not buried by other particles. This is realized by setting an insertion probability p , and during each time step either inserting a new particle with probability p or moving an existing particle with a probability $1 - p$. The first realization of this was the Clarke-Vvedensky model[17, 18]. The probabilities here depend on the ratio of the insertion flux F and the diffusion rate D as defined in Eq. 3.11.

In all the models presented so far, there has been no distinction between the interaction of particles with the substrate and the inter-particle interaction, i.e. we have assumed films to grow on a substrate of the same material. For the investigation of very long time scales, the exact nature of the substrate is irrelevant, since as soon as the substrate is completely covered, the film will effectively grow like it would on a substrate of the same material (due to the usual short-ranged nature of the substrate-interaction)[19, 20]. However, for the short to medium term morphological evolution of the thin film, the exact nature of the substrate plays a crucial role. For the growth of a thin film on a substrate of a different material, work has been done investigating elastic strain and subsequent stress release[21, 22, 23] and for strain-free systems by modeling specific materials, e.g. C₆₀ on Pentacene[24]. These approaches can be used to e.g. determine the energetic parameters of a system by fitting the simulation data to experimental results.

The simple models presented in the previous paragraphs are of course very abstract and thus cannot capture many of the effects seen in thin film growth. Due to this, they have

been extended further in order to describe investigate certain phenomena found in film growth, by e.g. introducing patterned substrates[25, 26, 27, 28, 29, 30, 31], simulating co-deposition of two particle species[32], introducing anisotropic interactions[33, 34] or anisotropically shaped particles[35].

1.3. Experimental methods and materials

On the other hand, of course, the measure against which simulation results are judged are results obtained in film growth experiments. In such experiments, a plethora of deposition methods and materials are used. Deposition methods include e.g. various vapor evaporation methods, sputtering, plasma processes, and chemical vapor deposition.[36]

In particle deposition film growth[37], the substrate is usually placed in a liquid phase in which colloidal particles (e.g. proteins or polymers) are suspended. These particles then diffuse downwards due to e.g. attractive energies between substrate and particles or hydrodynamic flow. This leads initially to the aggregation of particles on the substrate and subsequently the growth of a thick, usually porous film. This deposition method is the inspiration for the colloidal growth model, which we will describe later in this work.

Growth by evaporation, on the other hand, is usually conducted either in a vacuum chamber or under normal pressure. The main methods on which we focus here are molecular beam epitaxy (MBE) and chemical vapor deposition (CVD). In CVD, material of one species is heated, particles go into the gas phase, diffuse towards the substrate and react chemically with the substrate material. CVD is a versatile deposition procedure used for many applications, e.g. the production of solid state circuits.[36]

MBE, on the other hand, is a purely physical deposition process, used to grow single-crystal films under high vacuum conditions. A so-called *Knudsen effusion cell* is used to heat the material. Particles then sublime and diffuse in a directed beam towards the substrate. Here, the distinction between organic and inorganic must be pointed out: While for inorganic materials this method is called MBE, for organic molecules one usually uses the term organic molecular beam deposition (OMBD), since here epitaxy¹ does not necessarily play a role[38].

The distinction between organic and inorganic films is crucial. Inorganic thin films are usually grown by the deposition of atoms, which are more or less isotropic and very small, with a strong interaction between particles. Inorganic thin films are rigid and stable at high temperatures. Organic thin films, on the other hand are grown by deposition of larger molecules, e.g. pentacene or C₆₀. These molecules are often anisotropic, which means that molecular ordering has to be considered, and interact relatively weakly.

The nature of the substrate on which the film is grown will also significantly influence its final morphology. The main distinction here must be made between amorphous and crystalline substrates. Crystalline substrates have a crystal structure, the exact symmetry of which depends on how the material was cut. A structured substrate can lead to strained growth of crystalline thin films if the lattice constants or lattice symmetry are not exactly

¹The term epitaxy is used to describe the growth of crystalline films on top of crystalline substrates; organic films may, however, also grow amorphously

matched, eventually leading to the film breaking up. At short times, the structure of the surface may lead to adatoms forming needle-shaped clusters along the structure of the substrate[39, 40]. Amorphous substrates have no lattice structure. There, the film growth mode is mainly determined by interaction energies and the exact growth conditions.

As can already be seen, a wide variety of parameters plays a role during thin film growth. These can typically not be varied easily during experiments, which is where simulations come into play. Simulation models are typically simplified, focusing only on some aspects of the film growth process. While this allows us to more precisely investigate the effects of certain parameters, special care has to be exercised in the interpretation of the results from such studies.

1.4. Structure

This thesis is structured in the following way: In the first few chapters, we summarize the theoretical basics necessary to understand the context and implications of the results. The following chapters then contain descriptions of simulation results which we have already published in scientific journals, as well as some results which were not fleshed out enough to warrant publication. Finally, we present possible future avenues for research.

Chapter 2.

Theory of thin film growth

Thin film growth occurs when particles (usually atoms or small molecules) are deposited onto a substrate comprised of either the same or a different material. The structure of the resulting film (e.g. roughness, local composition) crucially depends on the employed materials, kinetic and energetic parameters and shapes of the particles.

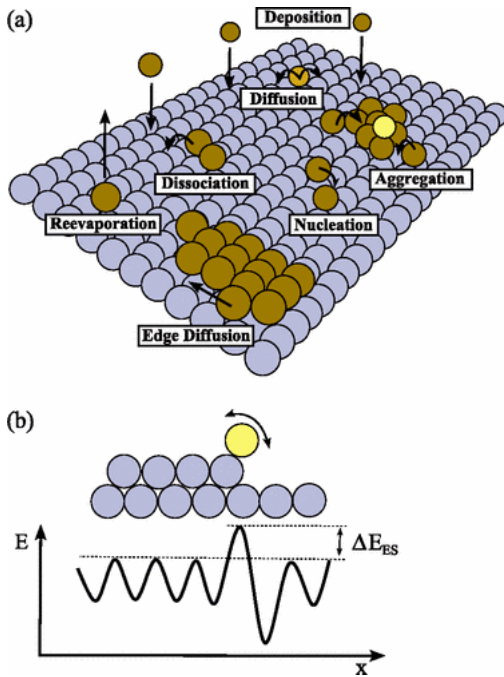


Figure 2.1.: (a) Schematic particle moves during the film growth process. (b) Ehrlich-Schwoebel barrier for interlayer diffusion. Source: Fig. 1 from Ref. 41

Particles are deposited onto the substrate and subsequently diffuse around until they are eventually buried. In Fig. 2.1(a) we show a schematic detailing a (non-exhaustive) variety of possible diffusion processes, including e.g. nucleation of single particles into islands, dissociation of islands, and re-evaporation of particles into the gas phase. Particles can also “hop up” or “hop down” between different layers, as shown for the yellow particle in Fig. 2.1(b). Such inter-layer hopping processes are usually energetically less favorable than diffusion within a layer, due to the loss of nearest-neighbors when detaching from the original layer. This energetic barrier is called the Ehrlich-Schwoebel barrier[42, 43], denoted in literature as ΔE_{ES} , E_{ES} , or E_s .

The Ehrlich-Schwoebel barrier and the strengths of interactions between two particles and between a particle and the substrate are the relevant energetic parameters in this film growth system, while the deposition rate F and the rates of different kinds of diffusion (most notably the surface diffusion rate D) are the main kinetic parameters. The value of D depends on the temperature as $D = D_0 \exp(-E_D/k_B T)$, where E_D is the diffusion barrier, D_0 is the attempt frequency, k_B the Boltzmann constant, and T the temperature. The value of D_0 can be obtained by e.g. transition state

theory[44] or density functional theory[45]. Often, one just uses the value introduced by Clarke and Vvedensky[46]. , $D_0 = \frac{2k_B T}{h}$, where h is the Planck constant. Another note has to be made regarding the substrate: In this work, we will be mainly concerned with perfectly smooth and homogeneous substrates. While substrates in experiments may contain e.g. impurities or steps[10] which significantly influence the diffusion behavior of deposited particles, our aim is to first understand the general principles of film growth.

The growth of a thin film can be roughly divided into three stages:

1. **Sub-monolayer regime:** During the initial stages of film growth, at coverages $\ll 1$ monolayer, the formation of the first islands takes place, the shapes and sizes of which are determined by the growth parameters and in turn influence the structure of the film upon continued deposition.
2. **Intermediate regime:** After the initial islands have formed and a few monolayers of material have been deposited, the structure of the thick film starts to emerge. It may become very smooth or rough and show different kinds of ordering behavior.
3. **Long-term regime:** Upon continued deposition of particles, the roughness behavior of film will eventually increase monotonically as a power of the coverage. This scaling behavior then falls into one of several universality classes.

We will investigate each of these three regimes in more detail in the following sections.

2.1. Sub-monolayer growth

During the initial stages of film growth, single particles will diffuse around on the substrate, bind to other particles to form islands and possible break those bonds again. To understand the dynamics of these nucleation processes, one can take inspiration from classical nucleation theory (CNT), which is a very general, albeit simplistic[47], model for the formation of clusters[48].

The central finding of CNT is that for a cluster to be stable and continue growing, it has to reach a certain critical size, otherwise it is energetically more favorable to decompose the cluster. Thus we similarly assume that in thin film growth, once a certain number of particles has formed an island, this island will not dissociate anymore and instead continue growing. It is usual to denote as i or i^* the size of the largest island which is *not* stable.

Following Refs. [10, 41, 49] (see these works for more details), the dynamics of island formation can be described using rate equations. In these, we describe the concentrations n_s of clusters consisting of s atoms (n_2 is the dimer density etc.). Assuming now that islands of size $s > 1$ are immobile, growth and shrinkage of a island of size s can only occur by attachment/detachment of a monomer to/from the island. The rate at which the concentration n_s changes is then

$$\frac{dn_s}{dt} = \Gamma_s - \Gamma_{s+1} \quad (2.1)$$

2.1. Sub-monolayer growth

where Γ_s is the net formation rate for a cluster of size s . These rates can be written as

$$\Gamma_s = \sigma_{s-1} D n n_{s-1} - K_s n_s \quad (2.2)$$

where D is the monomer diffusion rate, n the monomer density, σ_s the capture number for an island of size s , and K_s the rate of detachment of a monomer from an island of size s . The capture number is a dimensionless quantity and denotes the ability of an island to capture monomers. The net formation rate for an island of size s is thus simply the rate at which monomers attach to islands of size $s-1$, minus the rate at which monomers detach from islands of size s .

Monomers arrive on the substrate with a rate F and attach to and detach from existing islands. The change in monomer density n is then

$$\begin{aligned} \frac{dn}{dt} &= F - 2\Gamma_2 - \sum_{s>2} \Gamma_s \\ &= F - 2D\sigma_1 n^2 - Dn \sum_{s=2}^{\infty} \sigma_s n_s + 2K_2 n_2 + \sum_{s=3}^{\infty} K_s n_s \end{aligned} \quad (2.3)$$

Similarly, from Eqs. 2.1 and 2.2 it follows that the change in density of islands of size s can be written as:

$$\frac{dn_s}{dt} = D\sigma_{s-1} n n_{s-1} - D\sigma_s n n_s + K_{s+1} n_{s+1} - K_s n_s \quad (2.4)$$

These equations are impossible to solve without some simplifying assumptions. Foremost, as indicated earlier, we will now assume that any island of size $s > i$ is stable, i.e. $K_s = 0$ for $s > i$. We are then only interested in the total number of stable islands, $N = \sum_{s=i+1}^{\infty} n_s$. Additionally, one usually replaces σ_s for $s > i$ by an averaged

$$\bar{\sigma} = \frac{1}{N} \sum_{s=i+1}^{\infty} \sigma_s n_s \quad (2.5)$$

Assuming now that the number of unstable islands is quasi-stationary (islands of size $s \leq i$ decompose quasi immediately, i.e. $\Gamma_s = 0$) yields from Eq. 2.2:

$$K_s n_s \approx \sigma_{s-1} D n n_{s-1} \quad \text{for } s \leq i \quad (2.6)$$

which yields

$$n_s \propto n^s \quad \text{for } s \leq i \quad (2.7)$$

due to the recursive nature of this equation. To solve Eq. 2.6 for n_s , the process of monomer detachment has to be considered in more detail. For a monomer to detach from an island of size s , it has to overcome both the binding energy to the island and a diffusion barrier. The binding energy is $E_s - E_{s-1}$, where $E_s > 0$ is the energy necessary to decompose a cluster of size s into monomers (hence $E_1 = 0$). We can then write K_s as

$$K_s = \mu_s D \exp \left[\frac{-(E_s - E_{s-1})}{k_B T} \right] \quad (2.8)$$

with $D = D_0 \exp[-E_D/k_B T]$ and $\mu_s = \text{const}$. Inserting this into Eq. 2.6 yields:

$$\begin{aligned} n_s &\approx \frac{\sigma_{s-1} D n n_{s-1}}{K_s} \\ &= \frac{\sigma_{s-1}}{\mu_s} n \frac{n_{s-1}}{\exp\left[\frac{-(E_s - E_{s-1})}{k_B T}\right]} \end{aligned} \quad (2.9)$$

all energies up to E_{s-1} again cancel out due to the recursive nature of the equation, leading to the Walton relations[50],

$$n_s \approx b_s \exp[E_s/k_B T] n^s \quad \text{for } s \leq i \quad (2.10)$$

where $b_s = \prod_{i=1}^{s-1} \sigma_i / \mu_{i+1}$.

Using the considerations so far, the change in the monomer density is then:

$$\frac{dn}{dt} = F - (1 + \delta_{i,1}) \sigma_i D n n_i - \bar{\sigma} D n N \quad (2.11)$$

New monomers arrive with a rate F and attach to islands of size $s \geq i$. For $s < i$, attachment and detachment rates cancel out while for $s \geq i$ there is no detachment from the resulting island. The change in the density of stable islands, N , follows then from Eq. 2.4 as ($K_s = 0$ for $s > i$):

$$\begin{aligned} \frac{dN}{dt} &= \sum_{s=i+1}^{\infty} \frac{dn_s}{dt} = \sum_{s=i+1}^{\infty} D \sigma_{s-1} n n_{s-1} - D \sigma_s n n_s \\ &= D \sigma_i n n_i \end{aligned} \quad (2.12)$$

Assuming the ratio $\Gamma \equiv D/F \rightarrow \infty$, we can solve for N via the scaling ansatz:

$$n(\Gamma, \Theta) \propto \Gamma^{-\zeta} n_{\infty}(\Theta) \quad (2.13)$$

$$N(\Gamma, \Theta) \propto \Gamma^{-\chi} N_{\infty}(\Theta) \quad (2.14)$$

where n_{∞} and N_{∞} are the monomer and island densities in equilibrium, respectively, $\chi, \zeta > 0$ and Θ is the layer coverage. First, Eqs. 2.11 and 2.12 can be written to depend on Θ and Γ via:

$$\begin{aligned} \Theta &= Ft \\ \Gamma &= \frac{D}{F} \\ \frac{d}{d\Theta} &= \frac{\Gamma}{D} \frac{d}{dt} \end{aligned}$$

Using the Walton relation from Eq. 2.10, this yields:

$$\frac{dn}{d\Theta} = 1 - (1 + \delta_{i,1}) \sigma_i b_i \exp[E_i/k_B T] \Gamma n^{i+1} - \bar{\sigma} \Gamma n N \quad (2.15)$$

$$\frac{dN}{d\Theta} = \Gamma \sigma_i b_i \exp[E_i/k_B T] n^{i+1} \quad (2.16)$$

Inserting the ansatz from Eqs. 2.13 and 2.14 then yields:

$$\Gamma^{-\zeta} \frac{dn_\infty}{d\Theta} \propto 1 - (1 + \delta_{i,1}) \sigma_i b_i \exp[E_i/k_B T] \Gamma^{1-(i+1)\zeta} n_\infty^{i+1} - \bar{\sigma} \Gamma^{1-\zeta-\chi} n_\infty N_\infty \quad (2.17)$$

$$\Gamma^{-\chi} \frac{dN_\infty}{d\Theta} \propto \sigma_i b_i \exp[E_i/k_B T] \Gamma^{1-(i+1)\zeta} n_\infty^{i+1} \quad (2.18)$$

Comparing the coefficients, we thus find that $\chi + \zeta = 1$ and $\chi = (i+1)\zeta - 1 = \frac{i}{i+2}$. For the last term in Eq. 2.17 to become 1 and from Eq. 2.18 it additionally follows that:

$$n_\infty = \frac{1}{\bar{\sigma} N_\infty} \quad (2.19)$$

$$\frac{dN_\infty}{d\Theta} = \sigma_i b_i \exp[E_i/k_B T] n_\infty^{i+1} \quad (2.20)$$

Using $N_\infty(0) = 0$, Eqs. 2.19 and 2.20 lead to:

$$N_\infty(\Theta) = \left(\frac{(i+2) \sigma_i b_i \exp[E_i/k_B T]}{\bar{\sigma}^{i+1}} \Theta \right)^{1/(i+2)} \quad (2.21)$$

and consequently:

$$N(\Gamma, \Theta) \propto \left[\frac{(i+2) \sigma_i b_i}{\bar{\sigma}^{i+1}} \Theta \right]^{1/(i+2)} e^{E_i/(i+2)k_B T} \Gamma^{-i/(i+2)} \quad (2.22)$$

The most important result from this equation is that island densities scale with $N \sim \Theta^{1/(i+2)} \Gamma^{i/(i+2)}$, i.e. the island density at different coverages can be identical, provided the ratio Γ is scaled accordingly.

As indicated earlier, one usually assumes $i = 1$, i.e. that any island formed by two or more particles is stable and will not decompose. This means consequently that $E_i = 0$, i.e. the island density does not depend on the strength of inter-particle interactions ϵ . However, this assumption only holds true if $\epsilon \rightarrow \infty$. Usually in simulations and experiments, the strength of inter-particle interactions is finite, meaning that $i > 1$. This significantly complicates the form of the scaling relation. More importantly, this means that the island density now also depends on the strength of inter-particle interactions, since now also $E_i \neq 0$.

2.2. Film growth modes

As the film becomes thicker, its structure emerges. The film may be either flat or become rough, by forming islands or by different mechanisms.

Before explaining the growth modes in more detail, it is necessary to introduce the concept of epitaxy. Epitaxy in general means the oriented growth of one crystal on top of another.[51] In principle one distinguishes between homo- and heteroepitaxy. **Homoepitaxy** indicates that film and substrate material are identical. Typically (but not always) this leads to rather smooth films. **Heteroepitaxy** conversely indicates that the two are comprised of different materials. This can lead to a wide variety of growth modes, depending on the ratios of interaction strengths, lattice mismatch etc.

2.2.1. Equilibrium growth modes

Before investigating the structure of films in non-equilibrium, it is instructive to first describe the usual equilibrium approach using thermodynamic growth modes. These modes are divided into three categories[52]:

- **Vollmer-Weber growth:** Interactions between particles are stronger than those between particles and substrate. The particles will form tall, weakly-wetting islands on the substrate. This leads to very rough films.
- **Frank-van-der-Merwe growth:** The particles will form a perfectly smooth film; new layers will only start growing if the layer below is completely filled.
- **Stranski-Krastanov growth:** A hybrid of the two other modes. The film will initially grow in a layer-by-layer fashion, before eventually breaking up due to strain and forming islands.

Typically, it is said that Vollmer-Weber (VW) and Stranski-Krastanov (SK) growth occur during heteroepitaxy, while Frank-van-der-Merwe (FM) growth occurs during homoepitaxy. The distinction between VW and FM (and also SK) growth is then made using an equilibrium force balance argument.

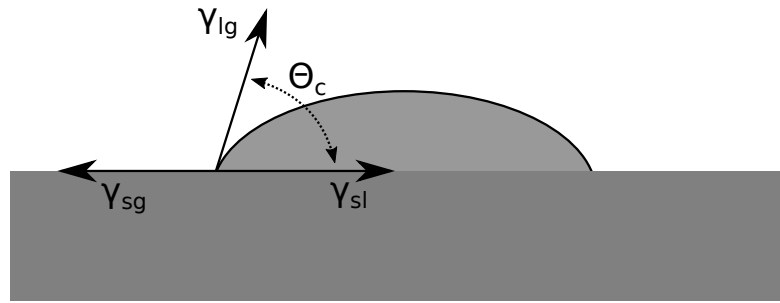


Figure 2.2.: Schematic representation of the force balance determining the contact angle of a droplet on a substrate. The γ are the free energy costs of the interfaces and Θ_c the contact angle of the droplet

In Fig. 2.2 we show a liquid droplet on a substrate. γ_{sg} denotes the free energy cost of the solid-gas interface, γ_{lg} that of the liquid-gas interface, and γ_{sl} that of the solid-liquid interface. Θ_c is the contact angle of the droplet. According to Young's equation[53], force equilibrium is achieved if

$$\gamma_{sg} = \gamma_{lg} + \gamma_{sl} \cos \Theta_c \quad (2.23)$$

The thin films we are interested in are not liquid. However, since at relatively high temperatures the film particles can freely re-arrange their positions, Young's equation can also be used to describe the wetting behavior of such films. Smooth and rough films

can then be distinguished by their contact angles:

$$\text{Frank-van-der-Merwe : } \Theta_c = 0 \Rightarrow \gamma_{\text{sg}} = \gamma_{\text{lg}} + \gamma_{\text{sl}}$$

$$\text{Vollmer-Weber : } \Theta_c > 0 \Rightarrow \gamma_{\text{sg}} < \gamma_{\text{lg}} + \gamma_{\text{sl}}$$

i.e. for a film to form islands ($\Theta_c > 0$), the substrate-liquid interface must be highly unfavorable. In the thin film growth scenario, this corresponds to film particles interacting more strongly with each other than with the substrate, favoring compact clusters over a flat, spread-out film. While this is a useful phenomenological description, we will show in this work how the distinction becomes significantly more complicated in the non-equilibrium scenario.

The intermediate case of Stranski-Krastanov growth occurs when the film material differs from the substrate material, both film and substrate are crystalline, and the lattice constants of film and substrate differ. In this case, it is initially favorable for the film to grow flat, but due to the mismatch in lattice constants a strain builds up, which eventually at a critical film thickness “tears apart” the film, leading to strong roughening in higher layers.

2.2.2. Kinetic growth modes

As already mentioned, the previously introduced growth modes are highly idealized. They should be viewed as limiting cases in the equilibrium scenario. Real-world film growth, however, does not necessarily occur close to equilibrium. During the process of deposition a plethora of diffusion processes can occur, all at different rates compared to the deposition speed.

Here it is useful to distinguish between atomic and molecular thin films. Atomic thin films usually consist of metal or semiconductor atoms, while molecular thin films usually consist of organic molecules (e.g. pentacene or most famously C_{60}). Metal and semiconductor atoms are more or less isotropic and exhibit relatively strong interaction. Organic molecules, on the other hand, are comparatively large, anisotropic, and interact relatively weakly via van-der-Waals and possible electrostatic interactions.

Homoepitaxy

In non-equilibrium homoepitaxial growth, following Michely and Krug[10], one can schematically distinguish four idealized growth modes for *atomic thin films*. For these modes, it is assumed that the substrate is not perfectly flat, but instead includes a certain amount of steps. This is a reasonable inclusion for modeling experimental data, since the formation of such steps is not trivial to avoid when preparing a substrate.

The growth modes are shown in Fig. 2.3:

- **Step flow growth:** Occurs at high temperatures. This leads to the formation of a single island within each plane which attaches to existing steps but does not form new steps. Due to this mechanism, the steps are merely moving within the plane.

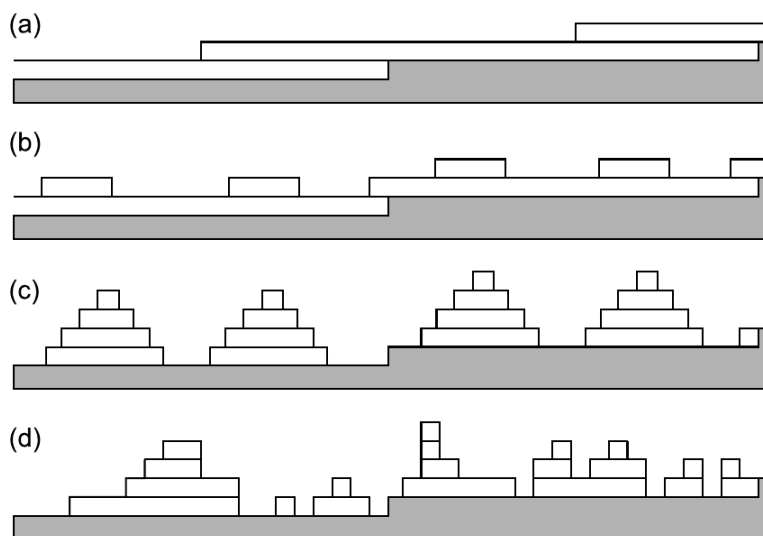


Figure 2.3.: Idealized growth modes in non-equilibrium homoepitaxial growth. These are (a) Step flow growth, (b) layer-by-layer growth, (c) mound formation, and (d) self-affine growth. Source: Fig. 4.1 from Ref. 10

- **Layer-by-layer growth:** Occurs at slightly lower temperatures. Multiple islands will now form within each plane, coalescing as the plane is filled. Islands will only start growing when the layer below is completely filled, leading to an oscillating roughness evolution. This can, however, only occur if interlayer transport is not inhibited
- **Mound formation:** Occurs when interlayer transport is inhibited. Particles cannot hop down in order to fill the layers below, instead forming new islands on top. This leads to the formation of very rough films
- **Self-affine growth:** At very low temperatures, particles cannot diffuse anymore and are confined to their initial position. Films grown in this way are very rough, showing a random and self-similar morphology.

While homoepitaxial organic thin films will often exhibit more or less the same growth modes as atomic thin films[54], the shape anisotropy can play a role in the evolution of the morphology. Pentacene thin films can e.g. exhibit step flow growth, while the individual layers can be rotated with respect to each other[55]

Heteroepitaxy

When films are grown heteroepitaxially in non-equilibrium conditions, the number of parameters influencing the manner in which the film grows increases further.

In atomic thin films, strain due to lattice mismatch plays an important role, leading to very rough films with a wide variety of morphologies[56].

Organic thin films will show an even wider variety of morphologies, depending on their shape and the exact substrate. Disc-shaped molecules (like phthalocyanines, benzene or perylene) will often form needles or stacks which on amorphous substrates (e.g. SiO₂) will grow in parallel to the substrate[57], while on ordered (metallic) substrates the needles will grow perpendicular to the substrate[58, 59, 60]. Such needles can occur throughout the whole film[61] or only within the first layer[62].

Rod-shaped molecules (e.g. pentacene or DIP) might grow standing up on the substrate[63, 64, 65, 66, 67] or lying down[63, 68].

As can already be seen from these examples, there is no easy classification for the growth modes of organic thin films, due to the wide variety of shapes and substrate interactions.

2.3. Asymptotic roughening

As the film becomes thicker, it will always eventually start to roughen. Deposition of new particles is not perfectly uniform and instead shows random fluctuations. These fluctuations then have to be smoothed out via surface diffusion of particles, which occurs at finite speeds. The driving force behind this smoothing out is the gradient of the free energy of the interface between film and gas phase (In the absence of deposition and for $t \rightarrow \infty$, the surface of the film will become smooth).[69]. Family and Vicsek found[70] that the roughness evolution can be described by the finite-size scaling expression

$$\sigma(L, \Theta) \sim \Theta^\beta f(L/\Theta^{1/z}) \quad (2.24)$$

where $f(x)$ is the scaling function

$$f(x) \sim \begin{cases} x^\alpha & \text{for } x \ll 1 \\ \text{const.} & \text{for } x \gg 1 \end{cases} \quad (2.25)$$

, L is the lateral size of the system, Θ is the average film thickness in monolayers, α and z are the scaling exponents and $\beta = \alpha/z$.

Depending on the exact values of the parameters α and z , growth can then be divided into one of several universality classes.

The roughening of the film surface can be described by a Langevin equation of the form

$$\frac{\partial h}{\partial t} = K(\nabla h, \nabla^2 h, \dots) + \delta F(\vec{r}, t) \quad (2.26)$$

where h is the local height of the film, K is a function of the derivatives of h and δF is the random noise of deposition. Depending on which powers of ∇h are included and on their respective power (pre-factors are irrelevant; this is known as power counting), the Langevin equation then describes different universality classes for long-term roughening. The most important universality classes[10] are shown in Tab. 2.1.

Most prominent here is the Kardar-Parisi-Zhang universality class[71], which is thought to encompass many growth models, including the solid-on-solid (SOS) model[72].

Class	α	z
Kardar-Parisi-Zhang	≈ 0.4	≈ 1.6
Edwards-Wilkinson	0	2
conserved KPZ	$\approx 2/3$	$\approx 10/3$
Mullins	1	4

Table 2.1.: Universality classes for the asymptotic evolution of film roughness on a two-dimensional substrate

A special case of this roughening is when the local roughness, defined as the square root of the height-height correlation function, scales with a value of α different from the one of the global roughness. This is then called **anomalous roughening**[73]. The consequence of this is that in some cases, α and z may not be sufficient to describe the universality class of the roughness, but an additional parameter α_{loc} is needed.

2.4. Concluding remarks

From these sections it should be obvious that while the sub-monolayer and the long-term regime have been studied in great detail and can be described by mathematical models, no such model exists for the intermediate regime.

For the description of the intermediate regime, there exist merely qualitative descriptions of growth modes and general parameter regions for their occurrences. The aim of this work is to start filling this gap.

Chapter 3.

Monte Carlo methods

3.1. Lattice gas

Thin films consist of many individual particles, often on the order of 10^6 . The question is of course how to most efficiently simulate such a many-body system. When trying to analyze physical many-body systems, there are two main methods which are often used: Monte Carlo (MC) and molecular dynamics. Molecular dynamics methods work by explicitly calculating the forces acting upon each particle (e.g. attraction to or repulsion from other particles) and then moving particles according to Newton's laws of motion. The advantage of MD simulations is that they include the full particle dynamics and thus in general yield accurate results. For this to work, however, the length of each time step has to be chosen to be very short, and since force calculations are computationally very expensive, MD simulations are usually limited to short timescales. Often, however, interesting dynamics only occur at relatively long timescales.

This problem can be solved by exploiting fundamental properties of such systems: During thin film growth, particles are deposited onto the substrate or the growing film. Once there, they will diffuse around before being eventually buried. When forming the film, the particles will in many cases arrange in a periodic lattice structure. This leads to subsequently deposited particles "seeing" an energy landscape consisting of periodically arranged energy minima. Movement of the particle thus consists of diffusion around an energetic minimum, before it will eventually cross a saddle point and "fall" into the next energetic minimum. This process is shown schematically in Fig. 3.1.

This insight lead to the development of the lattice gas model[75]: Particles can only reside on discrete lattice sites, and diffusion consists of discrete jumps between neighboring sites. In most implementations, each lattice site can only be occupied by one particle (hard-core repulsion), and particles may interact attractively with particles on neighboring lattice sites. The Hamiltonian of a configuration X in such a lattice gas system is then

$$H(X) = \sum_{i,j} \epsilon_{ij} n_i n_j \quad (3.1)$$

where i, j are lattice sites, $n_\alpha = 1$ if a site is occupied and 0 otherwise, and

$$\epsilon_{ij} = \begin{cases} \epsilon & \text{if } i \text{ and } j \text{ are nearest neighbors} \\ 0 & \text{otherwise} \end{cases} \quad (3.2)$$

the interaction strength between particles, usually in units of $k_B T$, with $\epsilon < 0$.

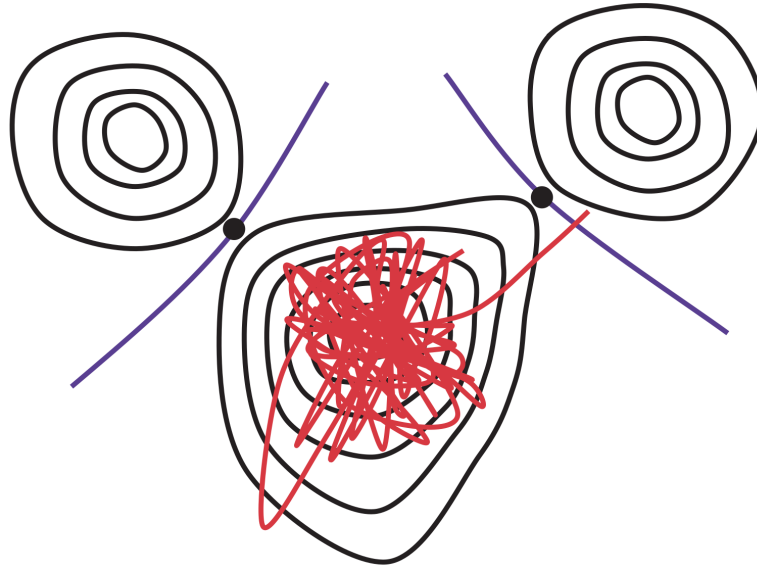


Figure 3.1.: Schematic contour plot of particle diffusion (red line) within an energy landscape (black lines). The particle will initially diffuse around the energy minimum, until it randomly passes the saddle point and falls into the next energy basin. Source: Fig. 1 from Ref. 74

The Monte Carlo method, which is usually used to solve equilibrium problems, can then be used to model the non-equilibrium problem of diffusion by performing random jumps of particles between lattice sites.

3.2. General Monte Carlo principles

The core of the MC method is the solution of multi-dimensional integrals. The integral of a function f is calculated as $\int d\Gamma f(\Gamma)w(\Gamma)$ by drawing random numbers Γ according to the probability distribution w and calculating the average value of f . [76]

An often used introductory example [77] is the estimation of the value of π by integrating the function

$$f(x, y) = \begin{cases} 1 & \text{for } x^2 + y^2 \leq 1 \\ 0 & \text{otherwise} \end{cases} \quad (3.3)$$

drawing random numbers from the probability distribution

$$w(s) = \begin{cases} 1 & \text{for } 0 \leq s \leq 1 \\ 0 & \text{otherwise} \end{cases} \quad (3.4)$$

Such a uniform distribution is however only useful for problems in which the area of interest is relatively large compared to the sample space. In physical many-particle systems, the number of interesting and allowed configurations is very small compared to

the number of possible configurations. Creating the corresponding distribution w is an impossible task, hence for this one often uses the Metropolis algorithm[78]

3.3. Metropolis Monte Carlo

The general idea of the Metropolis algorithm is, when simulating a system, to sample each configuration X (e.g. a set of positions of interacting particles or the spin distribution in the Ising model) according to its Boltzmann probability[79]

$$P(X) = \frac{1}{Z} \exp(-E(X)/k_B T) \quad (3.5)$$

where $Z = \sum_X \exp(-E(X)/k_B T)$ is the partition function of the system, and $E(X)$ is the internal energy of the system in the configuration X . Sampling configurations this way and averaging a function, we can thus calculate the equilibrium value of this function (e.g. pair correlation function in a system of colloids).

The partition function of any sufficiently complex system cannot be reasonably known, however. To circumvent this problem, Metropolis et al. proposed a scheme in which a not-forbidden initial state is generated and subsequent states then chosen according to a transition probability W . This is an example of a *Markov chain*, in which new states are generated without memory of any previous states except the current one[80]. Transition from one state to the next might e.g. be flipping a spin in the Ising model or randomly moving a particle by a small Δr .

A system evolving in such a way will then eventually reach the equilibrium distribution if the transition probability W fulfills the detailed balance condition

$$P(X)W(X \rightarrow X') = P(X')W(X' \rightarrow X) \quad (3.6)$$

where $W(X \rightarrow X')$ is the probability for the system to go from configuration X to X' , and can be written as

$$W(X \rightarrow X') = g(X \rightarrow X')A(X \rightarrow X') \quad (3.7)$$

where g is the probability for the move $X \rightarrow X'$ to be proposed and A the probability for this move to be accepted. The Metropolis choice for the acceptance probability is

$$A(X \rightarrow X') = \min \left(1, \frac{P(X')g(X \rightarrow X')}{P(X)g(X' \rightarrow X)} \right) \quad (3.8)$$

Assuming symmetric proposal probabilities g and using Eq. 3.5, we thus obtain:

$$A(X \rightarrow X') = \min (1, \exp(-\Delta E)) \quad (3.9)$$

where ΔE is the change in internal energy this move would cause.

Thus the Metropolis algorithm is:

1. Initialize system in state X
2. For N steps:
 - a) Create random next state X'
 - b) Calculate the change in internal energy $\Delta E = E(X') - E(X)$
 - c) Generate a random number $p \in [0, 1)$
 - d) If $p < \exp(-\Delta E/k_B T)$ then $X \leftarrow X'$

It should be noted that this method is typically used for the simulation of systems in equilibrium. An exception here is the dynamic Monte Carlo (DMC) method, which can be used to model e.g. the temporal evolution of a system of colloids[81, 82]. However, this method is only exact in the limit of very small particle moves, i.e. short time steps[81]. During film growth, a large variety of processes can occur, the speeds of which can span several orders of magnitude. To accurately model this using DMC, the length of a time step would have to be small enough to accommodate the fastest processes, leading to potentially very long simulation times.

3.4. Kinetic Monte Carlo

The most commonly used MC method which can be used to ameliorate the problem of time scales and simulate the temporal evolution of dynamical systems is kinetic Monte Carlo (KMC)[83, 84].

As noted earlier, MD simulations can be used to accurately model the temporal evolution of dynamical systems, but suffer from the problem that only small systems ($\lesssim 1000$ particles) and short times ($\lesssim 10^{-6}$ s) can be investigated, due to the need for time steps short enough to capture atomic vibrations ($\mathcal{O}(10^{-15})$ s). The key insight in the development of the KMC method was that for the investigation of long-term diffusive behavior, it is usually not necessary to model short-time vibrations around an energy minimum, and that it is sufficient to model the diffusion of a particle as discrete jumps between energy minima[74]. Compared to e.g. DMC, this leads to a significant speedup of simulations, since only concrete events have to be simulated. Hence KMC is called an *event driven* method.

In Fig. 3.1 we show this schematically. The particle will randomly diffuse around the energy minimum, until it passes the saddle point and falls into the next energy basin. Since the energy barrier between two minima is usually on the order of several $k_B T$, a significant amount of simulation time is used to explore the basin, all of which does not matter for the eventual hop into the next basin. In a KMC simulation, we only model particle movement as jumps between the basins. This saves a significant amount of simulation time compared to MD simulations. However, it is now necessary to choose which moves (i.e. jumps between energy minima) must be implemented. Apart from hops to neighboring sites on a substrate, we also have to consider e.g. rotations of anisotropic

particles and under which conditions they should be allowed (check whether a rotation would be blocked by another particle). The choice which moves to include can here be guided by the use of MD simulations[85].

We define then as all possible states only those where particles are located at minima in the free energy landscapes (i.e. the lattice gas model), where each move from a state i to a state j occurs *on average* with a rate k_{ij} . The change of $P_i(t)$, the probability for a particle to be in state i , can then be described by the Markovian master equation[86]

$$\frac{dP_i(t)}{dt} = - \sum_{j \neq i} k_{ij} P_i(t) + \sum_{j \neq i} k_{ji} P_j(t) \quad (3.10)$$

It is, however, unfeasible to solve this equation for any interesting system. Instead, we treat the jump from a state i to a state j as a Poisson process with an average waiting time $\tau_{ij} \equiv k_{ij}^{-1}$, since the time at which the particle crosses the energy barrier is effectively random. This allows us to randomly evolve the system one jump at a time, making KMC an *event driven* method.

In order to determine the rates k_{ij} for the different moves, one often used approach is transition state theory (TST)[87], where one takes the rate constant k_{ij} to be the equilibrium flux through the surface dividing states i and j , i.e. we count the number of crossings of this surface and divide it by the total number of trajectories at state i . While this approach can yield good results, it is rather elaborate. For the simulation of diffusing particles on top of a substrate, for example, one often rather uses the Clarke-Vvedensky bond counting ansatz[46]

$$k_{ij} = \frac{2k_B T}{h} \exp\left(-\frac{E_D + n_i E_B}{k_B T}\right) \quad (3.11)$$

where $E_D > 0$ is the diffusion barrier, n_i the number of nearest neighbors the hopping particle has in state i , and $E_B > 0$ the nearest-neighbor interaction between particles. Another approach is to use molecular dynamics simulations in order to determine the rates of possible moves[85].

The total rate at which the system tries to leave a state i is

$$K_i = \sum_{j \neq i} k_{ij} \quad (3.12)$$

and the average time the system spends in state i is K_i^{-1} [74]. To evolve the system from state i to a new state j , we randomly choose one move from a list of all currently possible moves[88], as shown in Fig. 3.2. For this, we create a list of all possible transitions, with the weight of each entry being proportional to its rate. We then generate a uniform random number r in the range $(0, K)$ and choose the transition j for which

$$\sum_{l=0}^j k_l \leq r < \sum_{l=0}^{j+1} k_l \quad (3.13)$$

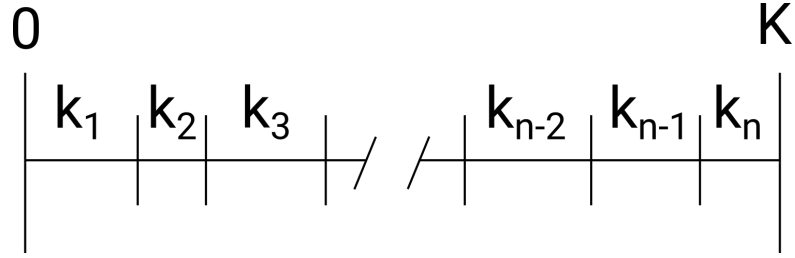


Figure 3.2.: Linearized list of all possible transitions from a current state, the length of each box being proportional to its rate k_i . To choose a move, we choose an item from this list with a probability proportional to its length $P = k_i/K$

To be more concrete: In a lattice model where each particle occupies one lattice site, state i is a given configuration denoted by which lattice sites are occupied by a particle. Transitions from state i to different states are realized by either (1) inserting a new particle into the system (at a random site), (2) an already existing particle hopping to an unoccupied neighboring site, or (if we perform a 3D simulation) (3) a particle hopping on top of a neighboring particle or hopping down from a particle into the layer below (see the following chapter for schematic diagrams of these moves). After a move is chosen with its corresponding probability, the list of all possible moves is of course different, and subsequently K might also be different.

Before pulling everything together into the final algorithm, some remarks must be made regarding the length of each time step. As indicated earlier, the average length of each time step can be calculated to be $\tau_{\text{av}} = K^{-1}$. This has however been found to lead to inaccurate dynamics[89]. Due to the jumps being Poisson processes, it is more accurate to draw the length of each time step from a Poisson distribution with an average time K^{-1} , i.e. $p(\tau) = K \exp(-K\tau)$. Instead of drawing from this exponential distribution, it is easier to draw a number from a uniform distribution and transform it using the inverse transform sampling method[90]. This yields for the length of the time step:

$$\tau = -\frac{\ln r}{K} \quad (3.14)$$

with r being a uniformly distributed random number in the range $(0, 1)$. Finally, pulling everything together, we can summarize the general KMC algorithm as shown in Alg. 3.1. As can be seen there, the KMC algorithm is rejection-free, in the sense that it is guaranteed that during each time step, a move will be performed.

```

Initialize list of all possible moves
Set simulation time  $t = 0$ 
while Stop condition is not met do
    Calculate  $K$ 
    Calculate length of timestep  $\tau$  according to Eq. 3.14
     $t \leftarrow t + \tau$ 
    Make linearized array of all rates
    Draw  $r \in (0, K)$ 
    Choose move  $j$  according to Eq. 3.13
    Execute move  $j$ 
    Update list of all possible moves
end

```

Algorithm 3.1: Kinetic Monte Carlo algorithm

This rejection-free implementation is however not suitable for every kind of simulation. Depending on the exact model, the calculation of K can be a significant bottleneck, especially in systems with many classes of moves. If we calculate the rates as shown in Eq. 3.11, we have to inspect the local environment of each particle at each time step in order to calculate $n_i E_B$. If the number of particles in the system becomes large and each particle has to be considered at all times, the number of necessary calculations quickly explodes.

To ameliorate this, it is possible to combine the KMC algorithm with a Metropolis step, leading to the so-called hybrid KMC method[89]. This is akin to splitting the interactions into two parts, repulsive and attractive. Instead of investigating the local environment of each particle, we only calculate k using the (constant) diffusion barrier, which would lead the rate in Eq. 3.11 to become

$$k_{ij} = \frac{2k_B T}{h} \exp\left(-\frac{E_D}{k_B T}\right) \quad (3.15)$$

i.e. the rates are constant and identical for all moves of the same class.

Thus, in order to calculate K , we only have to know *how many* moves of each class are allowed (not forbidden due to hard-core repulsion) at the current time. To then account for the attractive interactions, each move is accepted with the Metropolis probability from Eq. 3.9. Whether or not the proposed move is accepted, the time is still advanced by the random time step length.

Note also that the resulting dynamics are now subtly different from those in the CV model: Instead of only inspecting the local environment of a particle to determine the rates, we now inspect the initial and target environment to determine whether a move is allowed. Consequently, implementing this hybrid KMC method using CV kinetics would lead to a move acceptance probability

$$P_{CV} = \exp\left(-\frac{n_i E_B}{k_B T}\right) \quad (3.16)$$

which also fulfills the detailed balance condition of Eq. 3.6.

While this hybrid KMC method speeds up the simulation in some respects, it of course also leads to possible moves being rejected due to being energetically unfavorable, potentially wasting a significant amount of simulation time. Thus one must carefully choose which of the two methods is better suited for the task at hand. Further down in this work, we present two different simulation models, for both of which we used the hybrid KMC method. This was done due to the fact that for one model (the Colloidal Growth Model; see later) the number of degrees of freedom was excessively large, which would have made the rejection-free KMC method prohibitively slow. For the other model, we suspect that a rejection-free implementation would have been significantly faster. In order to be able to compare the results of both models, however, we also used the hybrid KMC method there.

Chapter 4.

Wetting and phase transitions

4.1. The Ising model

The Ising model is the simplest, most widely known lattice model used to study phase behavior, originally developed to study ferromagnets[91]. The model consists of a d dimensional lattice, where each lattice site is occupied by either a spin-up (+1) or a spin-down (-1). Next-neighbor spins interact with a strength $E_{ij} = s_i s_j J$, where s_i and s_j are the values of spins i and j , respectively, and J is the coupling strength in units of $k_B T$. Additionally, one often introduces an external magnetic field h , which couples to each spin with a strength $h_i = h \cdot s_i$, i.e. the Hamiltonian of this system is

$$\frac{H}{k_B T} = -J \sum_{i,j} s_i s_j - h \sum_i s_i \quad (4.1)$$

where i, j are nearest-neighbor sites. Upon increasing the value of J , the system will show a first-order transition going from a state in which both spins are equally likely to one in which one orientation dominates. The exact value J_c at which this transition occurs was found for the 1D system by Ising, while the exact solution for the 2D system was found by Onsager[92]

Since sites in the Ising model can only have one of two possible states, it is easy to map a state in this model to one in the lattice gas[93], e.g. by assigning spin-down to an unoccupied site and spin-up to an occupied site, which leads to

$$s_i = 2n_i - 1 \quad (4.2)$$

where $n_i \in [0, 1]$ denotes whether a lattice site is occupied or not. Using Eqs. 3.1 and 4.1, it becomes obvious that the energetic parameters can be mapped as

$$\epsilon = -4J \quad (4.3)$$

The ordering transition in the Ising model then becomes a gas-liquid transition.

4.2. The wetting transition

Binder and Landau[94, 95] studied a variation of the Ising model in 3D. They considered systems of size $L \times L \times D$ lattice sites, with the upper and lower boundaries being free

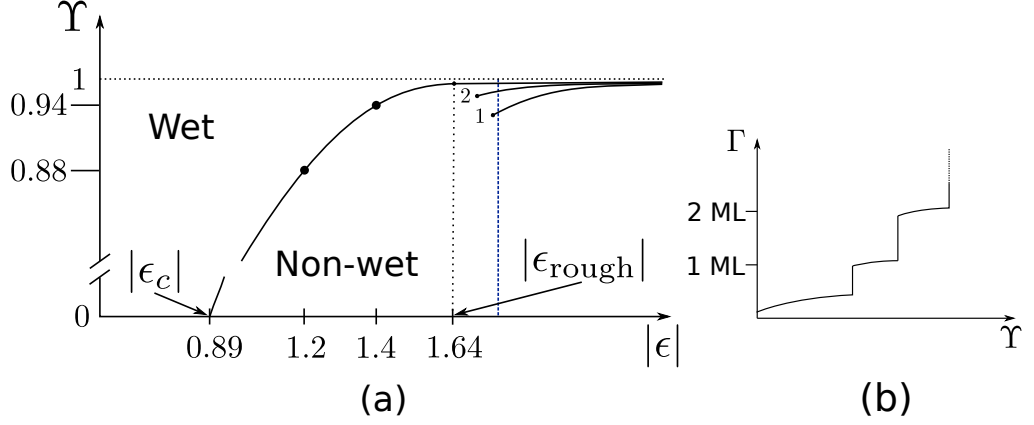


Figure 4.1.: (a) Schematic equilibrium wetting diagram for a 3D lattice gas model for $\Upsilon \equiv \epsilon_{\text{sub}}/\epsilon$. Starting at $\epsilon = \epsilon_c$, gas-liquid separation can occur and the system will show a wetting transition (infinitely thick films for Υ above this line, films of finite thickness below the line). For $|\epsilon| \geq |\epsilon_{\text{rough}}|$, the film will show roughening. For higher values of $|\epsilon|$, the layering transition occurs, where films of thickness 1 or 2 monolayers will occur before the film grows infinitely. The data points are from Ref. [94]. (b) Schematic depiction of the adsorption Γ as a function of Υ along the blue dashed line in (a).

surfaces of size $L \times L$. In these layers, neighboring spins interacted with strength J_s , while in the bulk they interacted with strength J . Thus here the Hamiltonian was

$$H = -J \sum_{\text{bulk}} s_i s_j - J_s \sum_{\text{surfaces}} s_i s_j - H \sum_i s_i - H_1 \sum_{\text{surfaces}} s_i \quad (4.4)$$

They found that this seemingly simple model shows complex phase behavior. As had been found earlier, the system would show a wetting transition. In the context of this version of the Ising model, wetting means that, starting from the free surface, all spins will be oriented in parallel (this orientation wets the free surface) and growing on from there, all spins will assume this orientation. Another view of this phenomenon is that the interface between “adsorbed phase” and mixed bulk phase becomes unbound from the free surface and distances itself infinitely from there. This transition can be either first or second order. In the lattice gas model, the corresponding transition would be an infinite accumulation of particles on a substrate.

In addition to this, two other transitions are important in the context of this work: The layering and the roughening transition. Given the right parameters, in the layering transition neighboring layers of spins will be re-ordered successively, instead of in the whole system at once. The roughening transition occurs when steps in the surface cost free energy to create, leading to a rough interface between the ordered region and the unordered region.

Translating the parameters from Ref. [94] to the lattice model via:

$$\epsilon = -4J \quad (4.5)$$

$$\epsilon_{\text{sub}} = -2J - 2H_1 \quad (4.6)$$

we can construct the phase diagram shown in Fig. 4.1. For $|\epsilon| \lesssim 0.89$, no film will form, since this is below the critical gas-liquid separation value ϵ_c ($J_c \approx 0.22$ in the 3D Ising model[96]). Relevant for the following discussions of thin film growth and the dynamic layering transitions is the fact that for the values of ϵ which we investigated during the course of this work ($|\epsilon| > 3$), the value of Υ for the wetting transition is ~ 1 , i.e. in an equilibrium lattice gas with moderately strong interactions, wetting will occur only when $|\epsilon_{\text{sub}}| > |\epsilon|$

4.3. Landau theory

Landau theory[97] provides a simplified model to describe ordering transitions. It is mainly used to describe e.g. the phase behavior of liquid crystals. The following considerations mainly follow Ref. [98]; see there for more details.

The basis of Landau theory is the assumption is that the behavior of a certain order parameter Q close to the transition point can be described by a single function, which is a free energy. This free energy F can be represented as a function of some thermodynamic variables (e.g. particle number N , volume V , and temperature T) and the order parameter Q . Often, one uses the free energy density $f(\rho, T; Q) = F/V$, where $\rho = N/V$ is the particle density. Landau theory then starts with expanding F in terms of Q :

$$F(N, V, T; Q) = F_0(N, V, T) + a_2 Q^2 + a_3 Q^3 + a_4 Q^4 \quad (4.7)$$

This expansion is typically only performed up to the fourth term, since the value of Q is small close to the transition point. The equilibrium state (i.e. the value of Q at given values of N , V , and T) is then the value at which F becomes minimal. Since Eq. 4.7 describes an ordering transition, i.e. a transition between different values of Q , some conditions for a_2 can be derived: In the derivative $\partial F/\partial Q$, it is the lowest coefficient, and thus should change its sign upon the phase transition when varying T . The phase transition then occurs at the point where $a_2(N, V, T) = 0$. This temperature is usually denoted as T_c . Considering a given pressure p , an equation that fulfills these conditions is:

$$a_2(N, V, T) = a(T - T_c) \quad (4.8)$$

where $a = (\partial a_2/\partial T)_{T=T_0}$. If an external field is applied, the free energy gains an additional term $-a_1 Q$, where a_1 is the strength of the external field.

The transitions we can describe using this free energy are usually between a state in which $Q = 0$ and one in which $Q \neq 0$. Such transitions are said to be either first or second order.

In Fig. 4.2 we show the difference between first and second order transitions. A system prepared at a certain $T > T_c$ will be unordered, i.e. at $Q = 0$. If the system is now cooled

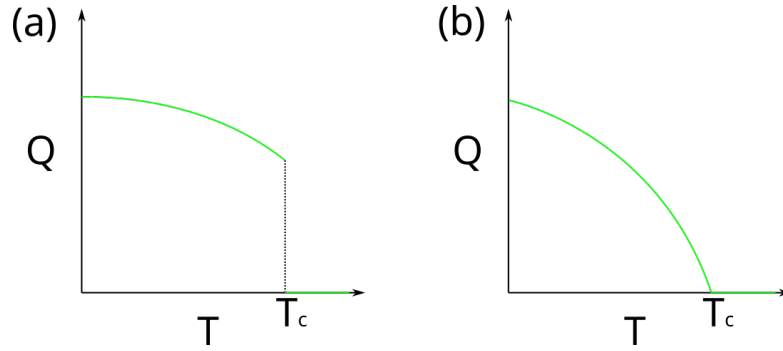


Figure 4.2.: Order parameter Q during (a) first order and (b) second order phase transitions

down, upon reaching T_c a transition will occur. A first order transition, as shown in Fig. 4.2(a), occurs when Q is discontinuous at $T = T_c$, while a second order transition, as shown in Fig. 4.2(b), will exhibit a discontinuity in its first derivative.

The origins of these transitions become clear when examining the free energy near the phase transition:

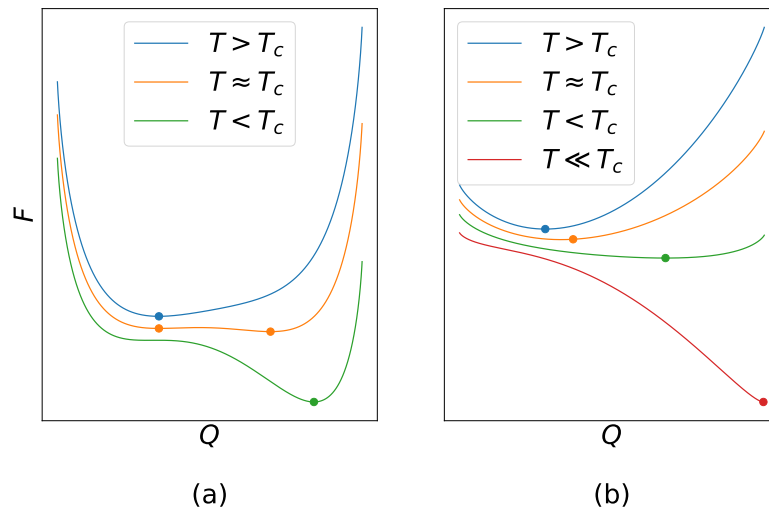


Figure 4.3.: Free energy close to the critical temperature exhibiting (a) a first order and (b) a second order phase transition. Markers denote the absolute minima of the respective free energies.

In Fig. 4.3(a) we show schematically a free energy for a system exhibiting a first order transition. For $T > T_c$, the free energy has one minimum, which corresponds to the stable composition. At $T \approx T_c$, the free energy has two minima at the same height. This indicates a coexistence between two phases at the corresponding values of Q . For $T < T_c$, there is again only one lowest minimum at a high value of Q .

In Fig. 4.3(b), the free energy for a system exhibiting a second order transition is shown. When preparing this system at a $T > T_c$ and lowering it, this minimum continuously shifts to higher values of Q as soon as $T \lesssim T_c$. For very low T , the function can become non-convex; however, there is again only one minimum.

A classical example for the application of Landau theory is the description of ordering of liquid crystals. There one can find, among other transitions, a first order isotropic-nematic transition and a second order transition from the uniaxial nematic to the biaxial nematic phase. This phase behavior can be modified by introducing external magnetic fields. Depending on the magnitude of such a field, this can lead to either increasing the nematic ordering or to a suppression of the first-order transition.

The system which we will be concerned with further below is a system of cubic particles on a cubic lattice. Each particle has an internal orientation vector in either the x , y or z direction, and interaction between particles depends on their orientations and relative positions. In this system, the order parameter is defined as either the relative concentration of particles of one orientation, x_α , or a dimensionless order parameter

$$\zeta = x_\alpha - \frac{1}{2}(x_\beta + x_\gamma) \quad (4.9)$$

Assuming $x_\beta = x_\gamma = \frac{1-x_\alpha}{2}$, it is easy to convert from one order parameter to the other.

There are several ways to obtain a free energy function for such a system. The most straightforward approach is a mean-field calculation, inspired by Flory-Huggins theory[99]. There one assumes that each particle interacts with an averaged field of all particles. This significantly simplifies calculations, but ignores local fluctuations, which leads to an underestimation of the value of T_c . Qualitatively, however, such an approach yields good results. The resulting free energy function can then be written as a Taylor series and analyzed according to Landau theory.

In Sec. 6.4 we explicitly calculate the mean-field free energy for such a system and predict phase the phase behavior using arguments from Landau theory.

Chapter 5.

Isotropic interactions

The results of this chapter have been previously published in Phys. Rev. E **103**, 023302 [100]

Previously, most work regarding simulations of thin film growth has been concerned with systems in which substrate and deposit consist of the same material[6]. However, in real-world film growth experiments the substrate and film usually consist of different materials, which leads to different growth modes. These growth modes occur on medium time-scales, i.e. for thin films with a thickness on the order of a few monolayers.

As discussed earlier, in the equilibrium limit, one classically distinguishes between Frank-van-der-Merwe, Vollmer-Weber, and Stranski-Krastanov growth. The exact growth mode there is determined by the particle-substrate interactions and the lattice mismatch between film and substrate. Real-world thin films, however, do not grow under equilibrium conditions, leading to more complicated conditions for the occurrence of certain morphologies.

In this chapter, we investigate how kinetic conditions and the ratio of inter-particle and particle-substrate attractions influence the morphology of a growing film. We then quantify where the transitions between different growth modes occur.

5.1. Models

We will investigate the system using two different models of thin film growth (see snapshots in Fig. 5.1). These are both lattice models, meaning the particles can only reside on discrete positions within a three-dimensional box. The upper and lower boundary of this box are hard, while periodic boundary conditions (PBC) were implemented in the x and y direction.

Interactions between neighboring particles have a strength ϵ (in units of $k_B T$), while particles at $z = 0$ interact with the substrate with a strength ϵ_{sub} .

The first model we implement is a conventional solid-on-solid (SOS) model. Here each particle has to be supported by either the substrate or another particle, meaning that there can be no cavities inside the film. Particles cannot desorb from the film, preventing the formation of a vapor phase. For many experiments (most notably metal-on-metal growth) these restrictions are realistic, since there one typically obtains a compact film without particles desorbing.

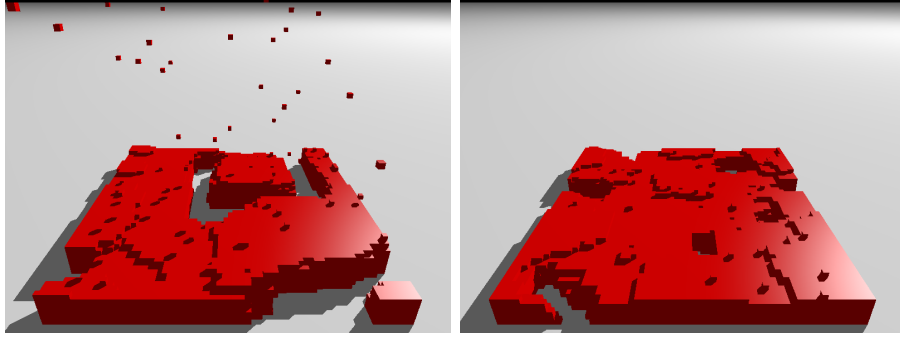


Figure 5.1.: Snapshots after deposition of 5 ML for $\epsilon = -3$, $\epsilon_{\text{sub}} = -1.33$, $\Gamma = 10^4$ in the CGM (left) and the SOS model (right). Due to the fact that particles can desorb from the film in the CGM, we see the formation of a vapor phase above the film.

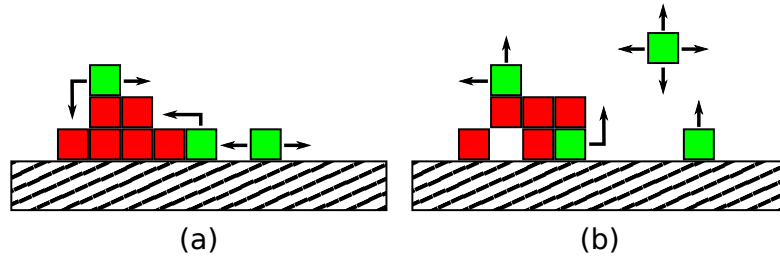


Figure 5.2.: (a) Schematic representation of the allowed moves in the SOS model and (b) additional moves allowed in the CGM

During each time step of the KMC simulation, we randomly choose to either insert a new particle into the system or to move an existing particle. If we insert a new particle, we choose a random lattice site and insert the particle on top of the highest particle in this column. If we choose to move a particle, we pick a random particle at the surface and try to move it to a neighboring site according to the Metropolis condition (with the restriction that the height difference between both sites can be no larger than 1 lattice site). Schematic representations of these moves are shown in Fig. 5.2(a).

The second model we dub Colloidal Growth Model (CGM). In this model, restrictions are relaxed insofar that particles are now allowed to desorb from the film. This leads to the formation of a vapor phase above the film, as well as the existence of overhangs and cavities inside the film (see Fig. 5.2(b) for schematic representations of the additional moves).

This model is reminiscent of the growth of colloidal films in solution[101], hence the name. It is the most generic extension of the simple SOS model. However, a large amount of additional bookkeeping is required here, since certain assumptions (e.g. that only the highest particle in any column can move) are no longer valid, leading to a sharp increase in simulation time. Additionally, we now also have to consider how exactly new particles are inserted into the system.

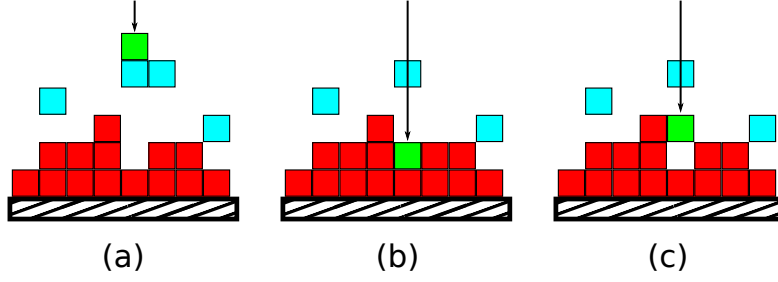


Figure 5.3.: Possible ways to insert new particles in the CGM. Red particles are connected to the substrate, blue particles are in the gas phase, and the newly inserted particle is indicated in green. (a) The new particle diffuses down until it touches any other particle (including those in the vapor phase). (b) The particle diffuses down towards the topmost particle in the chosen column. (c) The particle diffuses down until it touches any particle *connected to the film*.

In principle, there are three possible ways (shown schematically in Fig. 5.3):

1. A particle is inserted at the top of the box and diffuses downwards until it touches any other particle. Since we do not implement cluster moves, this however leads to the formation of large, stable clusters inside the gas phase, eventually blocking new particles from reaching the substrate.
2. The new particle is inserted on top of the topmost particle in the chosen column. This is most similar to insertion in the SOS model.
3. A particle is inserted at the top of the box and diffuses downwards until it touches any particle *connected to the film*. This is similar to insertion in colloidal growth experiments.

5.2. Observables

An important observable in both thin film growth experiments and simulations is the film roughness σ . It is defined as

$$\sigma = \sqrt{\frac{1}{N} \sum_{i=1}^N (h_i - \bar{h})^2} \quad (5.1)$$

where N is the number of lattice sites, h_i the film height at lattice position i and \bar{h} the mean height of the film. As the name indicates, σ is a measure of how rough the film is, and its magnitude allows us to draw conclusions about the morphology of the film. For example, when $\sigma(t)$ oscillates between 0 and 0.5, the film typically grows in a layer-by-layer fashion.

The advantage of σ as an observable is the relative ease with which it can be measured in experiments, both in-situ (using e.g. X-ray reflectivity measurements[102]) and ex-situ (using e.g. atomic force microscopy measurements[103]). However, it does not contain any information about structure, creating the need to complement σ by other observables, or often omitting its measurement in favor of e.g. reciprocal space maps obtained by X-ray scattering or grazing incidence diffraction[104].

The second observable we will use in this chapter is the layer-filling difference

$$\Psi_{i-j} = \Psi_i - \Psi_j \quad (5.2)$$

where Ψ_i is the ratio of occupied lattice sites in layer i . Specifically, we are interested in

$$\Psi_{1-2} = \Psi_1 - \Psi_2$$

which denotes the difference in layer filling between the layer in contact with the substrate and the one on top of it. If we measure Ψ_{1-2} after deposition of one monolayer, it allows us to decide whether a film initially grows in a layer-by-layer fashion ($\Psi_{1-2} = 1$), an island fashion ($\Psi_{1-2} = 0$), or something in-between.

5.3. Parameter scaling

Ultimately, we perform our simulations in order to compare the results to those of thin-film growth experiments, mostly of organic molecules. For this to yield plausible results, the kinetic and energetic parameters need to be in approximately the same regions.

To put this in context, for thin film growth of C_{60} on C_{60} at room temperature[105, 106], the diffusion coefficient is typically $D = \mathcal{O}(10^8)$ nm²/s, while deposition flux is usually on the order of $F = 0.001 \dots 0.1$ monolayers per second. We then find for the ratio of deposition rate and flux $\Gamma = D/(Fl^2) = \mathcal{O}(10^9) \dots \mathcal{O}(10^{11})$, where l is the length of a unit cell. Additionally, using the Girifalco potential[107], we can estimate the inter-particle interaction to be $\epsilon_0 \approx -10k_B T$. Such slow growth and strong interactions are difficult to model computationally, even in the SOS model. Usually simulation studies at such parameters will be limited to only simulating a few monolayers[85]. We argue, however, that we can simulate film growth at lower Γ and weaker values of ϵ and reasonably extrapolate to higher Γ and stronger values of ϵ .

As indicated earlier, for the island density in sub-monolayer growth a scaling relation of the form

$$N(\Gamma, \Theta) \propto \Theta^{1/3} \Gamma^{-1/3} \quad (5.3)$$

has been identified[41]. In this scenario, where dimers are stable ($i^* = 1$), the sub-monolayer island density does not depend on the inter-particle interactions.

The assumption that dimers are stable for the typical duration of the growth experiment does, however, necessitate very strong values of ϵ , comparable to e.g. covalent bonds between metallic molecules. Interactions between organic molecules are typically

significantly weaker, leading to dimers not necessarily being stable against decomposition and thus changing the scaling behavior of island densities.

To investigate this, we obtained the publicly available sub-monolayer data from Ref. 108, which contains pairs of energies E_D and E_B with the corresponding occupation of lattice sites at a coverage $\Theta = 0.15$. Here, E_D was the diffusion barrier energy and E_B was the strength of the inter-particle attraction. We used these data to calculate island densities at the different parameter sets and then translated the energetic parameters to our ϵ and Γ in order to determine whether we could find scaling behavior.

The authors used a Clarke-Vvedensky ansatz to determine the diffusion rate,

$$d_{ij} = \frac{2k_B T}{h} \exp\left(-\frac{E_D + n_i E_B}{k_B T}\right) \quad (5.4)$$

where n_i is the number of nearest neighbors of a particle.

The parameters used were $T = 273$ K, $E_s = 0$ and deposition rate $f = 0.0167$ monolayers/s. Thus we can translate these parameters to our system parameters as:

$$|\epsilon| = \frac{E_B}{k_B T} \quad (5.5)$$

$$\Gamma = \frac{\frac{2k_B T}{h} \exp\left(-\frac{E_D}{k_B T}\right)}{0.0167 \frac{1}{s}} \quad (5.6)$$

which gives for $E_D \in [0.4 \text{ eV} \dots 0.55 \text{ eV}]$ a range of $\Gamma \in [4.78 \cdot 10^4 \dots 2.8 \cdot 10^7]$ and for $E_B \in [0.1 \text{ eV} \dots 0.4 \text{ eV}]$ a range of $|\epsilon| \in [4.25 - 17]$. Note the subtle difference in kinetics: We accept moves with a probability depending on the *energetic difference* between initial and final state, while in the CV model only the number of neighbors in the initial state is considered. The general argument still holds, however.

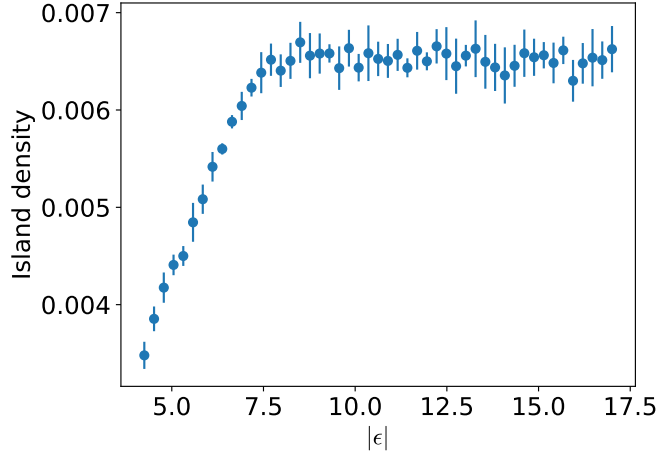


Figure 5.4.: Island density at $\Theta = 0.15$ vs. ϵ at $E_D = 0.55$ eV, i.e. $\Gamma \approx 4.78 \cdot 10^4$. When ϵ is weak, the island density clearly scales with ϵ , while for strong ϵ it remains constant, showing the crossover into the domain where dimers are stable.

In Fig. 5.4 we plot the calculated island density vs $|\epsilon|$ for a constant value of $\Gamma \approx 4.78 \cdot 10^4$. For low values of ϵ , the island density clearly changes as the strength of ϵ increases, eventually going towards a constant value for $|\epsilon| \gtrsim 8$. This change occurs due to the cross-over into the regime in which dimers of particles do not dissociate during the simulation time, i.e. the regime where dimers are stable and thus the island density only depends on Γ and Θ . We found such behaviors for all values of Γ .

To show that for weak ϵ we recover a scaling of the island density with ϵ , we plot the measured island densities scaled versus a function of the form $\Gamma^x(\epsilon + a)$, which was used in Ref. [19] to determine the scaling of surface roughness. We find empirically that for $|\epsilon| \lesssim 9$, a good data collapse can be achieved for $a = \exp(-8)$ and $x = 1.5$ (see Fig. 5.5).

This means that in the regime of weak ϵ , which we have investigated in our work, the island density scales with both Γ and ϵ . More specifically, this allows us to run our simulations at low values of Γ and ϵ and extrapolate to higher values, provided we do not cross over into the regime where dimers become stable. In our simulations, we investigate $|\epsilon|$ between 2 and 6 at $\Gamma = 10^4$ and 10^5 , which is well within the scaling region.

However, it should be reiterated that this scaling relation has so far only been identified for sub-monolayer films at low densities. It is unclear whether such a relation still holds in the multilayer regime, especially since here additional energetic parameters (ϵ_{sub} and E_{ES}) have to be considered and possibly enter the scaling relation.

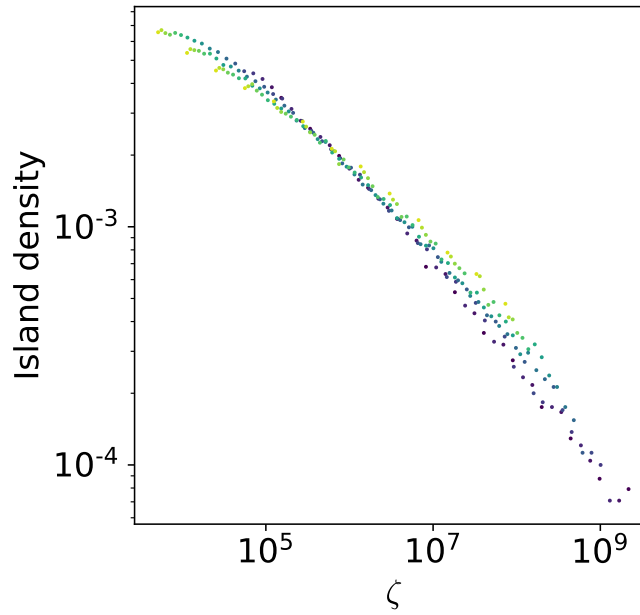


Figure 5.5.: Island density vs $\zeta = \Gamma^{1.5}(\epsilon + \exp(-8))$ for $|\epsilon| \lesssim 9$. Colors denote the strength of ϵ , going from purple (weak) to yellow (strong)

5.4. Results

Unless denoted otherwise, results for the CGM will be for a box of size $64 \times 64 \times 200$. In the SOS model, we were able to simulate larger lateral lattice sizes (up to $L = 300$), however, most results will be for $L = 64$ in order to be able to compare the two models. While these are rather small lattice sizes, we will show that the systems are sufficiently large for our study of film morphologies.

5.4.1. Dynamic layering transition

In Fig. 5.6 we show the evolution of σ vs. the total coverage Θ for both models at different values of ϵ and ϵ_{sub} . In both models, for both $\epsilon = -3$ and -5 , upon increasing the magnitude of ϵ_{sub} the value of $\sigma(\Theta)$ will initially decrease and then go towards oscillating behavior, indicating a transition from island formation to layer-by-layer growth. This transition, which we dub ISL \leftrightarrow LBL, is a dynamic layering transition. As discussed in Sec. 4.2, in an equilibrium system we would expect the transition ISL \leftrightarrow LBL to occur at $\epsilon_{\text{sub, crit}} = \epsilon$ when $\epsilon \rightarrow -\infty$, i.e. if ϵ_{sub} is weaker than ϵ we expect the film to form islands and vice versa. For finite values of ϵ , this transition is slightly shifted, however still at $\epsilon_{\text{sub, crit}} \approx \epsilon$. In Fig. 5.6 it becomes clear, however, that in the non-equilibrium film growth situation, this transition can occur at significantly weaker ϵ_{sub} . This is due to the fact that, at the right parameters, particles on the substrate will be “buried” and hence immobilized before they are able to properly equilibrate and form islands. After

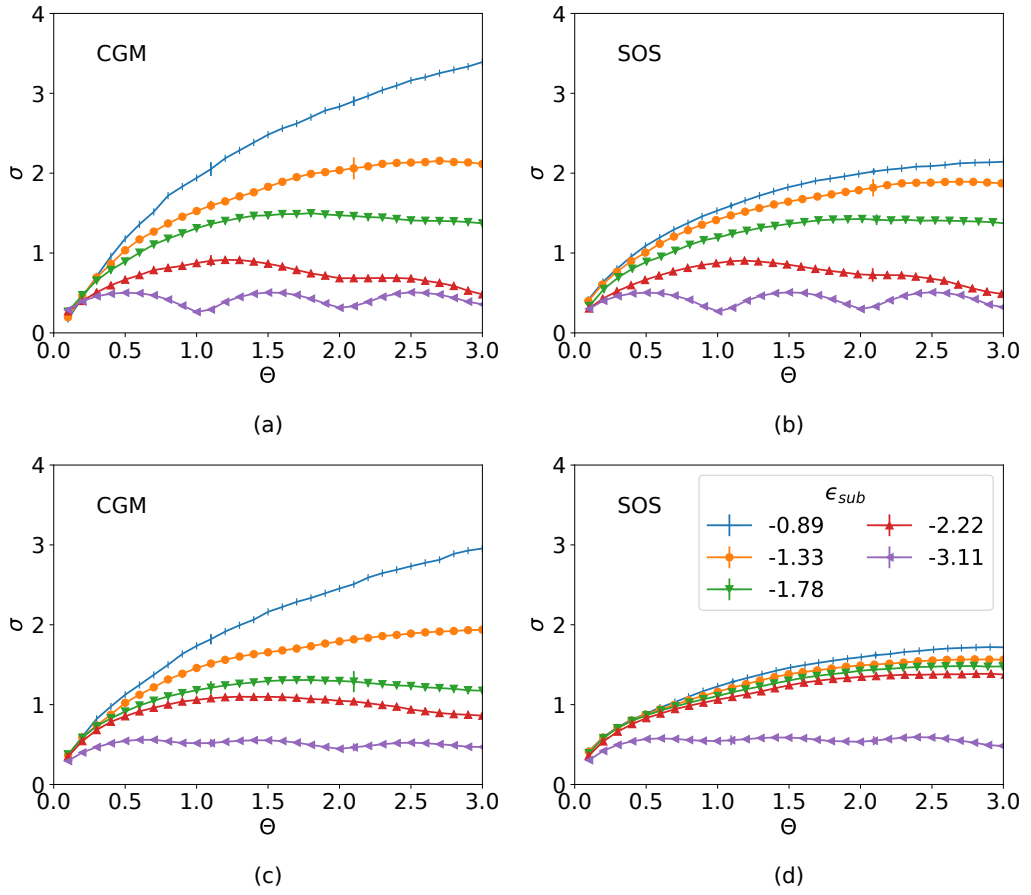


Figure 5.6.: Plot of σ vs Θ , averaged over 5 runs, in the CGM and SOS model at $\Gamma = 10^4$ and multiple substrate strengths ϵ_{sub} . (a), (b) $\epsilon = -3$ and (c), (d) $\epsilon = -5$

the first layer of particles has been buried in this way, the next layers will essentially grow on a substrate where $\epsilon_{sub} = \epsilon$ and thus continue to grow in the LBL fashion.

The exact value of this non-equilibrium $\epsilon_{sub, crit}$ cannot be determined analytically. However, we find that after deposition of 1 ML it is already clear whether the film will grow in an LBL fashion or form islands. Thus we focus on this regime in order to find an observable to pinpoint the transition.

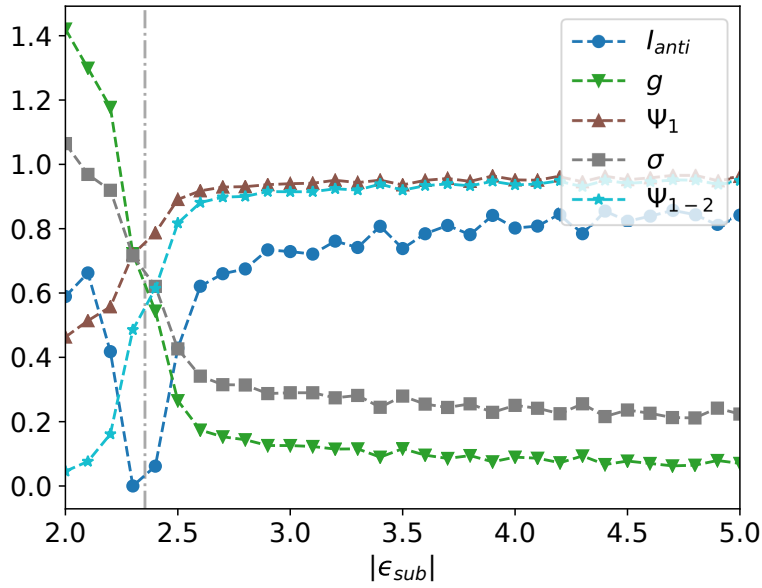


Figure 5.7.: Values of several observables after deposition of one monolayer for $\epsilon = -3$, $\Gamma = 10^4$. All observables (anti-phase Bragg intensity I_{anti} , growth number g , filling of the first monolayer Ψ_1 , roughness σ , and difference of the filling of the lowest two layers Ψ_{1-2}) show a change of behavior at approximately the same value of ϵ_{sub}

In Fig. 5.7 we show the value of several observables after deposition of one monolayer at $\epsilon = -3$, $\Gamma = 10^4$ plotted vs. ϵ_{sub} . The shown observables are:

- Anti-phase Bragg intensity I_{anti}
- Growth number g
- Filling of the first layer Ψ_1
- Roughness σ
- Difference of the filling of the lowest two layers Ψ_{1-2}

The growth number g is defined[10] as:

$$g = \frac{\sum_{n=1}^{\infty} |\Theta_n - \Theta_{n,LBL}|}{\sum_{n=1}^{\infty} |\Theta_{n,stat} - \Theta_{n,LBL}|} \quad (5.7)$$

where Θ_n is the filling of layer n , $\Theta_{n,LBL}$ is the filling of layer n in the case of perfect LBL growth, and $\Theta_{n,stat}$ is the filling of this layer in the case of completely random (Poisson) growth. It indicates whether a film grows in an LBL fashion ($g = 0$), a Poisson manner ($g = 1$), or in-between.

The anti-phase Bragg intensity is defined[10] as:

$$I_{\text{anti}}(\Theta) = \left| \sum_{i=0}^{\infty} (-1)^i (\Psi_i(\Theta) - \Psi_{i+1}(\Theta)) \right|^2 \quad (5.8)$$

where $i = 0$ denotes the substrate, hence $\Psi_0 \equiv 1$. It is used extensively in the analysis of experiments, e.g. if $I_{\text{anti}}(\Theta)$ shows oscillations, this is an indication for LBL growth[38].

All observables show a change in behavior at approximately the same value of ϵ_{sub} , indicating that they are all more or less suitable to pinpoint the location of the dynamic layering transition. As already indicated, we decided to use Ψ_{1-2} as our second observable. This is due to the fact that the value of Ψ_{1-2} is known for LBL ($\Psi_{1-2} = 1$) and ISL ($\Psi_{1-2} = 0$) growth, and that it empirically shows the “best” behavior. For each value of ϵ , we perform simulations at ϵ_{sub} from -2 to -6 , deposit one monolayer in each simulation, and calculate Ψ_{1-2} afterwards. We average the resulting value of Ψ_{1-2} over 5 runs for each parameter set. We can then easily fit a hyperbolic tangent to the data points of Ψ_{1-2} vs ϵ_{sub} and extract the inflection point of this curve as an estimation of $\epsilon_{\text{sub, crit}}$ for the dynamic layering transition.

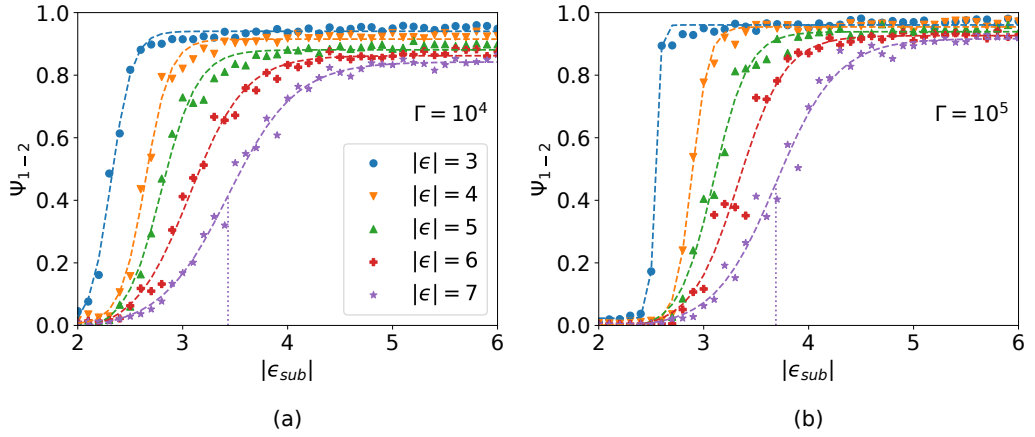


Figure 5.8.: Ψ_{1-2} at $\Theta = 1$ in the CGM for (a) $\Gamma = 10^4$ and (b) $\Gamma = 10^5$, averaged over 5 runs. $\epsilon_{\text{sub, crit}}$ is determined by the value of ϵ_{sub} of the inflection point of the fitted tanh (dotted lines for $|\epsilon| = 7$)

In Fig. 5.8 we show exemplary results for $\Gamma = 10^4$ and 10^5 at different values of ϵ . It is clear that, as the magnitude of ϵ increases, a stronger substrate is necessary for the film to grow in a LBL fashion, while simultaneously the transition becomes more smeared out. This is due to the fact that at stronger ϵ , the system will be further away from equilibrium. Conversely, for $|\epsilon| = 3$ and $\Gamma = 10^5$ (in Fig. 5.8(b)), the transition is almost a discontinuous jump, similar to what we would expect in an equilibrium system. This dependence of the transition width on the kinetic parameters is, however, not a finite size effect, which would occur in equilibrium simulations.

In Fig. 5.9 we show Ψ_{1-2} vs. $|\epsilon_{\text{sub}}|$ for $\epsilon = -7$ and $\Gamma = 10^4$. Neither in the CGM nor the SOS model does the width of the transition change with system size. Merely for

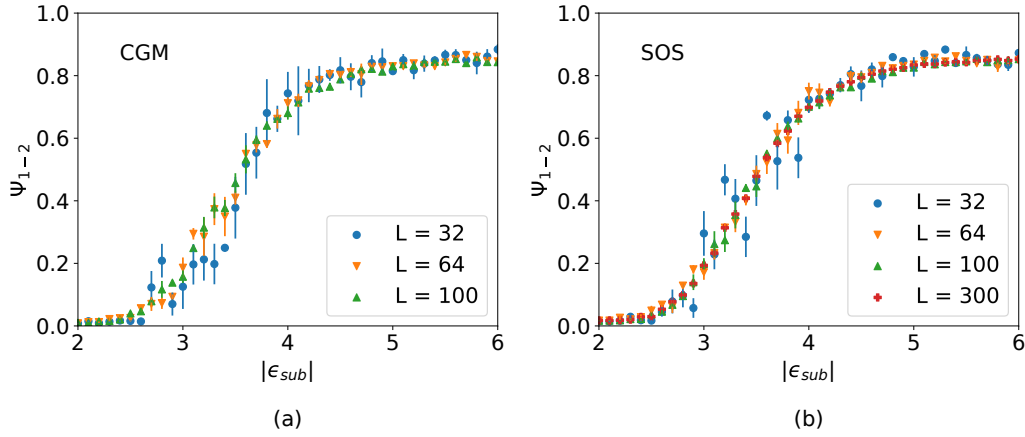


Figure 5.9.: Ψ_{1-2} vs. $|\epsilon_{\text{sub}}|$ at $\Gamma = 10^4$ and $\epsilon = -7$ for different system sizes in (a) the CGM and (b) the SOS model. In neither model the transition width depends on the lateral system size.

small $L \lesssim 32$ the data become very noisy. Due to these results, we are confident that the results presented in this chapter are representative despite the comparatively small value of $L = 64$.

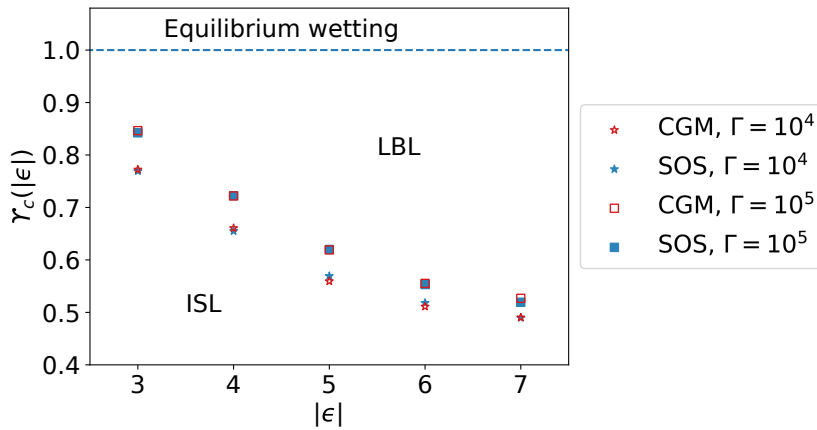


Figure 5.10.: Critical ratio $\Upsilon_c(|\epsilon|) = \frac{\epsilon_{\text{sub, crit}}}{\epsilon}$ for the dynamic layering transition at $\Gamma = 10^4$ and $\Gamma = 10^5$ in the CGM and the SOS model. The blue line indicates the equilibrium value for the layering transition, where $\epsilon_{\text{sub, crit}} \approx \epsilon$

In Fig. 5.10 we show the extracted values for $\epsilon_{\text{sub, crit}}$, re-scaled to $\Upsilon_c \equiv \frac{\epsilon_{\text{sub, crit}}}{\epsilon}$. In these results, it is striking that (1) the extracted $\epsilon_{\text{sub, crit}}$ for the CGM and the SOS model are virtually identical, indicating that the dynamic layering behavior in both systems is similar, and (2) as $|\epsilon|$ increases, the value of Υ_c continuously decreases, which indicates an increasing “dynamic gap” in the layering behavior due to the increased distance to equilibrium.

It may seem surprising that the CGM and the SOS model show similar layering behavior, given the fact that in the CGM particles can desorb from the film, which is a non-negligible process, especially at weaker ϵ and ϵ_{sub} . However, as already seen in Fig. 5.6, the roughness evolution in both models at short times is very similar, indicating that at these timescales desorption might not play a significant role.

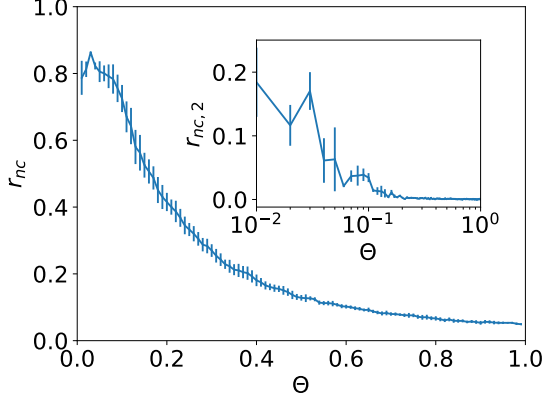


Figure 5.11.: The fraction r_{nc} of floating particles vs. Θ in the CGM at $\Gamma = 10^5$, $\epsilon = -3$, $\epsilon_{\text{sub}} = -2$. Inset: r_{nc} if only particles in the lowest two layers are considered.

This can be confirmed by measuring the amount of particles not connected to the film divided by the total number of particles, r_{nc} , vs. Θ , as shown in Fig. 5.11. The parameters for this figure were chosen to maximize the ratio of floating particles, i.e. the interaction strengths were minimized and Γ was maximized. At very low Θ , r_{nc} is indeed substantial, but quickly approaches 0 as $\Theta \rightarrow 1$. If we only consider disconnected particles in the lowest two layers (shown in the inset in Fig. 5.11), which we also do when measuring Ψ_{1-2} , the ratio $r_{\text{nc},2}$ drops even faster and is zero at $\Theta = 1$. Thus we can expect the number of film particles in the first two layers to be identical in both models, leading to similar morphologies.

In this section, we have shown that the transition from island to LBL growth, which in equilibrium occurs when $\epsilon \approx \epsilon_{\text{sub}}$, is shifted to lower values of ϵ_{sub} in non-equilibrium deposition simulations, thus we call this the dynamic layering transition. Using the parameter $\Upsilon \equiv \epsilon_{\text{sub}}/\epsilon$, we show how this parameter depends on ϵ and Γ . We suspect that the Ehrlich-Schwöbel barrier E_{ES} also plays a role, since it modifies how quickly the system can equilibrate (e.g. how quickly particles can desorb from a weakly attractive substrate to form islands). Hence in general $\Upsilon_c = \Upsilon_c(\epsilon, E_{\text{ES}}, \Gamma)$.

Verifying this experimentally would be challenging: Neither of the energetic parameters can be easily tuned. E_{ES} is an inherent property of the material. ϵ_{sub} can be modified by changing the substrate, but this only allows for a limited amount of values for ϵ_{sub} . Γ can be tuned more easily by changing the deposition rate F . The most commonly used control parameter in experimental setups is the substrate temperature T . Changing T will, however, change all three variables: $\epsilon, E_{\text{ES}} \propto 1/T$ and $D/F \propto \exp(-1/T)$. The dynamic layering transition is a hypersurface in the parameter space $(\epsilon_{\text{sub}}/\epsilon, \epsilon, E_{\text{ES}}, \Gamma)$, meaning that by varying T it is possible to hit one point of the transition, but it is not possible to independently change parameters to find other points of the transition.

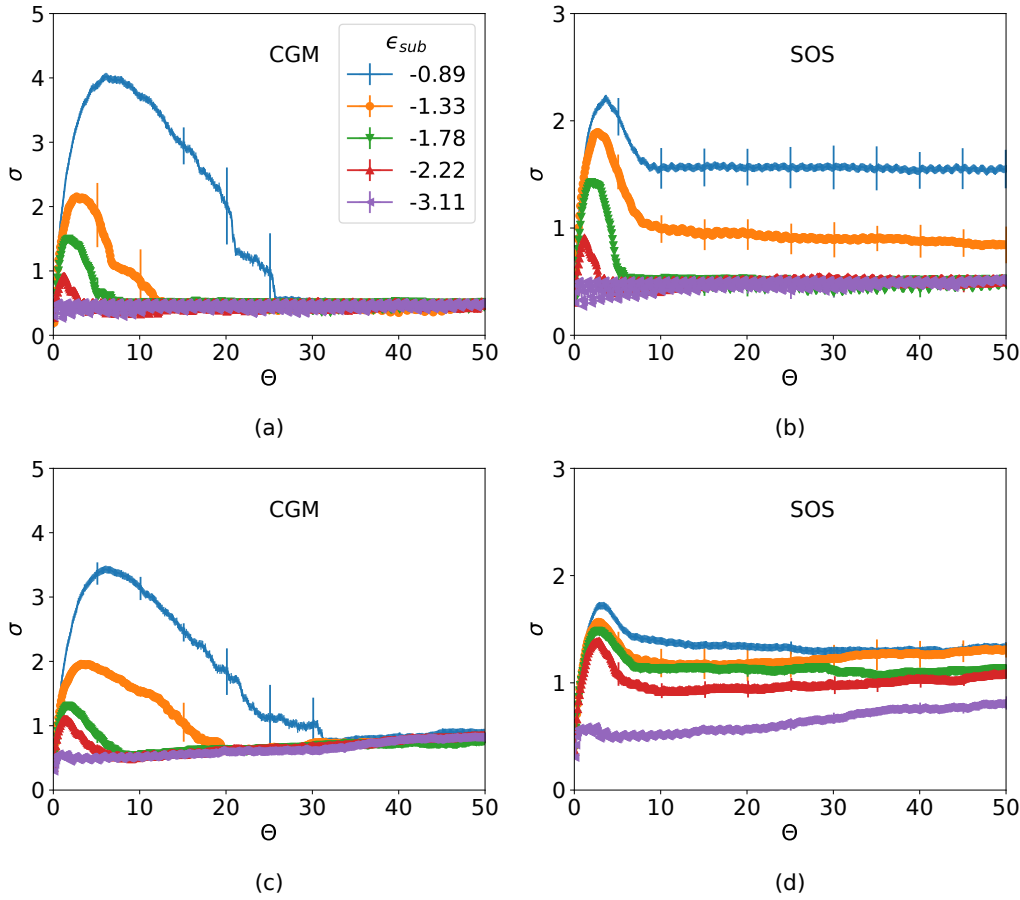


Figure 5.12.: σ vs. Θ up to $\Theta = 50$, in the CGM and SOS model at $\Gamma = 10^4$ and multiple substrate strengths ϵ_{sub} . (a), (b) $\epsilon = -3$ and (c), (d) $\epsilon = -5$. Note that the y-axes for the two models are different. The data for the CGM are averaged over three runs, those of the SOS model over 5 runs.

5.4.2. Flattening transition

While in the previous section we were concerned with the behavior of thin film morphology after deposition of one or few monolayers of material, we will now shift our attention to the processes which occur at intermediate times when $\Theta = \mathcal{O}(10)$. In Fig. 5.12 we show the roughness evolution for the same parameter sets as in Fig. 5.6, but now up to $\Theta = 50$.

For weaker ϵ_{sub} , σ will initially increase strongly, indicating island growth. Interestingly, this is not permanent: After further deposition, the film roughness will decrease again and eventually go towards oscillating values of $\sigma \lesssim 1$, indicating LBL growth. This behavior can be observed in both model; however, in the CGM it occurs for all $\epsilon_{\text{sub}} < \epsilon_{\text{sub, crit}}$, while in the SOS model it will only occur at relatively weak ϵ and relatively strong ϵ_{sub} . Otherwise, the film will not go towards the LBL growth mode, but

to a new mode where σ reaches a constant value > 1 . Hence we dub this growth mode **CONST**.

The decrease of σ as time increases can be explained intuitively: As the amount of particles increases, islands will grow in size and hence more substrate sites will be covered. Due to the choice to let the substrate only interact with the first layer of particles, newly arriving particles will “see” an effective substrate which is a mixture of the original substrate and other particles with an increased $\epsilon_{\text{sub, eff}} = \epsilon$. Eventually the substrate will be completely covered and hence growth continues as in a homoepitaxial system (as long as 3D effects are weak at short times, i.e. for sufficiently high Γ and weak E_{ES}).

We call the transitions from island growth to LBL or **CONST** growth **ISL** \rightarrow **LBL** and **ISL** \rightarrow **CONST**, respectively. As already indicated, the **CONST** mode only occurs in the SOS model. This is a consequence of restricting inter-layer moves to only occur one layer up or down. At very weak ϵ_{sub} , the initially formed islands will be comparatively high when coalescence occurs, leaving deep grooves which can only be filled by deposition, not by inter-layer moves. Since deposition is equally probable for all sites, the relative heights of islands and grooves do not change and σ remains constant. In the CGM, where particles can desorb into the gas phase, this growth mode will thus not occur, since any height difference can eventually be smoothed out, leading to LBL growth. Additionally, the desorption of particles will in the early stages of film growth lead to larger, higher islands and consequently higher roughness than in the SOS model at the same parameters.

Pinpointing the times at which these transitions occur is not feasible using the film roughness, since σ only gradually returns to the constant value. When determining transition points, one usually tries to do this using an observable which is discontinuous upon transition. One observable which proved to be viable candidates was the minimum film height.

In Fig. 5.13 we show plots of the minimum film height and σ vs. Θ for different values of ϵ_{sub} in both models. For weak substrates, the minimum height in the CGM initially be 0 but then exhibit a discrete jump and start increasing linearly such that $\min\{h(\Theta)\} \approx \Theta$. This coincides with the value of σ being < 1 , indicating LBL growth. In contrast, in the SOS model the minimum height will be 0 initially and then start increasing linearly near the roughness drop (without jumping).

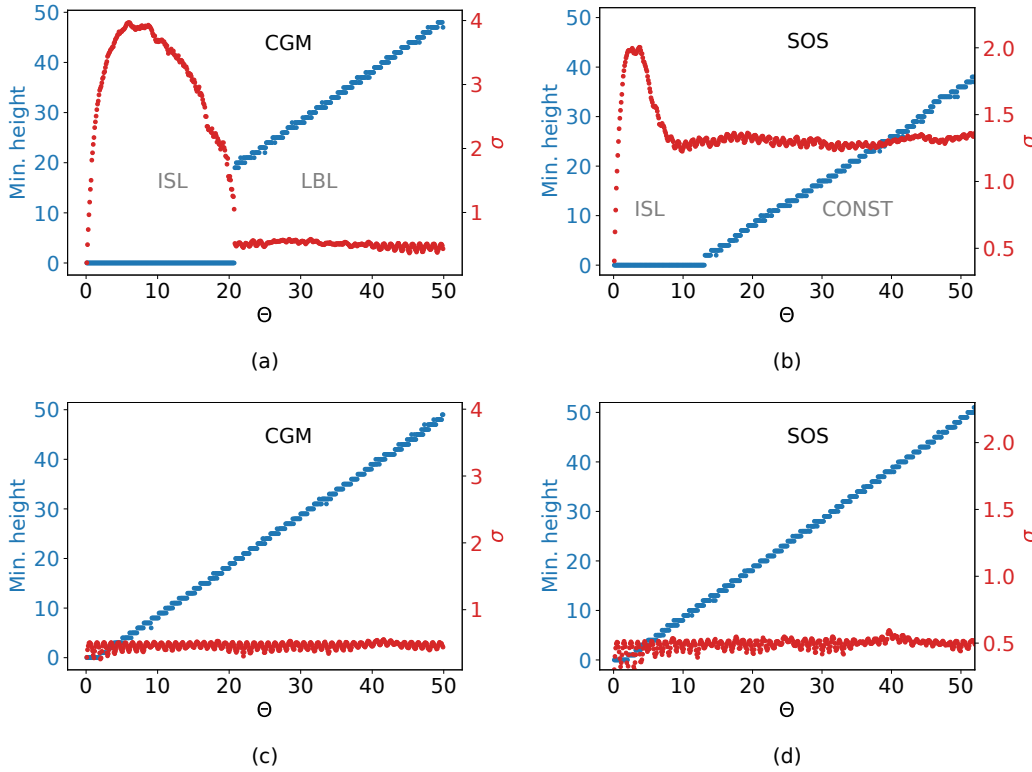


Figure 5.13.: Minimum film height and roughness vs. Θ in the CGM and the SOS model for $\epsilon = -3$, $\Gamma = 10^4$ at (a), (b) $\epsilon_{\text{sub}} = -0.89$ and (c), (d) $\epsilon_{\text{sub}} = -2.67$. At $\epsilon_{\text{sub}} = -0.89$ in the CGM model, the minimum height will exhibit a jump at the transition from ISL to LBL growth, while in the SOS model, the minimum height starts increasing from 0 at the transition from ISL to CONST. At $\epsilon_{\text{sub}} = -2.67$ such an increase is visible in both models from the start

Due to these two different behaviors, we used different methods to extract the numerical value of the transition point Θ_{trans} . In the SOS model, we averaged $\min\{h(\Theta)\}$ over several runs, fit a line to the region of linearly increasing min. height, and extracted the root of this line as the value of Θ_{trans} for the transition ISL \rightarrow CONST. In the CGM, we defined a fit function,

$$f(x) = \begin{cases} 0, & \text{if } \Theta < \Theta_{\text{trans}} \\ a \cdot \Theta + b, & \text{else} \end{cases} \quad (5.9)$$

where Θ_{trans} is the transition point ISL \rightarrow LBL. a , b , and Θ_{trans} are free parameters which we fitted for each run. The resulting Θ_{trans} for all runs were then averaged to obtain the final result. Examples for the fit procedures can be seen in Fig. 5.14.

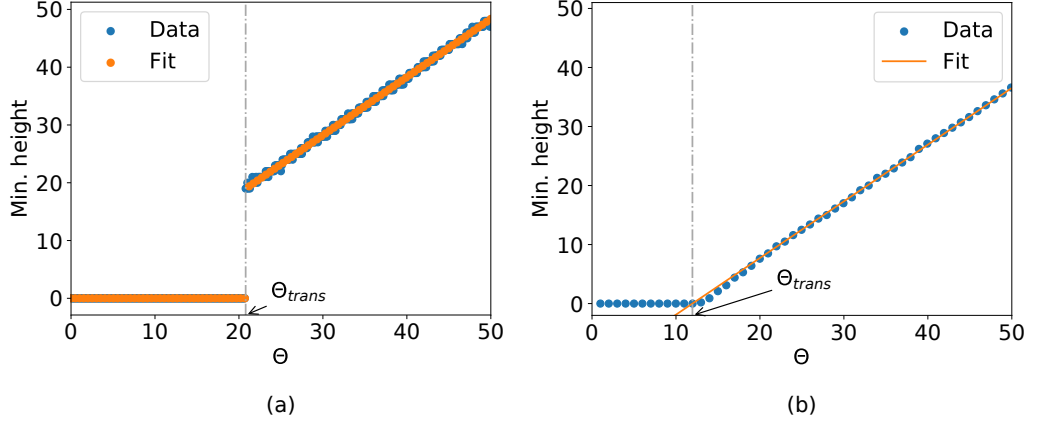


Figure 5.14.: Examples for the fit procedure to determine Θ_{trans} for $\epsilon = -3$, $\epsilon_{\text{sub}} = -0.89$, $\Gamma = 10^4$ in (a) the CGM and (b) the SOS model.

The dependence of Θ_{trans} on ϵ_{sub} reveals an interesting characteristic of the system. In Fig. 5.15 we show Θ_{trans} vs. ϵ_{sub} for $\epsilon = -3$, -5 in both models. In the SOS model for $\epsilon = -3$ (in Fig. 5.15(b)) we can identify three distinct regions: For $|\epsilon_{\text{sub}}| \lesssim 1.33$, Θ_{trans} has a value of ~ 10 , indicating that at these substrate strengths the system will initially grow in the ISL mode and after deposition of ~ 10 monolayers the growth mode changes to CONST. For $1.33 < |\epsilon_{\text{sub}}| < 2.67$ the value of Θ_{trans} is ≈ 2 . This indicates that here the system will initially grow in the ISL mode (since $|\epsilon_{\text{sub}}| < |\epsilon_{\text{sub, crit}}|$, i.e. the system is below the dynamic wetting transition) and at later times transitions towards the LBL mode. For even stronger values of ϵ_{sub} , the system will grow in the LBL mode from the start. These abrupt changes thus mean that the system shows a “**transition** (upon change of ϵ_{sub}) **between transition scenarios** (in roughness evolution)”. For $\epsilon = -5$ (in Fig. 5.15(d)), the jump in Θ_{trans} occurs at $\epsilon_{\text{sub}} \approx \epsilon_{\text{sub, crit}}$, leading to the disappearance of the ISL→LBL transition, which is swallowed by the LBL mode. Consequently, we observe only a transition from ISL→CONST to LBL upon increasing $|\epsilon_{\text{sub}}|$. In the CGM (Fig. 5.15(a) and (c)), there is only the transition from *ISL→LBL* to *LBL* at $\epsilon_{\text{sub}} = \epsilon_{\text{sub, crit}}$, with Θ_{trans} smoothly decreasing as $|\epsilon_{\text{sub}}|$ increases.

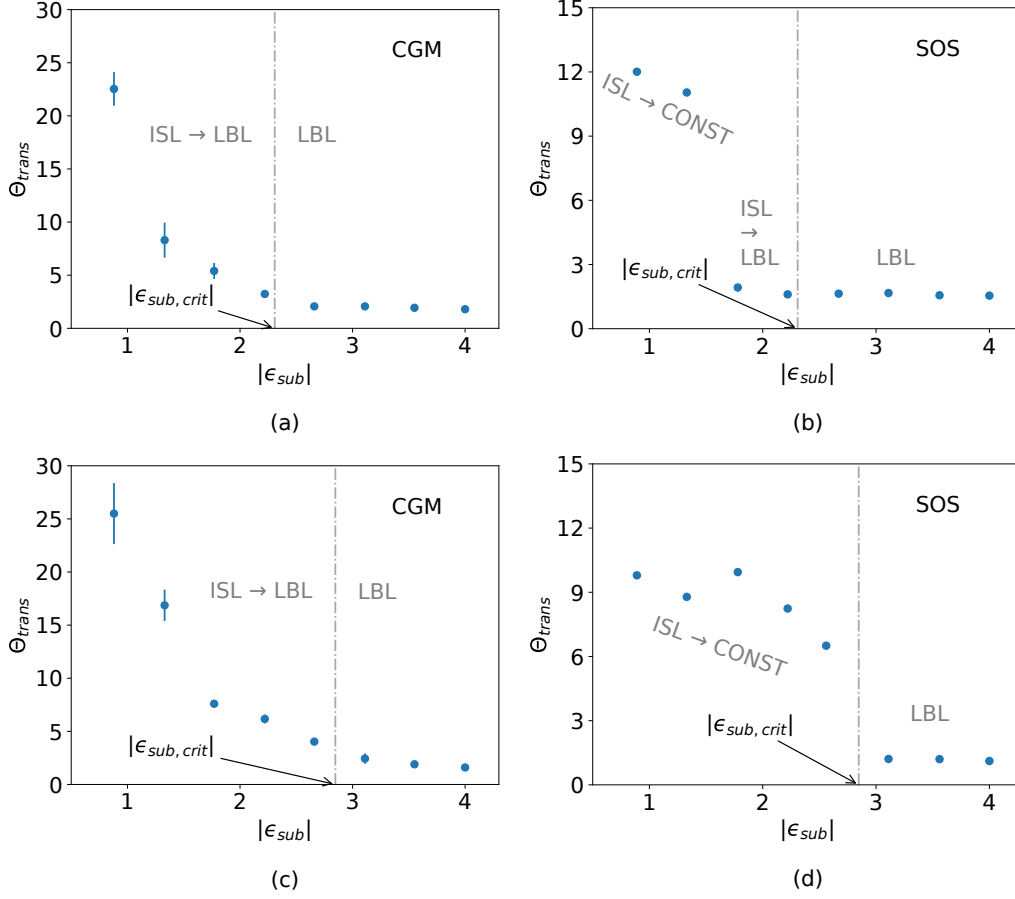


Figure 5.15.: Θ_{trans} vs ϵ_{sub} in the CGM and SOS model at (a), (b) $\epsilon = -3$ and (c), (d) $\epsilon = -5$. For $\epsilon = -3$ in the SOS model, Θ_{trans} shows a jump from ISL \rightarrow CONST to ISL \rightarrow LBL at an ϵ_{sub} which is lower than the dynamic wetting transition. For $\epsilon = -5$, this jump is at $\epsilon \approx \epsilon_{\text{sub}}$, leading to the disappearance of the ISL \rightarrow LBL mode. In the CGM, Θ_{trans} smoothly decreases as $|\epsilon_{\text{sub}}|$ is increased, leading to a continuous transition from ISL \rightarrow LBL to LBL growth

5.4.3. Asymptotic growth behavior

In the preceding sections, we have quantitatively analyzed the dynamic layering transition and the flattening transition, as well as the transition between transition scenarios in systems where $\epsilon_{\text{sub}} \neq \epsilon$. In both the SOS model and the CGM, eventually all sites of the substrate will be covered by particles. This means that the system returns to homoepitaxial growth where substrate and film consist of the same material.

We then expect the film roughness to increase for long deposition, albeit only weakly for $E_{\text{ES}} = 0$. This case has recently been studied for the SOS model[19], and it has been found that the roughness shows a scaling behavior of the form

$$\sigma \propto \Theta^\beta / (\Gamma^{3/2} (\exp(-|\epsilon|) + a)) \quad (5.10)$$

with $\beta \approx 0.2$ and $a = 0.025$. For the case $|\epsilon| < -\ln a \approx 3.7$ this then leads to equivalent roughness evolution if

$$|\epsilon| - \frac{3}{2} \log \Gamma = \text{const.} \quad (5.11)$$

(Compare this to Eq. 2.22 for the scaling of island density at sub-monolayer coverage, where the factor $\frac{3}{2}$ is absent.).

These transitions will only occur at sufficiently high values of Γ . For $\Gamma \rightarrow 0$, the SOS system goes towards the limiting case of stochastic growth ($\sigma \propto \Theta^{1/2}$). In this extreme case, the system will grow in a rough manner from the beginning, and upon increasing Γ we eventually cross over to the scenarios described above.

5.4.4. Non-zero E_{ES}

The previously shown results are all for $E_{ES} = 0$. We want to briefly discuss how changing the value of E_{ES} impacts the occurrence of growth modes and especially transitions between them. For the case of homoepitaxial growth with $\epsilon = \epsilon_{sub}$, an analytical solution has been found[109] for the SOS model with $\epsilon \rightarrow -\infty$ using rate equations. There it was found that increasing E_{ES} gradually increases the Γ necessary for LBL growth to occur, which matches our simulations quite well. In general, we can find the same growth modes as for $E_{ES} = 0$, as well as the transitions between them, albeit shifted to higher values of Γ . This is especially the case for the ISL→LBL transition, since this transition necessitates inter-layer moves of particles, which are slowed down by non-zero E_{ES} .

For finite values of E_{ES} , the phenomenologies in the CGM and the SOS model are qualitatively identical, however, for $E_{ES} \rightarrow \infty$ (effectively prohibiting direct inter-layer moves) interesting discrepancies arise. In the SOS model, this leads to the film growing stochastically. In the CGM, on the other hand, there will always be net inter-layer particle transport due to particles desorbing from the film, diffusing in the gas phase, and re-adsorbing in a different layer, effectively lowering the value of E_{ES} .

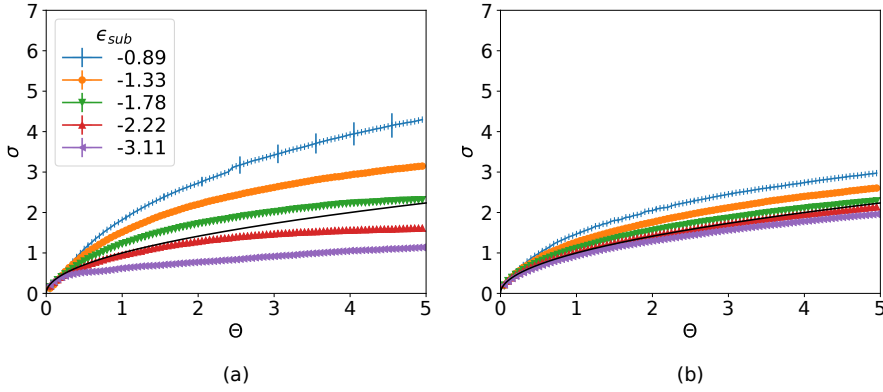


Figure 5.16.: σ vs. Θ in the CGM for $E_{ES} = \infty$ at $\Gamma = 10^4$ for different ϵ_{sub} and (a) $\epsilon = -3$, (b) $\epsilon = -5$. The black line denotes the statistical roughness evolution $\sigma = \sqrt{\Theta}$.

In Fig. 5.16 we show σ vs. Θ in the CGM for $\epsilon = -3$ and -5 and a range of ϵ_{sub} . For weak values of $|\epsilon_{sub}|$, the roughness is significantly higher than $\sqrt{\Theta}$, indicating strong island formation. As $|\epsilon_{sub}|$ increases, the roughness evolutions for the two values of ϵ diverge: For $\epsilon = -3$, σ decreases to values < 1 , indicating that here the system will again go towards smooth films as $|\epsilon_{sub}|$ increases. In contrast, for $\epsilon = -5$ the roughness curves at increasing $|\epsilon_{sub}|$ will saturate around the stochastic evolution $\sigma \propto \Theta^{1/2}$. Other observables, such as layer-filling vs. time, confirm that here indeed ϵ is strong enough for desorption from the film to become negligible and the film to grow in a stochastic manner.

We thus have a new transition for $E_{\text{ES}} \rightarrow \infty$: For weak ϵ , the system will show the familiar growth modes which we can also find for $E_{\text{ES}} = 0$, while for stronger ϵ the system will grow in a stochastic manner.

To determine the location of the transition from LBL to stochastic growth, we performed simulations at $\epsilon_{\text{sub}} = -10^6$, such that particles which reach the substrate will stay in the first layer. This was done in order to ensure that no other transitions, e.g. ISL \rightarrow LBL, could occur upon changing ϵ . We then performed simulations for different values of Γ , where for each Γ we swepted $|\epsilon|$ from 2 to 6. Each simulation was run until $\Theta = 1$ before measuring $\Psi_{1-2}(|\epsilon|)$, similar to Sec. 5.4.1.

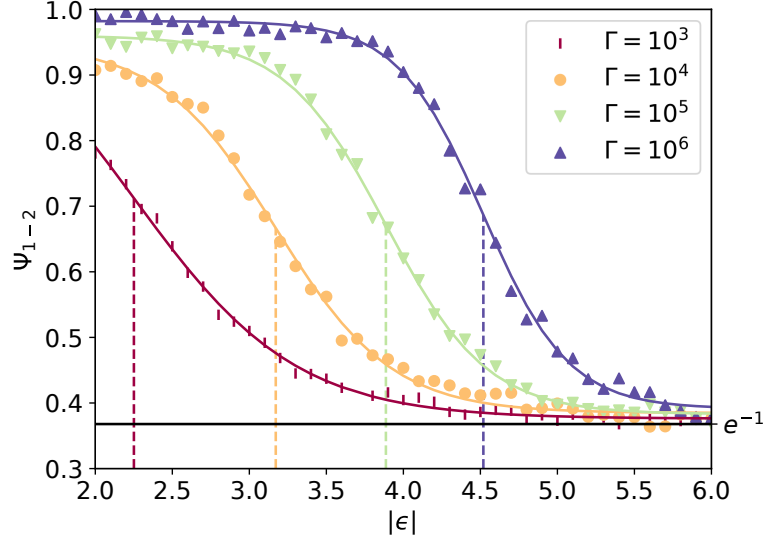


Figure 5.17.: $\Psi_{1-2}(|\epsilon|)$ after deposition of one ML in the CGM at $E_{\text{ES}} = \infty$ and $\epsilon_{\text{sub}} = -10^6$ for different values of Γ . The dashed lines indicate the inflection points of the fitted curves, while the solid line indicates the stochastic limit of $\Psi_{1-2} = \exp(-1)$.

In Fig. 5.17 we show the resulting data points. We can again fit a tanh curve to the data and extract its inflection point as the transition from LBL to stochastic growth. For weak ϵ , Ψ_{1-2} has a value of almost 1, since there particles in the second layer can easily reach the substrate via a multi-step diffusion process, after which they are stuck in the first layer, leading to all particles being in the first layer eventually. For strong ϵ , Ψ_{1-2} will go towards the value e^{-1} (denoted as the black line), which is the value we expect for stochastic growth with no inter-layer diffusion: The filling of the n th layer at coverage Θ is:[10]

$$\Psi_{n,\text{stat}}(\Theta) = 1 - \exp(-\Theta) \sum_{k=0}^{n-1} \frac{\Theta^k}{k!} \quad (5.12)$$

with the 0th layer being the substrate, i.e. $\Psi_0 \equiv 1$. Thus we obtain:

$$\begin{aligned}\Psi_{1-2}^{\text{stat}} &= \Psi_{1,\text{stat}}(1) - \Psi_{2,\text{stat}}(1) \\ &= \exp(-1)\end{aligned}\tag{5.13}$$

Hence we find that even in the CGM, the system can grow in a stochastic manner, given ϵ is strong enough. For increasing Γ , the critical ϵ for this transition increases, and for $\Gamma \rightarrow \infty$ we should also find $|\epsilon| \rightarrow \infty$, since in such an equilibrium scenario particles will always be able to desorb from the film eventually.

5.4.5. Global growth mode diagram

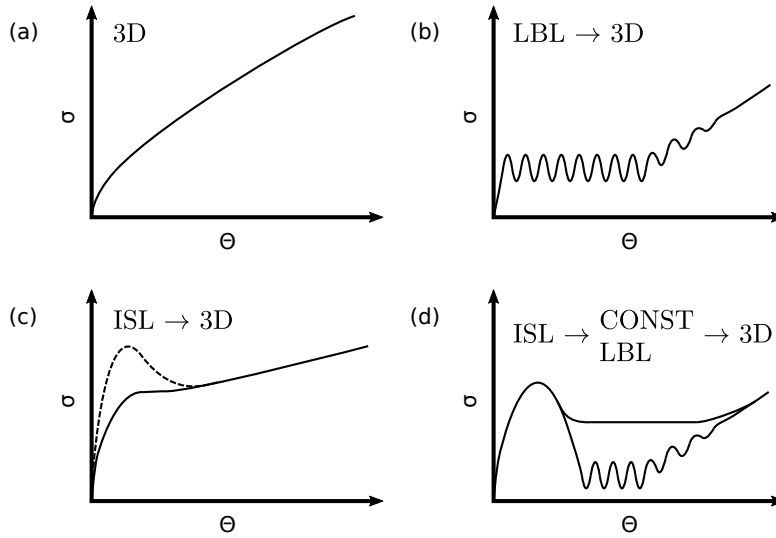


Figure 5.18.: Schematic representations of possible transitions in thin film growth. (a) Three-dimensional growth from the start. This occurs at small values of Γ or large values of E_{ES} . (b) Initial LBL growth, followed by 3D growth for larger Γ and $|\epsilon_{\text{sub}}| > |\epsilon_{\text{sub, crit}}|$. (c) Initial ISL growth, followed by 3D growth for intermediate Γ and $|\epsilon_{\text{sub}}| < |\epsilon_{\text{sub, crit}}|$. (d) Initial ISL growth, followed by LBL or const growth and finally 3D growth for high Γ and $|\epsilon_{\text{sub}}| < |\epsilon_{\text{sub, crit}}|$.

Tying everything together, we can now construct a diagram of all global growth scenarios of these systems, which we show in Fig. 5.18. As already indicated, systems will show asymptotic 3D growth for long times in all scenarios. For small values of Γ (high deposition rates) or high values of E_{ES} , the system will show 3D roughening from the start (Fig. 5.18(a)). For larger values of Γ and weaker values of ϵ_{sub} , we have to distinguish between the cases $|\epsilon_{\text{sub}}| > |\epsilon_{\text{sub, crit}}|$ and $|\epsilon_{\text{sub}}| < |\epsilon_{\text{sub, crit}}|$, where $\epsilon_{\text{sub, crit}} = \epsilon_{\text{sub, crit}}(\epsilon, \Gamma, E_{\text{ES}})$ (since $\epsilon_{\text{sub, crit}}$ is the point of the dynamic layering transition). In the first case, the system will initially grow in a LBL fashion and then show increased roughness for long

times, i.e. the **LBL**→**3D** transition as seen in Fig. 5.18(b). In the second case, the system will initially form islands. For intermediate values of Γ , the film will then transition to strongly roughening 3D growth without the roughness decreasing first (Fig. 5.18(c)), while for large values of Γ the roughness does decrease due to the film going to either the LBL or the CONST growth mode (the flattening transition discussed in Sec. 5.4.2) and then subsequently roughening (Fig. 5.18(d)).

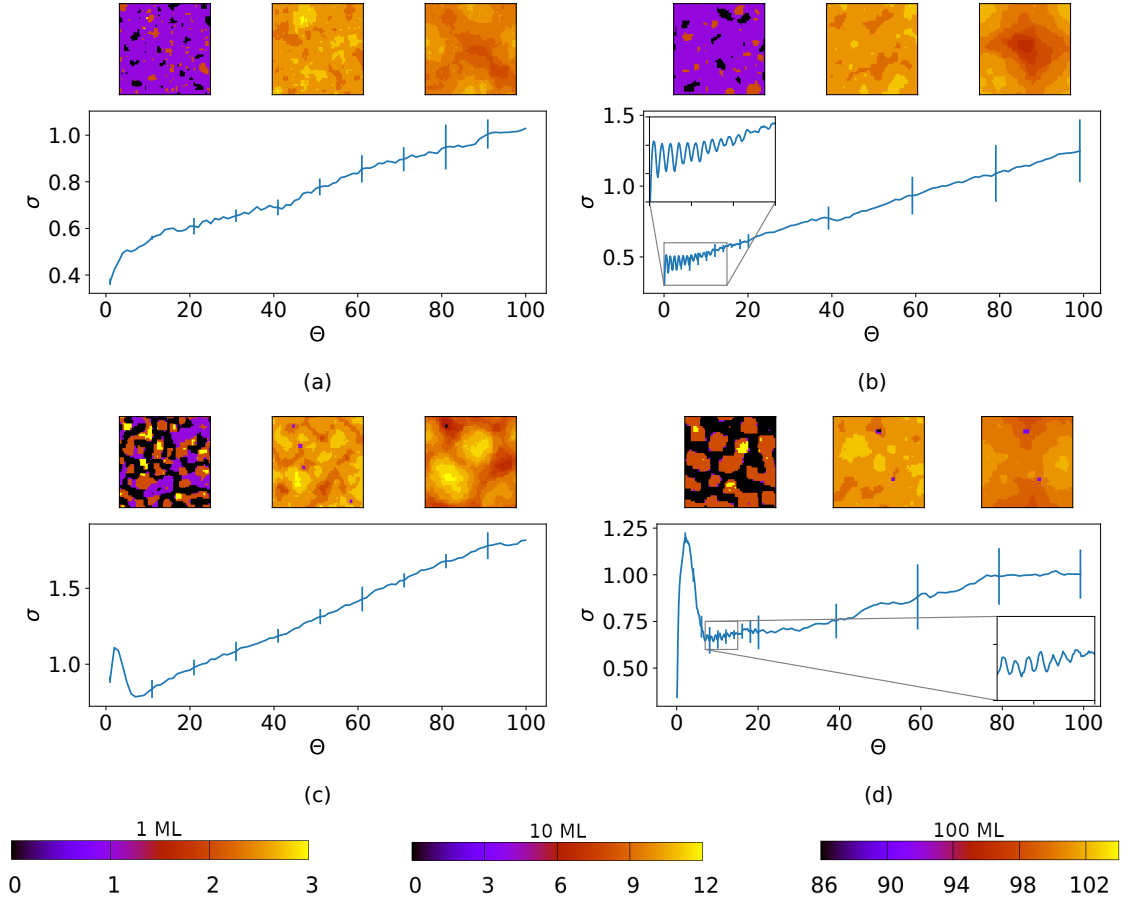


Figure 5.19.: Examples of simulations of the growth modes sketched in Fig. 5.18 in the SOS model. (a) 3D growth at $\Gamma = 10^3$, $\epsilon = -3$, $\epsilon_{\text{sub}} = -3.56$ (b) LBL→3D at $\Gamma = 10^4$, $\epsilon = -5$, $\epsilon_{\text{sub}} = -3.56$ (c) ISL→3D at $\Gamma = 10^3$, $\epsilon = -5$, $\epsilon_{\text{sub}} = -2.22$ (d) ISL→LBL→3D at $\Gamma = 10^4$, $\epsilon = -4$, $\epsilon_{\text{sub}} = -2.22$. Above each roughness plot are three height maps of representative runs at the coverages $\Theta = 1, 10, 100$, respectively. The corresponding color bars are shown below the roughness plots.

The schematic growth modes described in Fig. 5.18 are illustrated by simulation results for the SOS model in Fig. 5.19.

5.5. Comparison to experiments

To put these previous results into context of experimental results, we can consider either molecular thin films (consisting of organic molecules) or atomic thin films (consisting of metals and semiconductors). Thin films in these two categories will show significantly different behaviors, since organic molecules are usually anisotropic, interacting mostly via (relatively weak) van-der-Waals interactions, while atoms are isotropic and typically interact more strongly.

For atomic thin films, we could be tempted to draw on the extensive catalog of experiments of heteroepitaxial growth of metallic and semiconductor thin films[110, 111]. However, such systems are usually crystalline, meaning they have a specific lattice constant. Due to this, elastic strain plays a non-negligible role. Such strain occurs due to lattice constant mismatch between the substrate material and the thin film. This can lead to growth behavior such as Stranski-Krastanov growth[112], where the film will initially grow in a LBL fashion, until the strain becomes too large and the surface “breaks”, leading to the formation of islands. This is problematic since (1) the lattice parameter is an intrinsic property of the material and cannot be modified and (2) lattice parameters of different materials usually do not match. One way around this is to look at experiments in which the substrate is amorphous, i.e. it has no lattice constant which could lead to strain. An example for this is growth of polycrystalline Al on Si(100), which initially exhibits LBL growth and shows roughening at later times[113] (Fig. 5.18(b)). AlCu on SiO₂ will, depending on the deposition rate, either form islands, which coalesce into a smooth film before roughening or form a smooth film from the start; again, in both cases the film roughens for long times[114] (Fig. 5.18(c),(d)). Sputter deposited Au on PS and PMMA will initially form islands which will coalesce into a rough film, roughening further for longer times[115] (Fig. 5.18(c)).

Despite the considerable role of strain in systems with crystalline substrates, some of the general growth scenarios presented in Fig. 5.18 can also be found here. Al grown on sapphire will initially show a high roughness which decreases at later times[116], which is reminiscent of Fig. 5.18(d). Al grown on Si(111), on the other hand, will grow in an LBL fashion before slowly roughening[117].

Molecular thin films do not present as many problems, since strain usually plays a negligible role there. All growth scenarios depicted in Fig. 5.18 can be found there. Pure 3D growth from the start can e.g. be observed for DIP grown on MoS₂[118] or pentacene grown on graphene[119]. LBL→3D growth, which in this case is not due to lattice strains, can usually be observed for growth on weakly interacting substrates like SiO₂, e.g. for pentacene[65, 120] or PTCDI-C_x[121, 122]. This growth mode is extremely common. Coalescence of islands and subsequent LBL growth (ISL→LBL), on the other hand, is rarely observed, e.g. during growth of rubrene on SiO₂[123]. For the ISL→3D mode, we were unable to find hard experimental proof. We suspect that C₆₀ on SiO₂ grows in this mode, but due to limitations of the XRR method (which can be used to measure the in-situ roughness of a growing film), only roughness data for the intermediate growth regime are available there. It is, however, known that C₆₀ forms islands on SiO₂, and the film roughness continually increases at later times.

In Fig. 5.20 we show experimental examples for the other three growth modes. These are all from growth experiments using organic molecules, and intriguingly they show a (compared to our simulations) very early onset of roughening. This kind of rapid roughening cannot be reproduced using our simple simulation models.

5.6. Conclusion

In this chapter we have investigated the growth modes of a thin film of cubic particles on a substrate of a different material. We investigated two models: A standard SOS model, in which particles were prohibited from desorbing from the film and cavities could not occur, and the colloidal growth model, in which particles were allowed to desorb and re-adsorb.

We have identified two transitions between growth modes, both of which are non-equilibrium transitions. The first transition occurs upon increasing the strength of the substrate interaction, leading to the growth mode of the film changing from forming islands to growing in a layer-by-layer fashion. This transition corresponds to the layering transition in an equilibrium. There we would expect the transition to occur at $\epsilon \approx \epsilon_{\text{sub}}$. For the non-equilibrium transition, however, we find that the value of the critical $\epsilon_{\text{sub, crit}}$ is shifted to lower energies, making this a dynamic layering transition. The exact value of $\epsilon_{\text{sub, crit}}$ now depends on ϵ , Γ , and E_{ES} , as opposed to only ϵ in equilibrium. The second transition is a transition in time, where in conditions under which the film initially forms islands on the substrate, these islands will coalesce at later times. Depending on the model and the exact system parameters, this can lead to several outcomes: The film might continue to grow in a LBL fashion, it might go towards a rough film with constant roughness, or it might continue to increase in roughness.

After very long deposition times, thin films will always start roughening, a phenomenon which is well-known in the literature for growth of thin films on substrates consisting of the same material. Since at some point all lattice sites will be covered in our simulations, each film eventually behave as if grown on a substrate of the same material.

Tying all these findings together, we were able to create a global phase diagram with four possible scenarios, show in Fig. 5.18. Films may start roughening from the beginning, they may grow in a LBL fashion before roughening, they may form islands and continue roughening after island coalescence, or they may form islands, then smooth after island coalescence before roughening again.

We have compared our results to previous experimental findings. For the growth of molecular thin films, consisting of organic molecules, we were able to identify all growth modes from our simulations and their dependence on substrate and temperature. This is despite the fact that our particles were isotropic, while organic molecules are usually anisotropic (one notable exception being C_{60}). This indicates that anisotropy might not always play a significant role in the evolution of roughness. The exception here is the strength and time of the onset of roughening. In experiments (as shown in Fig. 5.20) thin films will usually start roughening after deposition of only a few layers. This effect is significantly stronger and the onset earlier than we can reproduce using our models.

We suspected the anisotropic shape of those particles to be the origin of this roughening, since there one can usually observe ordering effects which simply cannot be captured by our isotropic model. Hence the next step was to expand this model in order to more accurately capture such effects (see next chapter). Additionally, the Ehrlich-Schwoebel barrier plays a significant role: In our simulations, we used $E_{ES} = 0$, which leads to relatively weak roughening. For finite values of E_{ES} , the roughening effects are stronger, but this leads to the initial LBL mode vanishing.

Comparisons to atomic thin films were also possible, albeit more complicated. In such systems, strain usually plays an important role if one is not careful to either match lattice constants of substrate and film or to use an amorphous substrate.

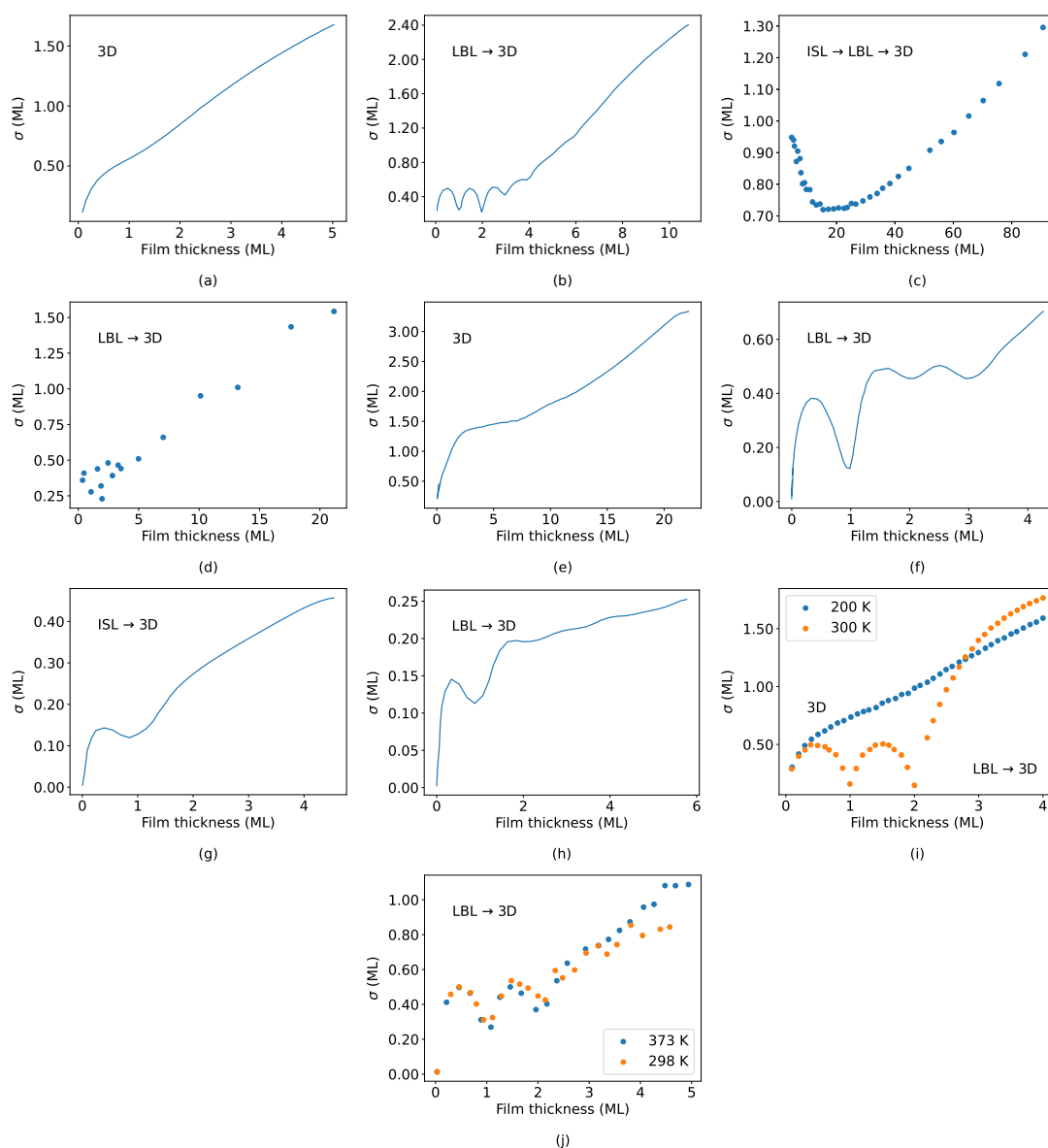


Figure 5.20.: Experimental in-situ roughness measurements exhibiting different growth modes. (a) tetracene on SiO_2 [124] ($1 \text{ ML} \equiv 13.4 \text{ \AA}$ [125]), (b) pentacene on SiO_2 [65] ($1 \text{ ML} \equiv 15.4 \text{ \AA}$), (c) rubrene on SiO_2 [123] ($1 \text{ ML} \equiv 13.4 \text{ \AA}$ in an orthorhombic polymorph crystal[126]; however, in these experiments the rubrene films were amorphous), (d) DIP on SiO_2 [64] ($1 \text{ ML} \equiv 17 \text{ \AA}$), (e) HBC on HOPG[59] ($1 \text{ ML} \equiv 3.37 \text{ \AA}$; reflectivity measurements indicate initial quasi-LBL growth), (f) PTCDI- C_8 on SiO_2 [122] ($1 \text{ ML} \equiv 20 \text{ \AA}$), (g) 6P and (h) 6P- F_4 on ZnO [40] ($1 \text{ ML} \equiv 26 \text{ \AA}$ in the 6P β -phase), (i) PTCDA on $\text{Ag}(111)$ [127], (j) 6T on SiO_2 [128]

Chapter 6.

Anisotropic interactions

The simulation results presented in this chapter have previously been published in Phys. Rev. E **105**, 045306 [129]

In the previous chapter, we focused on simulations of thin film growth of isotropic particles. We were able to identify roughness modes which corresponded well to those found in film growth of anisotropic organic molecules, indicating that anisotropy does not necessarily influence film roughness.

In the chosen region of $\mathcal{O}(10)$ deposited monolayers, the system of isotropic particles can, however, not yield more insights, due to its limited nature. Thus the next logical step was to extend the model. We chose to extend it by implementing anisotropic interactions between the lattice-isotropic, cubic particles in order to mimic the effects of anisotropic shape.

We chose to implement the anisotropy in this way since simulations of anisotropically shaped particles become quite tricky in the multilayer regime. On one hand, it is difficult to prevent cavity-rich films from occurring; hence, previous work usually focused on monolayers of e.g. rod-shaped molecules[35, 130]. On the other hand, shape anisotropy introduces a host of new parameters which need to be considered for translational and rotational moves.

In this chapter, we investigate how this anisotropy leads to ordering and re-orientation effects and how the grown films relate to those grown with isotropic interactions.

6.1. Model

As a basis for the model with anisotropic interactions we use the SOS model from Ch. 5. This means that each particle in the film always needs to be supported by either another particle or the substrate, and that no particle can desorb from the film.

We extend this model by giving each particle an internal “orientation” along either the x , y , or z axis. Depending on the relative positions of two neighboring particles and on their respective orientations, they can now interact with a strength $-\eta \cdot \epsilon$, where $\eta \geq 1$, or with a strength $-\epsilon$. The particle-substrate interaction strength is for the most part again $-\epsilon_{\text{sub}}$, but we will also discuss the case of a strongly interacting substrate.

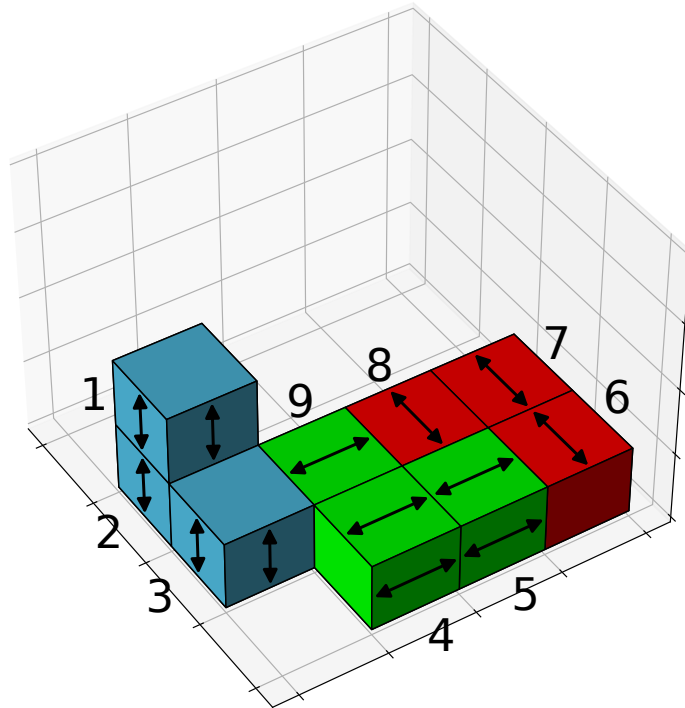


Figure 6.1.: Schematic representation of anisotropic nearest-neighbor interactions. The colors and arrows denote the orientations of particles.

In Fig. 6.1 we show a schematic representation of a few particles. We investigate two major ways in which to implement the interaction anisotropy:

- **Disc-like:** Particles interact strongly if their orientation vectors align and are parallel to the vector connecting the two particles. In Fig. 6.1, this would mean that particle pairs 1-2, 4-5, and 6-7 interact strongly, while all other pairs interact with strength $-\epsilon$.
This leads to particles stacking and forming “needles”, similar to what is observed in growth experiments for disc-shaped particles.
- **Rod-like:** Particles interact strongly if their orientation vectors align and are perpendicular to the vector connecting the two particles. In Fig. 6.1, this would mean that particle pairs 2-3, 4-9, and 7-8 interact strongly while all other particle pairs interact weakly.
This leads to the alignment of parallel particles, similar to what can be observed in growth experiments of rod-shaped particles.

This implementation of anisotropic interactions differs from e.g. the Lebwohl-Lasher model[131] for liquid crystals in that the interaction strength depends on the relative positions of particles (in the Lebwohl-Lasher model, all neighboring particles of identical

orientation will interact strongly). Most of the results shown in this chapter are for so-called disc-like interactions between particles.

The KMC simulations are then performed in a manner similar to those of the previous chapter, with the introduction of a new move. During each time step, either a new particle can be inserted with a rate F , or an already existing particle can attempt to either hop to a neighboring site with a rate D (with the restriction that the height difference between origin and target site is ≤ 1 layer) or to change its orientation vector, i.e. rotate, with a rate D_{rot} . These moves are then again accepted with a probability $p = \min(1, \exp(-\Delta E))$, where ΔE is the change in internal energy this move would cause. Both D and D_{rot} are again given in units of F .

For the implementation of the rotation moves, we investigate two different scenarios:

- **Model B:** Here, all particles, including those buried inside the film, can possibly rotate at any time. This implementation is the more intuitive one, since our particles are isotropic with respect to the lattice and thus no steric blocking of rotations can occur
- **Model S:** Only particles at the surface can rotate. This implementation is closer to the behavior of anisotropic molecules in growth experiments, which cannot rotate easily once they have been buried.

6.2. Effective Ehrlich-Schwoebel barrier

In these simulations, we again do not implement an explicit Ehrlich-Schwoebel barrier. The newly introduced interaction anisotropy does, however, lead to an effective, asymmetric ES barrier.

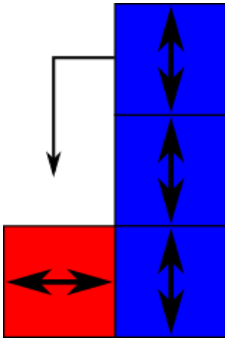


Figure 6.2.: Schematic illustration for the origin of the effective ES barrier

In Fig. 6.2 we schematically show the origin of this barrier in a system of disc-like interacting particles. For the top-most z particle to hop down, the change in internal energy is $\Delta E = 2\epsilon - \eta\epsilon$. For $\eta > 2$, this hop down becomes energetically unfavorable. The reverse, upwards hop, however, would be energetically favorable.

The results presented in this chapter show that for strong anisotropies, a strong roughening effect accompanied by the formation of z needles can be observed, which can probably be traced back to this barrier.

6.3. Observables

In addition to the morphology of the grown film, we are now also interested in the ordering inside the film. To measure this, we use the order parameter

$$\zeta = \frac{N_z - \frac{1}{2}(N_x + N_y)}{N_x + N_y + N_z} \quad (6.1)$$

where N_α is the number of particles oriented in direction α . This order parameter is frequently used to study the ordering of anisotropically shaped particles[132]. Its value ranges from -0.5 (if all particles are oriented in the x or y direction) to 1 (if all particles are oriented in the z direction). In an isotropic system, where all orientations are equally likely, it has the value 0 .

This value can also be calculated layer-wise, allowing us to measure order vs. height inside the film.

6.4. Mean-field calculations

As already indicated in Sec. 4.3, we can derive a mean-field approximation to predict equilibrium phase behavior for a system of particles with multiple possible orientations. The goal of these calculations is to investigate whether such an approximation is applicable in this scenario, and if so, how well it works.

We do this by equating the concentrations ($x_\alpha = N_\alpha/N$) of two of the three species, e.g. $x_x = x_y$, and then calculate when phase separation between these two species and the third, e.g. x_z occurs. Rather than writing the free energy as a function of T , we will write it as a function of energies which are $\propto 1/T$.

The free energy of a mixed system is defined as:

$$\Delta F_{\text{mix}} = \Delta E_{\text{mix}} - T\Delta S_{\text{mix}} \quad (6.2)$$

The internal energy in a system of three particle species is

$$\Delta E_{\text{mix}} = -n_{xx}\epsilon_{xx} - n_{yy}\epsilon_{yy} - n_{zz}\epsilon_{zz} - n_{xy}\epsilon_{xy} - n_{xz}\epsilon_{xz} - n_{yz}\epsilon_{yz} \quad (6.3)$$

where $n_{\alpha\beta}$ is the number of nearest neighbor pairs of species α and β , and $\epsilon_{\alpha\beta}$ the interaction strength between particles of species α and β .

To calculate the mixing entropy in such a three-component system, we assume that the lattice is completely filled. The number of possible configurations is then:

$$\Omega = \frac{N!}{N_x!N_y!N_z!} \quad (6.4)$$

where N is the number of lattice sites and N_α the number of particles oriented in the direction α . Consequently, we can calculate the entropy of this system using the Stirling approximation:

$$\begin{aligned} \Delta S_{\text{mix}} &= k \log \left(\frac{N!}{N_x!N_y!N_z!} \right) \\ &\approx -k(N_x \log x_x + N_y \log x_y + N_z \log x_z) \end{aligned} \quad (6.5)$$

6.4.1. 3D

Since in 3D the average inter-particle interactions are identical for all three species, we only differentiate interactions between particles of like and unlike species, ϵ_0 and ϵ'_0 . Translating these parameters to the system of anisotropically interacting particles yields:

- **Disc-like:** $\epsilon_0 = \frac{\eta+2}{3}\epsilon$, $\epsilon'_0 = \epsilon$
- **Rod-like:** $\epsilon_0 = \frac{2\eta+1}{3}\epsilon$, $\epsilon'_0 = \epsilon$

In a similar spirit to Flory-Huggins theory, we will here subtract the bulk energies of the pure systems, $E_0 = -\frac{z}{2}\epsilon_{xx}N_x - \frac{z}{2}\epsilon_{yy}N_y - \frac{z}{2}\epsilon_{zz}N_z$, from ΔE_{mix} . This is done purely to simplify the calculations and does not change the phase behavior, since it constitutes a shift by a constant. Thus we can substitute in Eq. 6.3:

$$\begin{aligned}\epsilon_{xx} &= \epsilon_{yy} = \epsilon_{zz} \equiv \epsilon_0 \\ \epsilon_{xy} &= \epsilon_{xz} = \epsilon_{yz} \equiv \epsilon'_0 \\ n_{\alpha\alpha} &= \frac{zN_\alpha - n_{\alpha\beta} - n_{\alpha\gamma}}{2}\end{aligned}$$

This yields

$$\begin{aligned}\Delta E_{\text{mix}} &= -n_{xx}\epsilon_{xx} - n_{yy}\epsilon_{yy} - n_{zz}\epsilon_{zz} - n_{xy}\epsilon_{xy} - n_{xz}\epsilon_{xz} - n_{yz}\epsilon_{yz} \\ &\quad + \frac{z}{2}\epsilon_{xx}N_x + \frac{z}{2}\epsilon_{yy}N_y + \frac{z}{2}\epsilon_{zz}N_z \\ &= (n_{xy} + n_{yz} + n_{xz})(\epsilon_0 - \epsilon'_0) \equiv \frac{kT(n_{xy}+n_{yz}+n_{xz})\chi}{z} \\ &= NkT\chi(x_x x_y + x_y x_z + x_z x_x)\end{aligned}\tag{6.6}$$

with

$$\begin{aligned}n_{\alpha\beta} &= zN_\alpha x_\beta \\ \chi &\equiv \frac{z}{kT}(\epsilon_0 - \epsilon'_0)\end{aligned}$$

Thus we obtain:

$$\begin{aligned}\Delta F_{\text{mix}} &= \Delta E_{\text{mix}} - T\Delta S_{\text{mix}} \\ &= NkT(\chi(x_x x_y + x_y x_z + x_z x_x) + x_x \log x_x + x_y \log x_y + x_z \log x_z)\end{aligned}\tag{6.7}$$

All three particle species behave identically, thus it plays no role which species is picked as the distinct one. We choose to set $x_x = x_y$. This yields:

$$\Delta F_{\text{mix}} = NkT(\chi(2x_z x_y + x_z^2) + x_z \log x_z + 2x_y \log x_y)$$

We now use $x_y = \frac{1-x_z}{2}$ and $f = \frac{\Delta F_{\text{mix}}}{NkT}$ to obtain:

$$f = \frac{\chi}{4} \left(-3x_z^2 + 2x_z + 1 \right) + x_z \log x_z + (1 - x_z) \log \frac{1 - x_z}{2}\tag{6.8}$$

And thus we obtain an equation which only depends on x_z and χ . The composition of the stable phase is again the one at which the free energy has its global minimum. Analytically determining the minima of such a function is no easy task. This is where Landau theory comes in useful, since finding the minima of a polynomial is considerably easier.

To analyze this function using Landau theory, we first rewrite it to depend on ζ using $x_z = \frac{2}{3}\zeta + \frac{1}{3}$. The reason for this is that for $\chi < \chi_c$, ζ will be 0, while it is nonzero for $\chi > \chi_c$; this is a requirement for Landau theory to apply. This rewrite yields:

$$f(\zeta) = \frac{1}{3} \left(-\chi\zeta^2 + 2\zeta \log(2\zeta + 1) - 2(\zeta - 1) \log(1 - \zeta) + \log\left(\frac{1}{27}(2\zeta + 1)\right) + \chi \right) \quad (6.9)$$

which can be written as a Taylor expansion up to the fourth order:

$$f(\zeta) \approx \frac{\chi}{3} - \log(3) + \left(1 - \frac{\chi}{3}\right)\zeta^2 - \frac{\zeta^3}{3} + \frac{\zeta^4}{2} \quad (6.10)$$

The stable phases are those where $\frac{\partial f}{\partial \zeta} = 0$, i.e.

$$\frac{\partial f}{\partial \zeta} = \zeta \left(6\zeta^2 - 3\zeta - 2\chi + 6 \right) \stackrel{!}{=} 0 \quad (6.11)$$

This yields two solutions:

1. $\zeta = 0$: This is the solution for $\chi < \chi_c$, i.e. below the phase transition
2. $\zeta = \frac{1}{12} (3 \pm \sqrt{48\chi - 135})$, for the position of the maximum and second minimum. This is the result for $\chi \geq 135/48$. However, when the second minimum initially appears, it is energetically less favorable than the one at $\zeta = 0$. Only for $\chi \geq \chi_c$ is this the absolute minimum of the free energy. To find the value of χ_c , we can use the condition that at coexistence the value of the free energy at both minima is identical, and that the first minimum will be at $\zeta = 0$, i.e.

$$\begin{aligned} f(\zeta_{\min,2}) &= f(0) = \frac{\chi_c}{3} - \log(3) \\ \Leftrightarrow \left(1 - \frac{\chi_c}{3}\right)\zeta_{\min,2}^2 - \frac{\zeta_{\min,2}^3}{3} + \frac{\zeta_{\min,2}^4}{2} &= 0 \end{aligned}$$

Using $\zeta_{\min,2} = \frac{1}{12} (3 + \sqrt{48\chi_c - 135})$, this yields:

$$\chi_c = \frac{17}{6} \approx 2.833 \quad (6.12)$$

χ_c is the critical point at which the system will undergo a first order phase transition. The transition being first order is evident from the fact that there is a jump between the compositions of the stable phases, from $\zeta = 0$ to $\zeta = 1/3$. As already stated, Landau theory only yields useful results close to the critical point. In order to determine the phase behavior further away from χ_c , it is more instructive to inspect the free energy

function itself, as shown in Fig. 6.3. From visual inspection of f , we find the value of χ_c to be closer to ~ 2.772 . This slight discrepancy from the value found using Landau theory can be explained by the fact that higher order terms are not taken into account in the Taylor expansion of f . Additionally, the second minimum at coexistence is now at $\zeta \approx 0.5$.

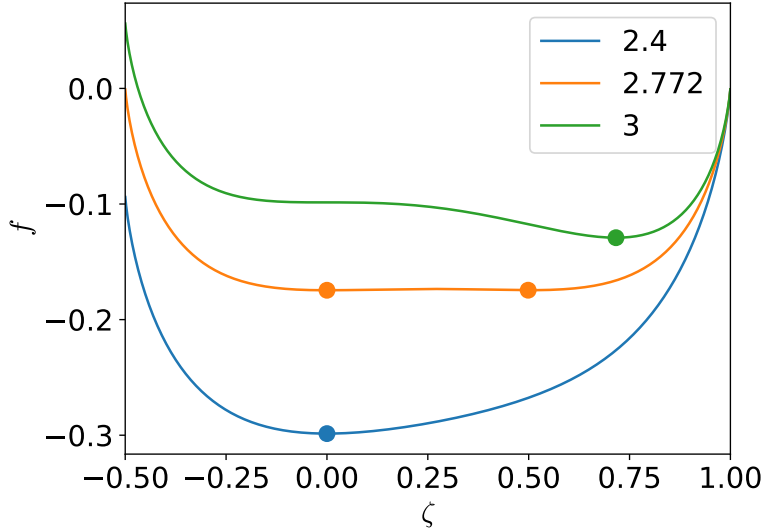


Figure 6.3.: Plot of f vs ζ in the three-component 3D system for three values of χ below, at, and above χ_c . Markers denote the absolute minima of f .

As expected, we find that for $\chi < \chi_c$, there is one minimum at $\zeta = 0$, i.e. the system is isotropic. At $\chi \approx \chi_c$, the free energy has two minima of equal depth, indicating that here phase coexistence occurs. For $\chi > \chi_c$, the free energy becomes non-convex. However, for $\chi > \chi_c$ there is only one point at which the free energy reaches this lowest value, indicating that it is energetically most favorable for the system to be at a high concentration of orientation z as χ increases. This indicates a first-order phase transition upon increasing χ from an isotropic system to one in which one species dominates. As we will show below, this matches very well our simulation results for rod-like anisotropy. For disc-like interactions, however, our simulations yield that demixing always yields a phase with two dominating particle species.

This discrepancy is due to the averaging nature of the mean-field approximation, which prohibits it from accounting for the anisotropy of the interactions. Consider a completely filled 3D box of disc-like interacting particles. Energetically, there is no difference between a system in which all particles are oriented in the same direction and one in which there are alternately oriented “sheets” of particles (e.g. in the x and y direction). Entropically, the latter is favorable and thus occurs more easily.

6.4.2. 2D

Apart from the 3D case, we want to investigate whether (and if so, how well) a mean-field description describes the ordering behavior in a 2D film, i.e. a monolayer. The monolayer case is especially interesting, since it might give us insight regarding the initial stages of film growth. We now investigate a completely filled 2D layer in which particles can assume all of the three orientations. The interaction parameters are now:

- **Disc-like:** $\epsilon_0 = \frac{\eta+1}{2}\epsilon$ for x and y particles, $\epsilon_0 = \epsilon$ for z particles, $\epsilon'_0 = \epsilon$
- **Rod-like:** $\epsilon_0 = \eta\epsilon$ for z particles, $\epsilon_0 = \epsilon$ for x and y particles, $\epsilon'_0 = \epsilon$

In the previous section we found that a mean-field approximation of our three-component system will show a first order phase transition. The question is whether this transition still occurs. Also, in the previous section we subtracted the bulk internal energy from ΔE_{mix} due to this making the calculations easier. In the 2D system, there is no clear way to subtract the bulk energy, since now the bulk energy of a pure z system differs from those where only x and y particles are present.

For disc-like interactions, we thus obtain

$$\begin{aligned}\Delta E_{\text{mix}} &= E_{\text{mix}} \\ &= -n_{zz}\epsilon - n_{xx}\frac{\eta+1}{2}\epsilon - n_{yy}\frac{\eta+1}{2}\epsilon - (n_{xy} + n_{yz} + n_{xz})\epsilon \\ &= \frac{(\eta-1)}{4}\epsilon n_{xz} + \frac{(\eta-1)}{4}\epsilon n_{yz} + \frac{\eta-1}{2}\epsilon n_{xy} - 2\epsilon N_z - (\eta+1)\epsilon N_x - (\eta+1)\epsilon N_y \\ &= N((\eta-1)\epsilon x_x x_z + (\eta-1)\epsilon x_y x_z + 2(\eta-1)\epsilon x_x x_y - 2\epsilon x_z - (\eta+1)\epsilon x_x - (\eta+1)\epsilon x_y)\end{aligned}$$

using $n_{zz} = \frac{zN_z - n_{xz} - n_{yz}}{2}$ etc. for $z = 4$. Due to the broken symmetry, particles oriented in the z direction now interact differently than those in the x and y directions. We are thus interested in the concentration of this species. Substituting $x_x = x_y = \frac{1-x_z}{2}$, we then obtain

$$f = -\frac{\epsilon}{2}(\eta + (\eta-1)x_z^2 - 2(\eta-1)x_z + 3) + x_z \log x_z + (1-x_z) \log \left(\frac{1-x_z}{2} \right) \quad (6.13)$$

In a similar way for rod-like interactions, we can obtain

$$f = -\frac{\epsilon}{2}(\eta + 5(\eta-1)x_z^2 - 2(\eta-1)x_z + 3) + x_z \log x_z + (1-x_z) \log \left(\frac{1-x_z}{2} \right) \quad (6.14)$$

Similarly to the results in the previous section, we can rewrite this function to depend on ζ and analyze the Taylor expansion using Landau theory. This yields for Eqs. 6.13 and 6.14:

$$f_{\text{disk}}(\zeta) \approx -\frac{2}{9}(\eta+8)\epsilon - \log(3) + \frac{4}{9}(\eta-1)\epsilon\zeta + \left(1 - \frac{2}{9}(\eta-1)\epsilon\right)\zeta^2 - \frac{\zeta^3}{3} + \frac{\zeta^4}{2} \quad (6.15)$$

$$f_{\text{rod}}(\zeta) \approx -\frac{2}{9}(2\eta+7)\epsilon - \log(3) - \frac{4}{9}(\eta-1)\epsilon\zeta + \left(1 - \frac{10}{9}(\eta-1)\epsilon\right)\zeta^2 - \frac{\zeta^3}{3} + \frac{\zeta^4}{2} \quad (6.16)$$

This functional form is more complicated than in the 3D case and reminiscent of that for a 2D system with an applied external field (see App. C). In such systems, the external field will often suppress the first order transition in favor of a second order transition. Note also that the sign of the linear term is opposite in both equations, i.e. z particles will be suppressed when implementing disk-like interactions and promoted by rod-like interactions.

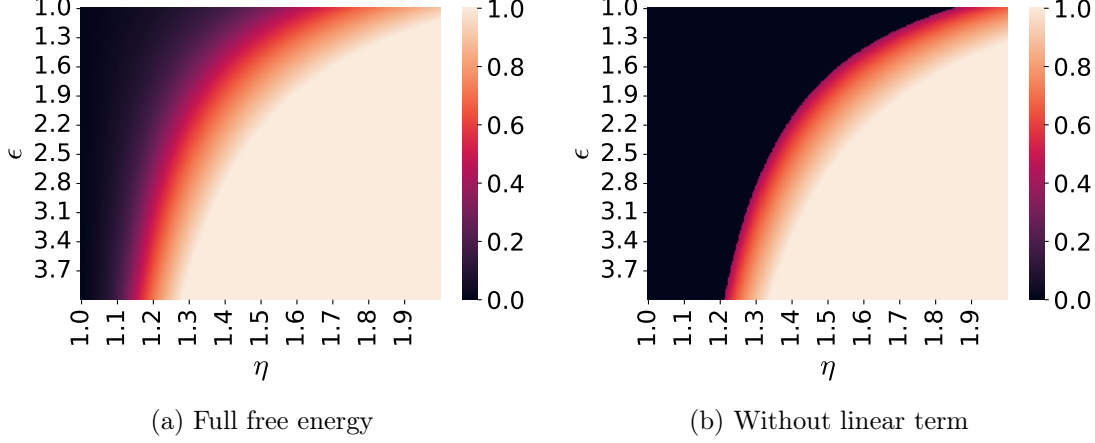


Figure 6.4.: Order parameter ζ at which the free energy from Eq. 6.16 has an absolute minimum (a) for the full free energy function and (b) for the free energy without including the term $-\frac{4}{9}(\eta - 1)\epsilon\zeta$

In order to determine whether a second order transition occurs, we plot the position of the value of ζ for the global minimum of Eq. 6.16 (for rod-like interactions) in the ϵ - η -plane in Fig. 6.4 for (a) the full free energy and (b) the free energy without including the linear term $-\frac{4}{9}(\eta - 1)\epsilon\zeta$. In Fig. 6.4(a), the minimum continuously shifts as η and ϵ increase, while in Fig. 6.4(b), a discrete jump from $\zeta = 0$ to a non-zero ordering is visible. This indicates that the three-component system on a 2D lattice will indeed exhibit a second order phase transition, due to the anisotropic interactions acting similarly to an external field. In both cases, ζ_{\min} will go from 0 to 1, i.e. the system transitions from an unordered state to one in which all particles are oriented in the z direction. Conversely, for Eq. 6.15 (disc-like interactions) we find a transition of ζ_{\min} from 0 to -0.5 .

Using this knowledge, we will now numerically analyze the minima of Eqs. 6.13 and 6.14. Since these systems will only exhibit a second order phase transition, it is sufficient to determine the position of the global minimum, i.e. $\partial f / \partial x_z = 0$:

- **Disc-like:** $\frac{\partial f}{\partial x_z} = \chi(1 - x_z) - \log(1 - x_z) + \log(2x_z) \equiv 0$
- **Rod-like:** $\frac{\partial f}{\partial x_z} = \chi(1 - 5x_z) - \log(1 - x_z) + \log(2x_z) \equiv 0$

where $\chi \equiv (\eta - 1)\epsilon$.

We now calculate χ for a range of values for $x_{z,\min}$ and then plot χ vs. $x_{z,\min}$ for both types of anisotropy in Fig. 6.5. In the system with rod-like anisotropy, $x_{z,\min}$ quickly

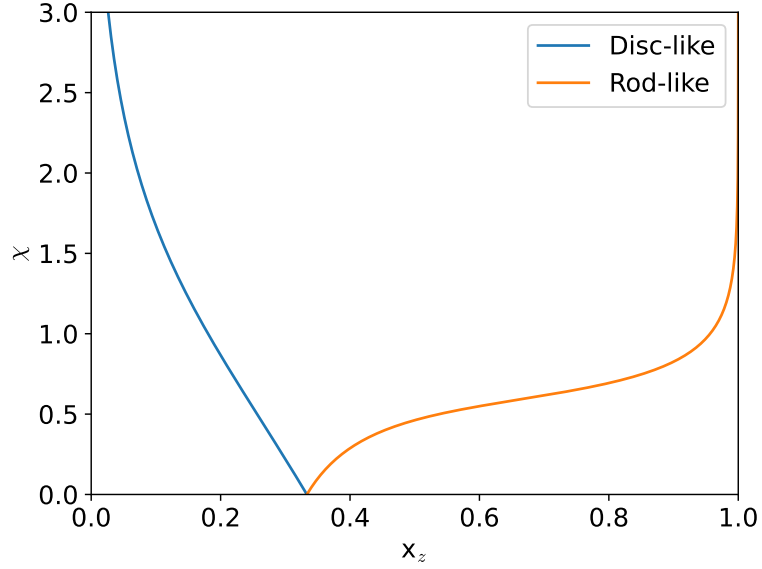


Figure 6.5.: χ vs $x_{z,\min}$ found by solving $\partial f(x_z)/\partial x_z = 0$ for disc-like and rod-like interactions. Disc-like interactions lead to the disappearance of z particles as χ is increased, while for rod-like interactions all particles quickly orient in the z direction.

goes towards 1, i.e. a state in which all particles are oriented in the z direction, as χ increases, while for the disc-like interactions $x_{z,\min}$ slowly relaxes towards 0, i.e. a state in which particles are only oriented in the x and y directions.

To test whether this fits simulation data, we can convert $x_{z,\min}$ and χ to ζ and η , respectively, as:

$$\zeta = x_{z,\min} - \frac{1}{2}(1 - x_{z,\min}) \quad (6.17)$$

$$\eta = 1 + \frac{\chi}{\epsilon} \quad (6.18)$$

We performed equilibrium simulations in a completely filled 2D lattice, where during each time step we attempted to rotate a randomly chosen particle. The value of η was varied from 1 to 3 for several values of ϵ , letting the system run for 10^{10} steps and extracting the average order parameter at each value of η .

In Fig. 6.6 we show the results compared to the respective mean-field calculations. While there are slight deviations, it is obvious that in this 2D three-component system the mean-field calculations yield very good results.

These findings indicate that during the initial stages of film growth, the film will be only ordered partially. As shown below, thick films will, however be oriented completely for strong enough values of η , i.e. an ordering transition vs. time occurs here.

Additionally, we find that, while in 2D the system will show a second-order phase transition, it will show a first-order transition in 3D. This is due to the fact that the

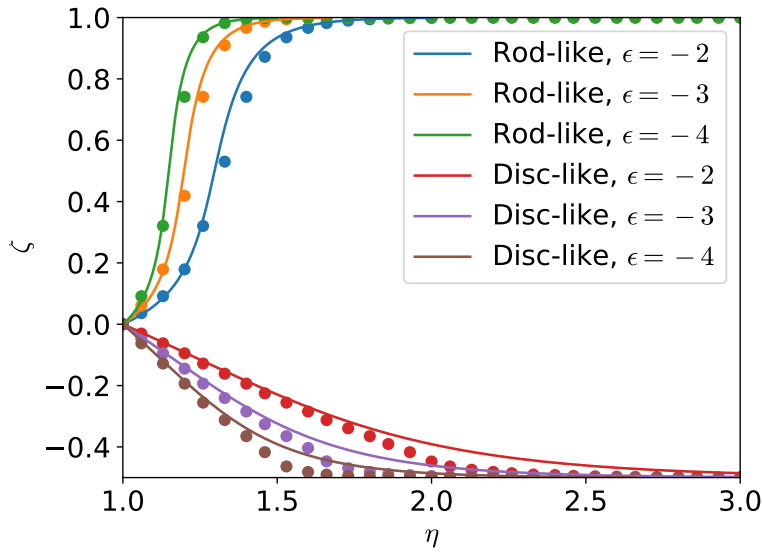


Figure 6.6.: ζ vs. η in equilibrium simulations for rod-like and disc-like interactions. The colored lines indicate the values predicted by mean-field calculations.

restriction to 2 dimensions is akin to applying a symmetry breaking field which disfavors z particles in the case of disc-like interactions and favors them for rod-like interactions., effectively suppressing the first order transition.

6.5. Simulations

Unless stated otherwise, all KMC results shown in this section were performed at $L = 256$ for **disk-like** interactions. ϵ is investigated in the range $-2 \dots -6$, D for $10^3 \dots 10^5$, and D_{rot} for $10 \dots 10^4$. As explained in the previous chapter, the values for ϵ and D are significantly lower than what we would expect them to be in growth experiments. However, we still assume that these will lead to qualitatively the same roughness behavior as the “real” parameters, provided the scaling relations still hold for anisotropic interactions. For the choice of values for D_{rot} there is no real justification. We chose for rotations to occur more slowly than diffusion since we assume that the energy barriers are stronger for rotations.

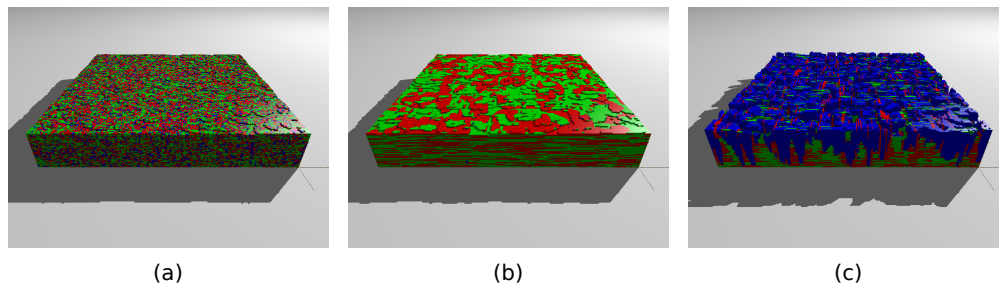


Figure 6.7.: Snapshots of films after deposition of 50 monolayers at $\epsilon = -3$, $\epsilon_{\text{sub}} = -3.11$, $D = 10^4$, $D_{\text{rot}} = 100$ in model S. Red, green, and blue indicate particles oriented in the x , y and z direction, respectively. The snapshots were taken for $\eta =$ (a) 1.5, (b) 2.5 and (c) 3.5

In Fig. 6.7 we show snapshots of KMC simulations of disc-like interacting particles after deposition of 50 ML for several values of η .

If η were 1, i.e. in an isotropic system, the system would show LBL growth under such conditions. At $\eta = 1.5$ (Fig. 6.7(a)), this is still the case. Additionally, the system is more or less isotropic, evidenced by the fact that all orientations occur approximately equally likely. Slightly increasing η to 2.5 (Fig. 6.7(b)), the film is still very smooth, while now there seems to be a depletion of blue particles (oriented in the z direction). This is due to the fact that at these parameters fibers of x - and y -oriented particles (x -fibers and y -fibers) start forming within the planes. These fibers are themselves relatively short and randomly distributed within the planes, leading to layers being relatively unordered. If we increase η even further to 3.5 (Fig. 6.7(c)) we can now observe the formation of long z fibers (blue), which reach throughout the whole film and lead to a significant increase in film roughness.

These two transitions (unordered to ordered and smooth to rough) were found to occur in both models and over wide ranges of parameters and will be analyzed below.

6.5.1. Growth modes

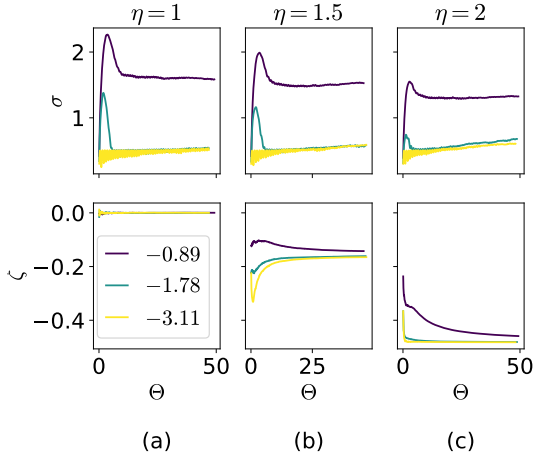


Figure 6.8.: Temporal evolution of roughness σ and order parameter ζ for $\epsilon = -3$, $\Gamma = 10^4$. $D_{\text{rot}} = 100$ and $\eta = 1, 1.5, 2$ for different ϵ_{sub} in model S

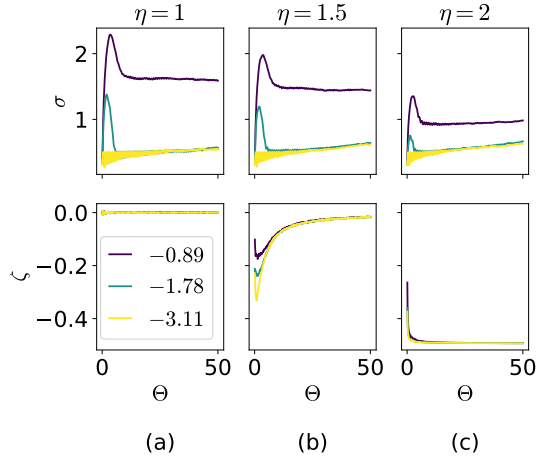


Figure 6.9.: Same as Fig. 6.8, but for Model B

First we investigate if and how the interaction anisotropy influences the growth modes described in the previous chapter for isotropic interactions. For such systems we found that the roughness evolution of thin films can be divided into four categories, depending on the parameters Γ , ϵ , and ϵ_{sub} :

1. LBL: smooth layer-by-layer growth
2. ISL \rightarrow LBL/CONST: initial island formation, followed by a reduced roughness
3. ISL \rightarrow 3D: initial island formation, followed by increasing roughness
4. 3D: Increasing roughness from the beginning

In the top rows of Figs. 6.8 and 6.9 we show typical examples of growth modes 1, 2, and 3 (depending on the value of ϵ_{sub}) for weak anisotropies. Growth mode 4 is not shown since, again, it mainly occurs at very low Γ or at strong E_{ES} .

From left to right we increase the value of η from 1 to 2. The growth modes of the thin films do not change upon increasing η , although the exact value of the roughness does change. For weak substrates ($\epsilon_{\text{sub}} = -0.89$), the film shows the ISL \rightarrow CONST growth modes, and the final roughness decreases as η increases. One might assume that for even stronger values of η , it will eventually go down to 0.5 and the film will go to the ISL \rightarrow LBL growth mode. As will be explained in more detail in the following sections, this does however not occur, since above a critical η_{trans} the particles will no longer be all

oriented in the x and y directions, instead now also forming long z -fibers, roughening the film in the process.

When looking at the values for the order parameter in the lower rows, however, it is obvious that the order parameter ζ undergoes a significant change upon increasing η . The film goes from completely unordered ($\zeta = 0$) at $\eta = 1$ to completely ordered in the x and y direction ($\zeta = -0.5$) for $\eta = 2$. At $\eta = 1.5$, in model B ζ will initially decrease (partial ordering) before returning to 0 at longer times. In model S the film will remain frozen in the partially ordered state, due to the fact that buried particles cannot rotate.

These findings indicate that for sufficiently weak anisotropies, roughness and ordering of thin films are independent of each other. Additionally, the value of ζ seems to be independent of ϵ_{sub} for long times. This is most likely due to the short-ranged nature of the substrate attraction, due to which the film behaves as one grown under homoepitaxial conditions as soon as the substrate is completely covered.

6.5.2. Equilibrium transition

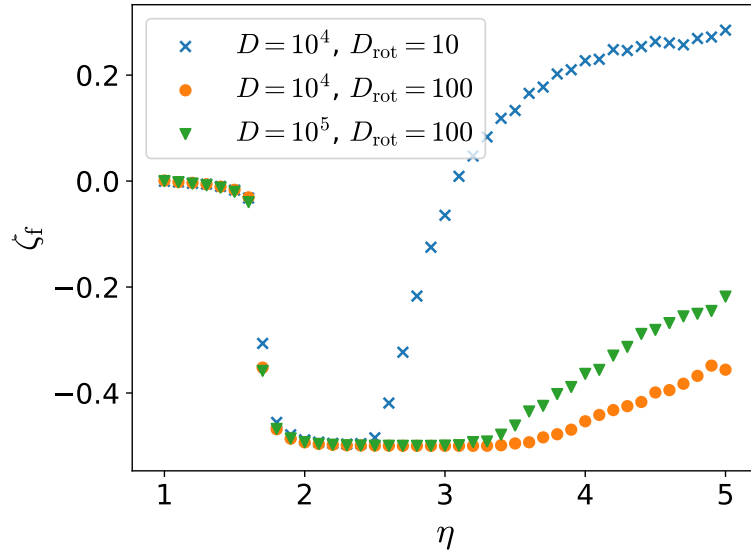


Figure 6.10.: ζ_{final} (ζ after deposition of 50 ML) vs. η for $\epsilon = -3$ and $\epsilon_{\text{sub}} = -4$ in model B. The isotropic \rightarrow ordering transition from $\zeta_{\text{final}} = 0$ to $\zeta_{\text{final}} = 1$ is independent of the kinetic parameters in the observed range.

As shown in Figs. 6.8 and 6.9, ζ will go from 0 to -0.5 upon increasing η , independent of the substrate. We suspected this to be an equilibrium ordering transition, i.e. independent of kinetic parameters. To confirm this, we performed η sweeps at different kinetic parameters and then plotted ζ after deposition of 50 ML ($\equiv \zeta_{\text{final}}$) vs η , as shown in Fig. 6.10. The cut-off of 50 ML was chosen arbitrarily as a “thick enough” film. From Figs. 6.8 and 6.9 it seems that for thicker films, ζ will not change noticeably for longer times.

It is evident from Fig. 6.10 that, at least in the range of used kinetic parameters, the transition from unordered to ordered is completely independent of the kinetics, indicating equilibrium behavior.

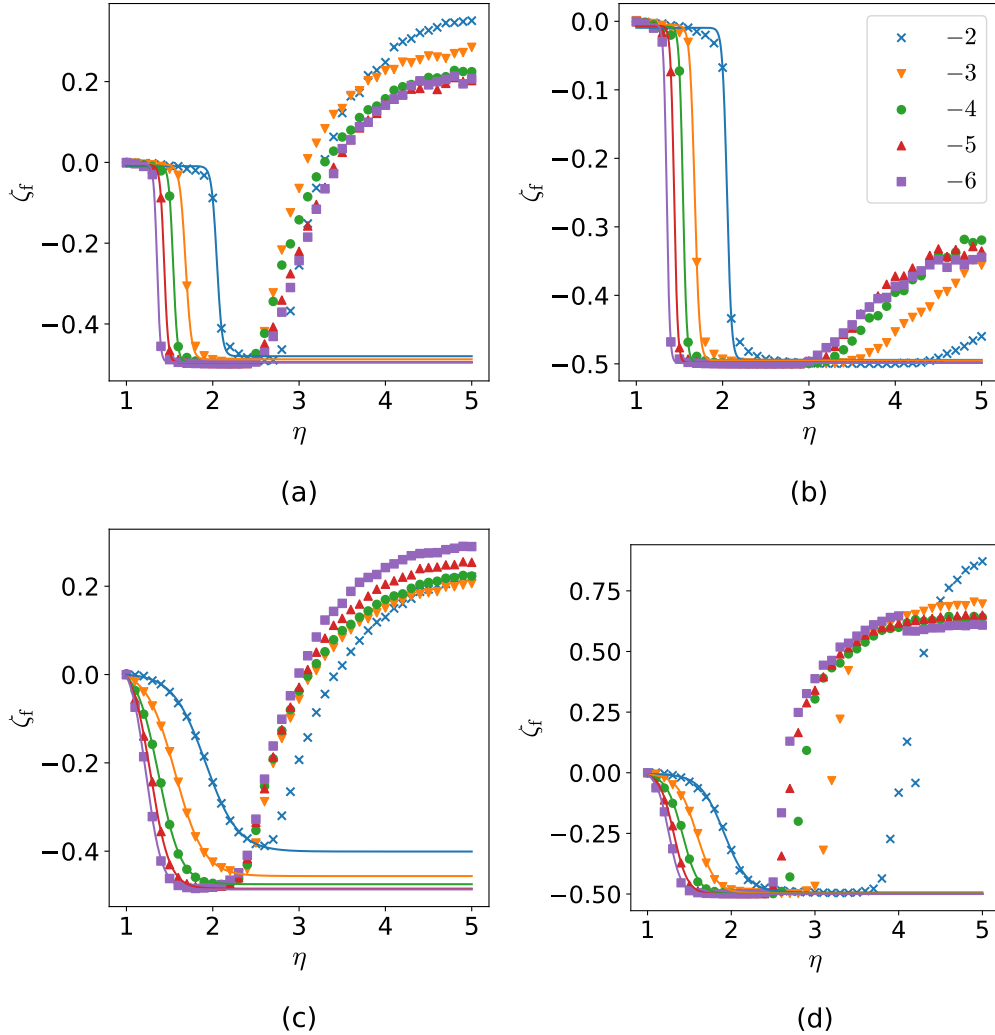


Figure 6.11.: Order parameter ζ_{final} vs η for different values of ϵ at $\epsilon_{\text{sub}} = -4$, $D = 10^4$ in model B ((a) and (b)) and model S ((c) and (d)) for $D_{\text{rot}} = 10$ ((a) and (b)) and $D_{\text{rot}} = 100$ ((c) and (d))

We can now again extract the transition point by fitting a tanh curve to the data points (here only to those points before the re-ordering transition at higher η) and extracting the inflection point as the transition point η_{crit} . This is shown in Fig. 6.11

In Fig. 6.12 we show the thus extracted values of η_{crit} for several values of ϵ , re-scaled to $(\eta_{\text{crit}} - 1)\epsilon$. The values are compared to those obtained in equilibrium Monte Carlo simulations performed by Nicolas Bader[129].

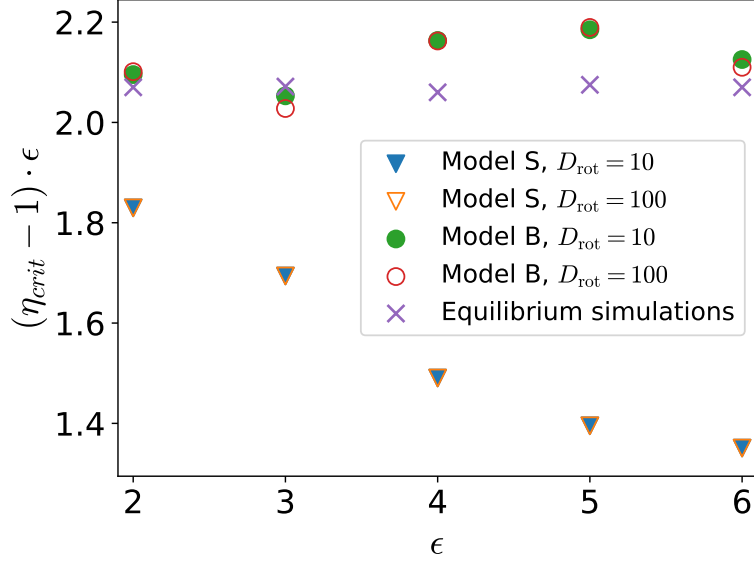


Figure 6.12.: η_{crit} for the unordered to ordered transition for several values of ϵ , re-scaled to $(\eta_{\text{crit}} - 1)\epsilon$, for both models. In model B, the transition occurs at the same point as in equilibrium, while in model S it is shifted slightly.

In those equilibrium simulations the re-scaled values are approximately constant, showing that η_{crit} scales as

$$\eta_{\text{crit}} = 1 + \frac{\chi}{\epsilon} \quad (6.19)$$

with $\chi \approx 2.07$. The extracted values of η_{crit} for model B are very close to these points, indicating that the transition in model B is indeed the equilibrium one. This makes sense, since in model B all particles are allowed to rotate at any time, allowing the film to equilibrate from any configuration. In model S, the extracted values for η_{crit} deviate from the equilibrium ones, being significantly lower.

6.5.3. Non-equilibrium transition

From Figs. 6.10 and 6.11 it is clear that if we increase η beyond η_{crit} , ζ_{final} will eventually increase again. The value of η at which this increase begins seems to now depend on the kinetic parameters (see Fig. 6.10), indicating that this is a non-equilibrium transition. The increase of ζ_{final} indicates that beyond this transition point, which we call η_{trans} , a significant fraction of the particles will be oriented in the z direction. Referring back to the snapshot Fig. 6.7(c), it is clear that this does occur, accompanied by the z particles now forming long z -fibers.

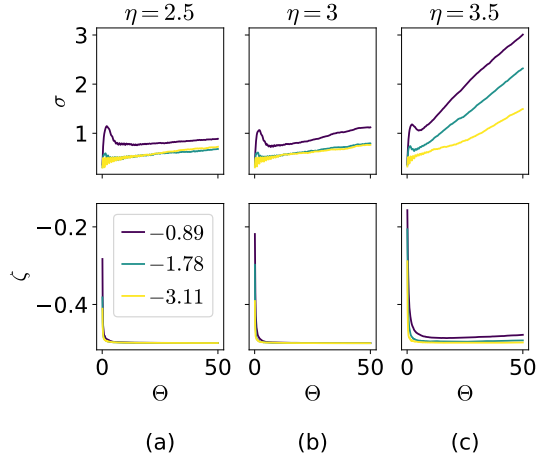
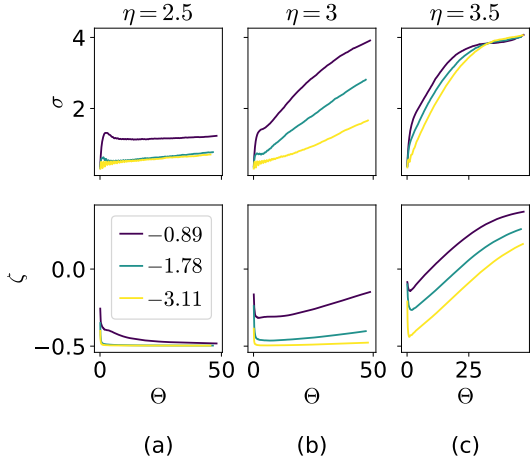


Figure 6.13.: Temporal evolution of roughness σ and order parameter ζ for $\epsilon = -3$, $\Gamma = 10^4$. $D_{\text{rot}} = 100$ and $\eta = 2.5, 3, 3.5$ for different ϵ_{sub} in model S.

Figure 6.14.: Same as Fig. 6.13, but for model B

In Figs. 6.13 and 6.14 we show how the evolution of ζ and σ changes as η is increased. For large values of η , we see that now both ζ and σ strongly increase with Θ . This can be seen in both models. We were now interested in the value η_{trans} at which this roughening and re-ordering transition occurs. As is already obvious from e.g. Fig. 6.11, ζ_{final} is not suitable for this purpose, since there is no clear point after which ζ_{final} increases, and a tanh fit similar to those performed in the previous sections is also not practical.

From looking at snapshots, we can however conjecture that the size distribution of the lengths of z fibers might be significantly changed during this transition, since it coincides with the appearance of large fibers.

In Fig. 6.15 we show the distributions of fiber lengths before and after the non-equilibrium transition. It is clear that before the transition, the distribution of z -fiber lengths is narrow, with the longest fiber being ~ 8 lattice sites long. After the transition, however, the distribution becomes very wide, with maximum fiber lengths up to 50 (i.e. fibers going from the substrate to the top of the film). Thus we now try to extract the transition point by using the width of this z -fiber distribution.

For each parameter set, we run 5 simulations (now at $L = 100$), create a distribution of all z -fibers in all 5 simulations, then determine the width of this distribution (excluding fibers of length 1), W_z . We take as the transition point η_{trans} the value of η at which W_z jumps to a significantly higher value.

In Fig. 6.16 we show ζ_{final} and W_z vs η . As noted earlier, ζ_{final} slowly increases, making it difficult to use this observable to quantify the transition point. W_z , on the other hand, shows a clear jump from ~ 1 to ~ 10 , allowing us to precisely quantify the location of η_{trans} , indicating that this observable is well suited to pinpoint the non-

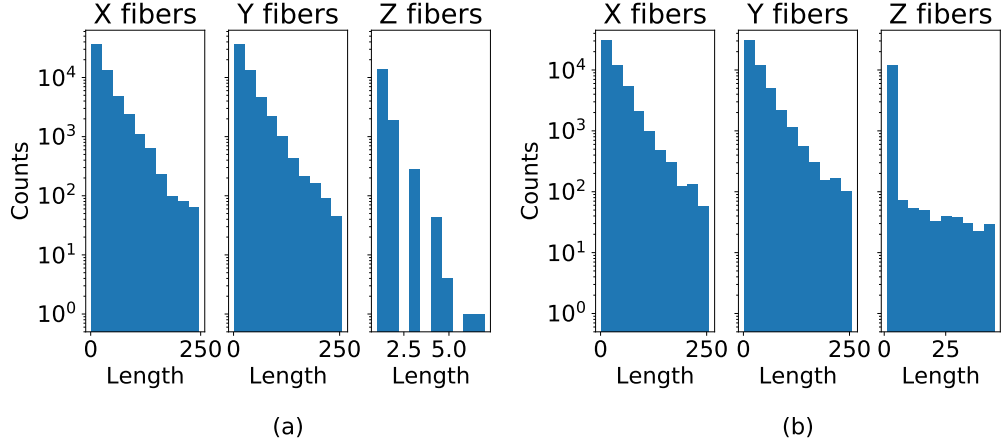


Figure 6.15.: Fiber length distributions in a film for $\Theta = 50$ (a) before and (b) after the non-equilibrium transition at $\epsilon = -2$, $D = 10^4$, $D_{\text{rot}} = 10$ and (a) $\eta = 2.6$, (b) $\eta = 2.7$. In the distribution of z fibers, it can be seen that the transition leads to the occurrence of long z needles.

equilibrium transition. Notable here is that this jump occurs at a lower value of η than one might choose when using the increase of ζ_{final} as the criterion for the non-equilibrium transition. This is due to the fact that shortly after the transition, there are relatively few long z -fibers, changing the value of ζ_{final} only slightly.

We now used this method to determine the value of η_{trans} at several values of D and D_{rot} , sweeping over several orders of magnitude, for both model B and model S. We found that this method works reasonably well in both models, for the most part. At very low values of D and D_{rot} , the exact transition point is not as clear as in Fig. 6.16, but still distinguishable. At very high values of D and D_{rot} , interestingly the transition seems to disappear completely in model B. There we were unable to see a deviation from the equilibrium ordering for values of η up to 10^5 , as shown in App.A

In Fig. 6.17 we show a heatmap of η_{trans} as a function of D and D_{rot} in model S. Even though the kinetic parameters range over several orders of magnitude, the value of η_{trans} shifts only slowly, going from ~ 2 to ~ 4 .

Putting together the results of the previous two sections, we can now construct a “dynamic phase diagram” in the $\epsilon_{\text{sub}}\text{-}\eta$ plane at a given value of ϵ , of which we show an example in Fig. 6.18 for $\epsilon = -3$.

The diagram of growth modes from the previous chapter is expanded into a new dimension showing the film ordering. For $\eta \lesssim 1.6$ (i.e. $\eta < \eta_{\text{crit}}$), the film remains unordered and we recover the “simple” growth modes from the isotropic system. In general we find that for $\eta \lesssim 2.4$ (i.e. $\eta < \eta_{\text{trans}}$, below the non-equilibrium transition), roughness and film ordering are completely independent of each other, and for higher values of η the system shows the new roughness growth mode caused by the formation of long z -fibers.

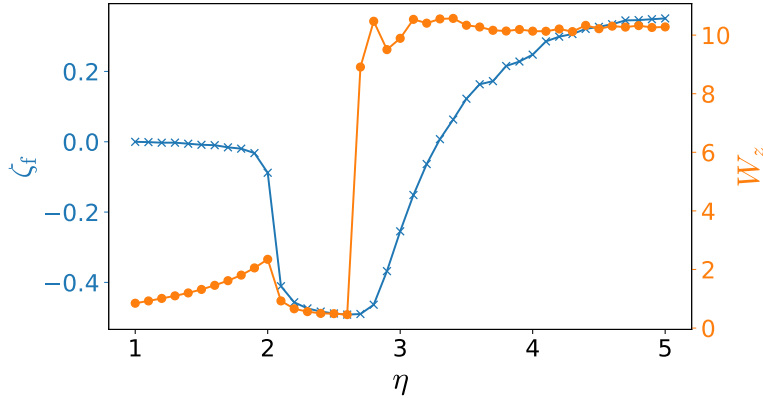


Figure 6.16.: Comparison of ζ_{final} and W_z vs η after deposition of 50 monolayers for $\epsilon = -3$, $\epsilon_{\text{sub}} = -4$, $D = 10$, and $D_{\text{rot}} = 100$ in model S. W_z shows a discrete jump which corresponds to the non-equilibrium transition. This occurs slightly before ζ_{final} changes.

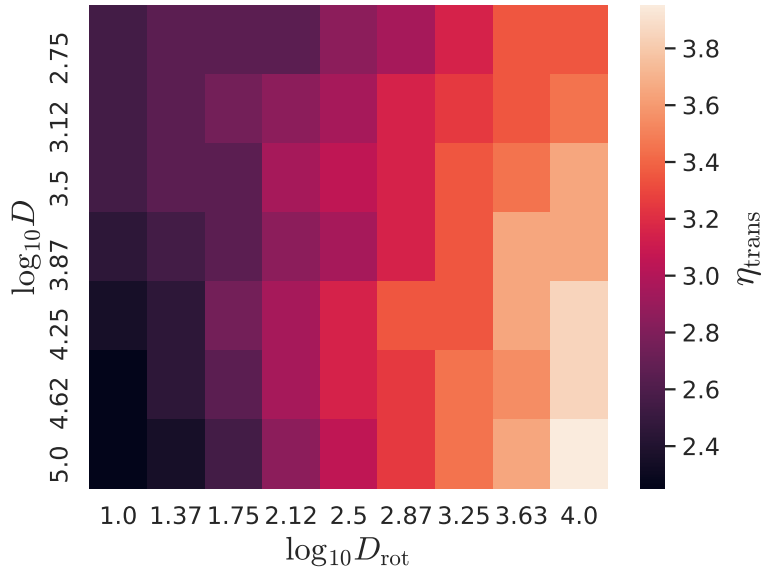


Figure 6.17.: Heatmap showing the value of η_{trans} for the non-equilibrium transition at different kinetic parameters ad $\epsilon = -3$ in model S. Increasing D and D_{rot} leads to a higher value of η_{trans} . Even so, when the kinetic parameters are varied over several orders of magnitude, the value of η_{trans} only approximately doubles.

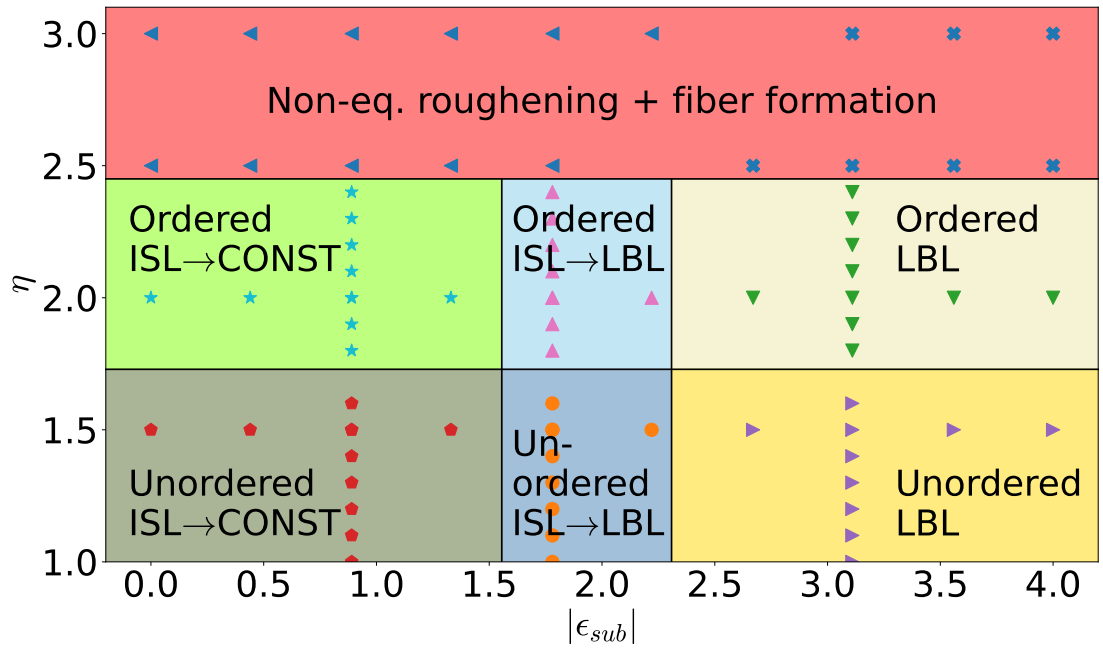


Figure 6.18.: Modified growth mode diagram for $\epsilon = 3, D = 10^4, D_{\text{rot}} = 10$ in model S. The simulated parameter sets are denoted by symbols, background colors mark the approximate extent of the respective growth modes. For weak anisotropies ($\eta < \eta_{\text{trans}}$), roughness and ordering behavior are independent of each other, leading to separate regions. For strong anisotropies ($\eta > \eta_{\text{trans}}$), non-equilibrium roughening behavior occurs, changing both the ordering and roughness.

6.6. Model variations

The results shown so far are all for a system of disc-like interacting particles growing a film on a substrate which interacts equally strong with particles of all orientations. We now want to briefly discuss two obvious extensions of the model.

6.6.1. Strongly interacting substrate

In addition to the orientation-agnostic (“weakly-interacting”) substrate from the previous sections, we now implement a “strongly-interacting” substrate. Here the substrate interaction of z oriented particles becomes $-\eta \cdot \epsilon$, while for other orientations it remains $-\epsilon_{\text{sub}}$. This substrate interaction anisotropy was chosen to mimic substrates preferring e.g. disk-like particles lying down flat.

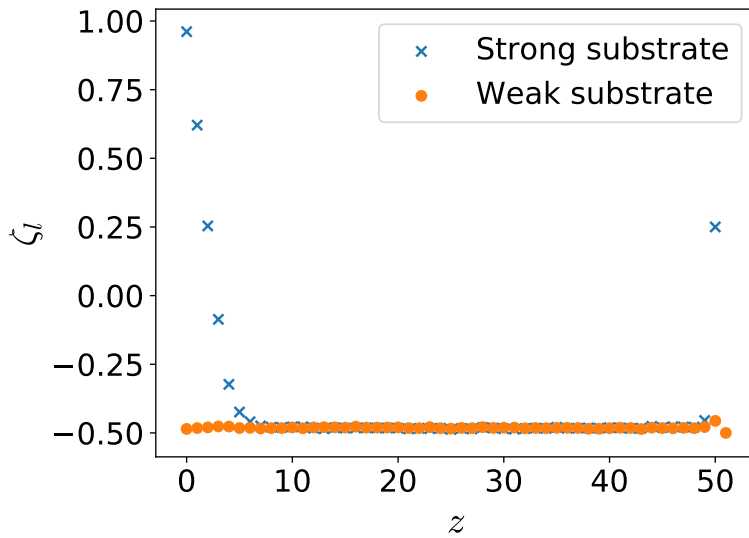


Figure 6.19.: Layer-wise ordering ζ_l vs layer z after deposition of 50 ML in model S for $\epsilon = -3, \eta = 2$. We compare substrates where (1) all orientations interact equally strongly with the substrate (“weak”) and (2) z oriented particles interact with strength $\eta \cdot \epsilon_{\text{sub}}$ with the substrate (“strong”). On the strong substrate, all particles in the lowest layer are oriented in the z directions. ζ_l then slowly relaxes towards -0.5 as z increases. On the weak substrate, all layers are perfectly ordered in parallel to the substrate.

In Fig. 6.19 we show an example for moderate anisotropy ($\eta = 2$). Particles in the lowest layers will now all be oriented in the z direction ($\zeta_l = 1$), slowly relaxing towards the equilibrium orientation in higher layers (in contrast to this, ζ_l will be -0.5 in all layers for films grown on the weakly-interacting substrate). The increase of ζ_l in the highest layers is due to these layers not being completely filled.

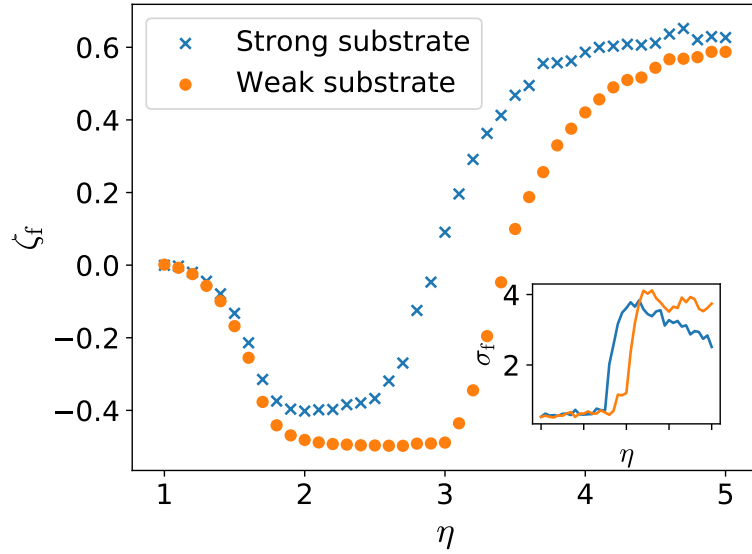


Figure 6.20.: Comparison of the final ζ_{final} vs η after deposition of 50 ML between strong and weak substrate for $\epsilon = -3$ in model S. The isotropic \rightarrow ordered transition occurs approximately at the same η . The non-equilibrium roughening transition, however, occurs earlier on the strong substrate. This is due to the fact that there, all particles in the first layer will be oriented in the z direction, which act as nucleation sites for the formation of needles. In the inset we show the results for σ_{final} , where a similar trend can be observed.

Due to this relaxation of ζ_l , the value of ζ_{final} will never truly reach -0.5 , as shown in Fig. 6.20. Additionally, this figure shows that the non-equilibrium transition is shifted to lower values of η upon switching from the weakly to the strongly interacting substrate. This is a consequence of the fact that the lowest layers on the strongly interacting substrate will now be filled by z -oriented particles, acting as nucleation sites for the formation of z -fibers and consequently enhancing the roughening growth mode.

6.6.2. Rod-like interactions

As indicated earlier, we can also implement the interaction anisotropy to mimic rod-shaped molecules (e.g. pentacene). This is realized by letting NN particles interact strongly if their orientations are identical and perpendicular to the vector connecting the particles (see description in Sec. 6.1).

For these systems we found the ordering behavior to be the inverse of the one found for disc-like molecules, as seen in Fig. 6.21. Inverse behavior means that, upon increasing η from 1 (Fig. 6.21(a)), the system will first go from an unordered state to one in which all particles are oriented in the z direction (\equiv standing-up rods, Fig. 6.21(b)). When η is increased even further, we again find a non-equilibrium roughening transition, this time accompanied by particles orienting in the x and y directions (\equiv lying-down rods,

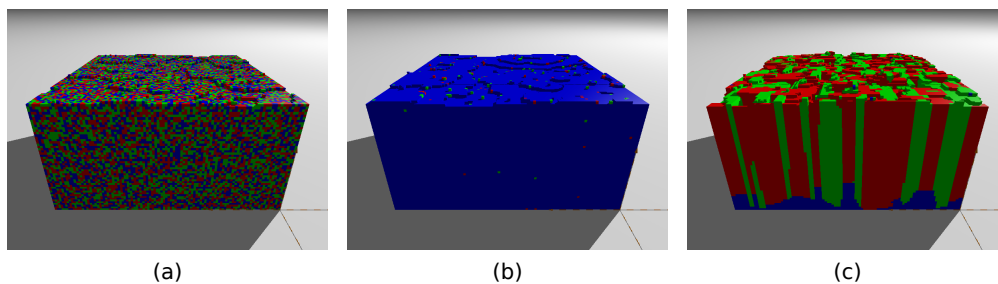


Figure 6.21.: Snapshots after deposition of 50 ML at $\epsilon = 3$, $\epsilon_{\text{sub}} = 3.11$, $D = 10^4$, $D_{\text{rot}} = 100$ in model S for rod-like interactions at $\eta =$ (a) 1, (b) 1.6, (c) 3. Red, green, and blue particles are oriented in the x , y and z direction, respectively. Upon increasing η , the film will initially go from an isotropic state to one in which all particles are oriented in the z direction. Upon increasing η even further, sheets consisting of x and y particles start forming, leading to a rough film.

Fig. 6.21(c)). These lying-down particles then form “sheets” which consolidate into large, compact blocks.

In Fig. 6.22, we show ζ_{final} and σ_{final} vs. η at different values of ϵ . It is evident that rod-like interactions lead to an ordering opposite to the one found for disk-like interactions, i.e. to a state where all particles are oriented in the z direction. Upon increasing η further, again an equilibrium transition will occur, leading to a decrease of ζ_{final} . Qualitatively, these are the same transitions as found for disc-like interactions. In the non-equilibrium roughening regime, σ_{final} seems to be independent of the value of ϵ . The final roughness is similar to the one found for disc-like interactions, now due to the occurrence of sheets consisting of x and y particles which lead to a strong roughening of the film (for snapshots see Fig. 6.21).

In simulations and experiments using rod-shaped molecules, it was found that the anisotropic particle shape plays a significant role in the ordering of the film. Depending on the molecules used and the exact growth conditions, one can also find there a standing-up transition (similar to our ordering transition from $\zeta = 0$ to $\zeta = 1$). However, in simulations it was found that this occurred due to the anisotropic shape of the particles, where rods would lie down at low layer filling and only stand up at higher filling[35].

6.7. Comparison to experiments

The extension of the SOS model with anisotropic interactions has thus lead to new ordering effects. These anisotropic interactions were implemented in the first place in an attempt to mimic the anisotropic shape of organic molecules, hence it is instructive to compare our findings to those of experiments.

We mainly used the interaction anisotropy to model disc-shaped molecules. Corresponding molecules used in organic thin film experimental studies are hexa-*peri*-hexabenz-

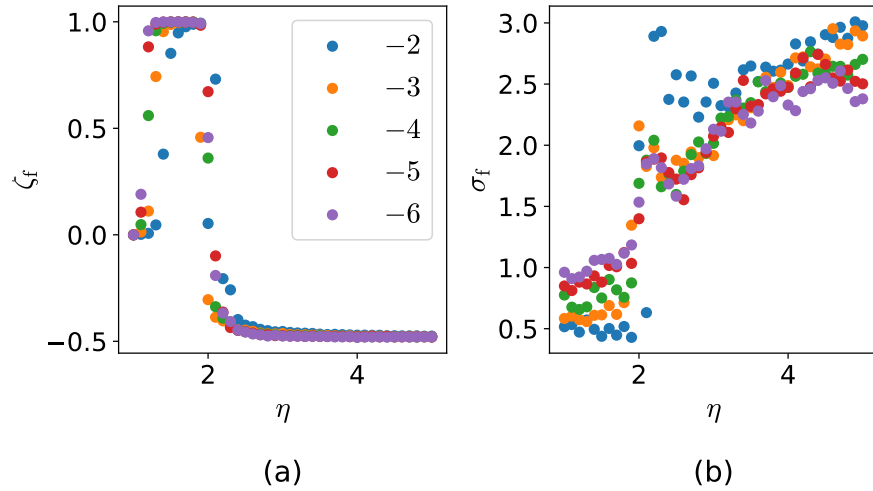


Figure 6.22.: (a) ζ_{final} and (b) σ_{final} after deposition of 50 ML vs η at $\epsilon_{\text{sub}} = 4$, $D = 10^4$ and $D_{\text{rot}} = 100$ for different ϵ in model S.

coronene (HBC), phthalocyanines (e.g. CuPC and ZnPC), benzene, and perylene. These particles will, given the right conditions, form needles or stacks, similar to particles in our simulations at strong enough anisotropies. The variety of possible structures is of course larger than in our orientation restricted model. Stacking structure there include e.g. herringbone or π - π stacking[133].

The growth direction and ordering of such needles also strongly depends on the substrate. The main distinction can be made here between amorphous substrates, such as SiO_2 (corresponding to a weakly interacting substrate in our work) and ordered substrates, such as metal surfaces (corresponding to a strongly interacting substrate).

Disc-like particles grown on an amorphous substrate will stand up on the substrate. Phthalocyanines will arrange in a herring-bone structure and form needles growing perpendicularly to the substrate[57], while HBC on SiO_2 will form a polycrystalline film consisting of standing molecules[59]. On metallic (ordered) substrates, on the other hand, disc-like particles in the first layer will lie down flat on the substrate, subsequently forming needles growing perpendicularly to the substrate. This has been found for growth of perylene on copper[58] and for HBC on various metallic substrates[60] and HOPG (highly ordered pyrolytic graphene)[59]. These results are of course reminiscent of the behavior found in our simulations for disc-like particles grown on weakly and strongly interacting substrates, respectively. Benzene particle grown on a substrate modified by a self-assembled monolayer (SAM) will either form needles throughout the whole film, or form an ordered structure in the first layer and a polycrystalline film in higher layers[61]. The latter behavior can also be found for a benzene derivative grown on HOPG[62]. This behavior of ordering at short times and disordering at long times is similar to our results for films grown with relatively low anisotropy ($1 < \eta < \eta_{\text{crit}}$), judging from the ζ vs Θ curves.

In an experiment, varying just the inter-particle or the substrate-particle interaction is not easy to achieve. In most cases, the only control parameter here is the substrate temperature T . In Ref. 134 benzene was deposited onto gold-coated copper at different substrate temperatures. It was found that upon increasing T , the film will go from an amorphous to a partially ordered to a completely ordered state. This is in contrast to our findings that when keeping η constant and decreasing ϵ (increasing T), the film will go from the partially ordered non-equilibrium roughened phase to the completely ordered equilibrium phase. However, changing T does not only change the value of ϵ , but also those of ϵ_{sub} , D , and D_{rot} in a non-linear manner. Due to this the correspondence between experiments and simulations is not always immediately obvious.

It is unclear whether the formation of perpendicularly growing needles as found in experimental studies is accompanied by the type of rapid roughening which we observe in our simulations. The in-situ roughness evolution of films of disc-shaped particles is not often measured, being often omitted in favor of reciprocal space maps. Examples which we could find include the growth of CuPC on SiO₂[135] and of F₁₆CuPC on SiO₂[136], which both show initial LBL growth followed by rapid, strong roughening. Simultaneously, a change in grain sizes is observed. However, for these results there is no information on the molecular orientation during film growth. The roughening effect could as well be produced by a strong ES barrier.

While for disc-like molecules the number of studies is limited, a wide variety of data and observations can be found for thin film growth with rod-like molecules, especially pentacene (PEN) and diindenoperylene (DIP). These molecules will show a rapid roughening behavior (see Fig. 5.20) which cannot be explained using rod-like interactions in our model. On SiO₂ at high temperatures, molecules of these species will initially stand up on the substrate forming a smooth film, with the film later breaking up and strongly roughening [63, 64, 66, 67, 137]. Growth of DIP on SiO₂ at low temperatures[63] or on gold[68] will, however, lead to particles lying down and forming a rough film, which is reminiscent of our results, see Sec. 6.6.2. Pure pentacene films will not show this effect, while a 1:1 mixture of pentacene and perfluoropentacene does[138]. All in all, the comparison of results from our model to those from experiments is more complicated here, since the shape of rod-like molecules is highly anisotropic, leading to a stronger influence of steric interactions on the morphology.

6.8. Conclusion

We have extended the lattice SOS model for film growth from the previous chapter by introducing anisotropic interactions, where the interaction anisotropy depended upon the orientations and relative positions of the particles. The anisotropy was chosen in a way to model the anisotropic interactions between anisotropically (disk-like or rod-like) shaped particles, where the strength of interactions between neighboring particles could be increased by a factor $\eta \geq 1$. Along with these anisotropic interactions, we introduced a new rotation move with a corresponding rate D_{rot} . For these rotations, we distinguish two scenarios: Model B, where all particles within the film can rotate at any

time, and model S, where only particles at the surface can rotate. If the anisotropy is small ($\eta < \eta_{\text{trans}}$), the roughness growth modes presented in the previous chapter will still occur. We find in this regime that upon increasing the value of η , the growth mode of the film is unchanged, while particles will orient themselves in parallel or perpendicularly to the substrate for disk- and rod-like interactions, respectively. In model B, this ordering transition is independent of the kinetic parameters and occurs at the same value of η as a first order ordering transition in a 3D equilibrium system. In model S, the location of the transition depends only weakly on the kinetic parameters and is still close to the equilibrium position. However, the transition is now for most kinetic parameters not to a state in which all particles are ordered.

At strong anisotropies ($\eta \geq \eta_{\text{trans}}$), the roughness evolution of the thin film changes. Films will now exhibit a strong roughening. The location of this roughening transition now depends on the kinetic parameters, making it non-equilibrium. For disk-like interactions, this is due to the occurrence of needles perpendicular to the substrate, while for rod-like interactions, “sheets” of x and y particles will start forming. These new structures change both the ordering and the roughness of the film.

In model B, the transition can disappear close to equilibrium (i.e. for high values of D and D_{rot}). For film thicknesses smaller than the lateral lattice size, it is e.g. for disk-like interactions energetically more favorable for all particles to orient in parallel to the substrate. Since in model B particles can rotate at any time, they are at sufficiently high D and D_{rot} always able to reach this stable state. Conversely, in model S particles cannot rotate once they are buried. This prevents all particles from rotating, providing nucleation sites for z needles to start growing. Thus this non-equilibrium transition will always occur there.

Chapter 7.

Binary systems

In addition to simulations of a species of anisotropically interacting particles, simulations of binary films are of significant interest, since these are also the subject of a wide variety of experimental studies[139, 140, 141]. Such mixed films show a large variety of new behavior: Depending on the interaction energies, the particle species might intermix or phase separate[142], and the sizes of these demixed domains can vary drastically depending on temperature, deposition flux etc. The roughness evolution might significantly differ from those of the pure components and new morphological features might emerge (see next section).

Binary thin films play an important role in many manufacturing processes. Most notable here are donor-acceptor thin films comprised of semiconducting organic molecules. These are used in the manufacturing of organic solar cells[4]. Since electronic properties sensitively depend on the morphological properties, a precise control of the film structure is desirable.

In simulations of binary systems, there is an additional energetic parameter ϵ' , denoting the interaction strength between particles of different species. Furthermore, one can also assign each of the two species an own ϵ_α for interactions between two particles of species α , as well as a species-dependent substrate interactions $\epsilon_{\text{sub},\alpha}$ and diffusion coefficient D_α , complicating the investigation of such systems even more.

Extending the KMC simulations to incorporate two particle species is relatively straightforward:

- Any time a deposition move is chosen, generate a random number to determine the species of the new particle. E.g. for a desired concentration of species 1 $c_1 = 0.5$, the new particle is of species 1 if $r \leq 0.5$, with a random $r \in [0, 1]$.
- Any time a diffusion move is proposed, check the species of all neighboring particles in order to properly calculate the energy barrier ΔE

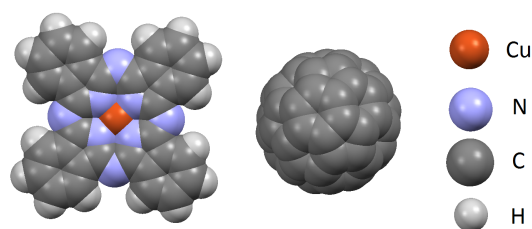


Figure 7.1.: (Left) Copper phthalocyanine (CuPC) molecule, (right) Buckminster Fullerene (C_{60}) molecule. Figure by courtesy of B. Reisz

In this chapter, we present two ansatzes for binary systems: The study performed in Ref. [135], where we used simple isotropically interacting particles, trying to recreate the film morphology by using Ehrlich-Schwoebel barriers which depend on the local environment of the particle, as well as preliminary results for a binary film incorporating anisotropic interactions. In both of these studies, the focus is on recreating the film morphology for a CuPC: C_{60} blend. In Fig. 7.1 we show the structure of these two molecules. There we see that CuPC is relatively flat, while C_{60} is “football-shaped”, i.e. approximately round.

7.1. Species-dependent Ehrlich-Schwoebel barrier

The results of this section have been previously published in Phys. Rev. Mat. 5, 045601. The author of this thesis did not perform the simulations presented in this section. [135]

In growth experiments, it was found that co-depositing CuPC and C_{60} at 310 K will lead to a film which is smoother than pure films of either particle species, while at 400 K the grown film will be significantly rougher. One conjectured explanation for this is the reduction of the ES barrier for inter-layer diffusion in a mixed system, due to a higher number of possible pathways around the edge, leading to different roughening mechanisms at different diffusion speeds.

To test this hypothesis, we modified the SOS model from Ch. 5 such that the species onto which the hopping particle would move is checked before each inter-layer hop. If both particles are of the same species (which is always the case in a one-component system), the ES barrier is $E_{ES} = E_{ES}^{11} = E_{ES}^{22}$ for species 1 and 2, respectively. If, in a two-component film, the two particles are of different species, the ES barrier for such a hop would be E_{ES}^{12} . The other energetic and kinetic parameters were chosen such that pure films of species 1 and 2 mimic the general growth behavior of CuPC and C_{60} films, respectively.

In Tab. 7.1 we show the parameters used in these simulations. This table shows that inter-layer hops are unrestricted for hops onto a particle of a different species, but severely limited otherwise.

The ratios $\Gamma = D/F$ were chosen in such a way to mimic the change in temperature in experiments when going from $T = 310K$ to $T = 400K$, since $F = \text{const.}$ and $D \propto k_B T \exp(-E_D/k_B T)$. This is a valid choice if the diffusion barrier $E_D \approx 11k_B T$, which is a realistic value for organic molecules (see e.g. our calculations for C_{60} in Ch. 5; also note

7.1. Species-dependent Ehrlich-Schwoebel barrier

Parameter	Value
$\epsilon_1 = \epsilon_2$	-3
$\epsilon_{\text{sub},1}$	-2.7
$\epsilon_{\text{sub},2}$	-1.0
$E_{\text{ES}}^{11} = E_{\text{ES}}^{22}$	3
E_{ES}^{12}	0
$\Gamma_1 = \Gamma_2$	$10^4, 10^5$

Table 7.1.: Parameters used for the simulations of binary systems with a species-dependent ES barrier

that the scaling is not completely accurate here: Changing T in an experiment would also change the values of the energetic parameters, since these are in units of $k_B T$).

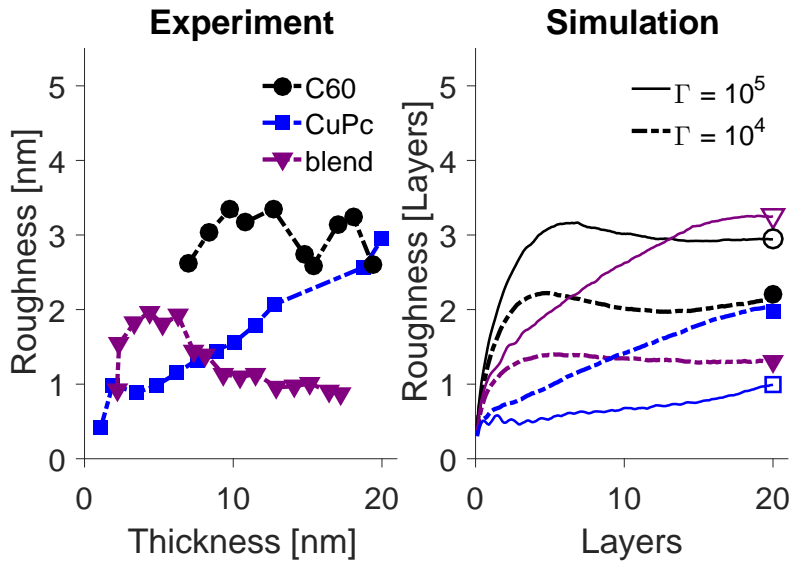


Figure 7.2.: In-situ roughness vs. layer coverage for (left) experiments (extracted from Kiessig simulations at $T = 310\text{K}$) and (right) simulations. The ratios $\Gamma = 10^4$ and 10^5 correspond to temperatures $T = 310\text{ K}$ and 400 K , respectively, while the thickness of one layer is equivalent to 0.7, 1.3, and 1 nm for C₆₀, CuPC, and the blended film, respectively. Figure by courtesy of B. Reisz.

In Fig. 7.2 we show a comparison of the roughness evolution in experiments and simulations for deposition of 20 monolayers. There we see how in the experiments, the blend film will be significantly smoother than the pure films (for C₆₀, the roughness cannot be extracted at short times due to the absence of Kiessig oscillations; see Ref. [143] for more details). The roughness evolution in the simulations for $\Gamma = 10^4$ matches the experimental ones quite well, indicating that the chosen parameters are at least adequate to properly model the roughness evolution of such mixed films.

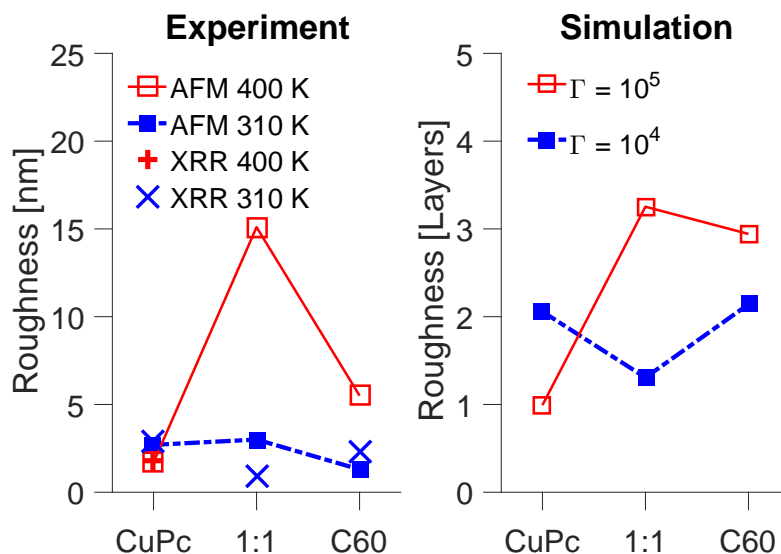


Figure 7.3.: Final film roughness after deposition of (a) 20 nm in an experiment and (b) 20 monolayers in simulations at 310 K and 400 K and $\Gamma = 10^4$ and 10^5 , respectively. Figure by courtesy of B. Reisz.

In Fig. 7.3 we compare the final film roughness after deposition of 20 monolayers. The general trend, i.e. a strong roughening in the blend at high temperature and a smoothing at low temperature, are replicated very well. Notice how:

1. XRR data are missing for C₆₀ and the blend at 400 K. This is due to the fact that here no Kiessig oscillations could be observed, which is usually a consequence of very rapid roughening.
2. The roughness extracted via atomic force microscopy (AFM) is significantly higher than the values obtained via XRR and simulations. This can be traced back to the fact that AFM measurements are performed some time after the film has stopped growing. During this time, the film will usually undergo significant morphological changes, in this case apparently very strong roughening. XRR, on the other hand, is performed during film deposition, allowing us to extract the in-situ roughness evolution. The caveat here is, however, that this method is highly sensitive.

Such results lead to the question of whether these post-growth effects could be modeled in simulations, since these effects appear to strongly influence the morphology of the resulting film.

Similarly, the island densities after deposition in Fig. 7.4 show a good qualitative match between experimental and simulation results. The method to determine the island densities was devised by B. Reisz and can be found in Ref. [143]. Quantitatively, however, the discrepancy is rather large. Assuming that one lattice site has an area of 1 nm^2 , the simulated island density would be around $9000 \mu\text{m}^{-2}$, i.e. two orders of magnitude higher than the densities measured in experiments. This is to be expected, since Γ in

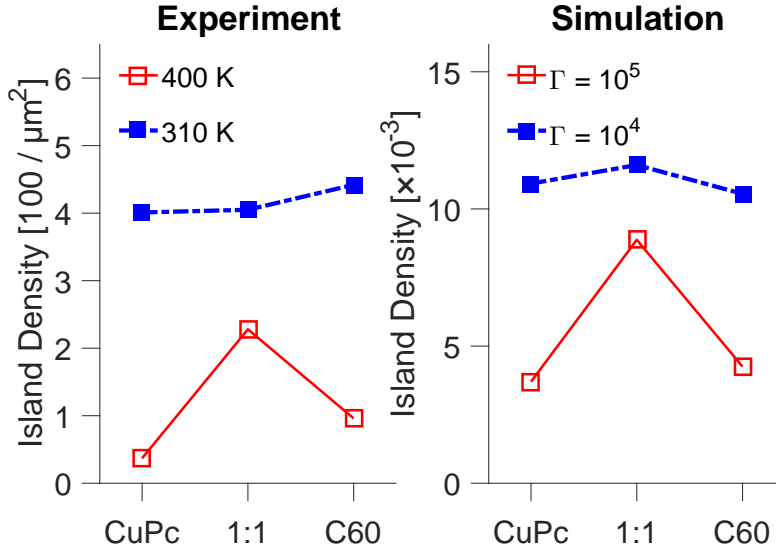
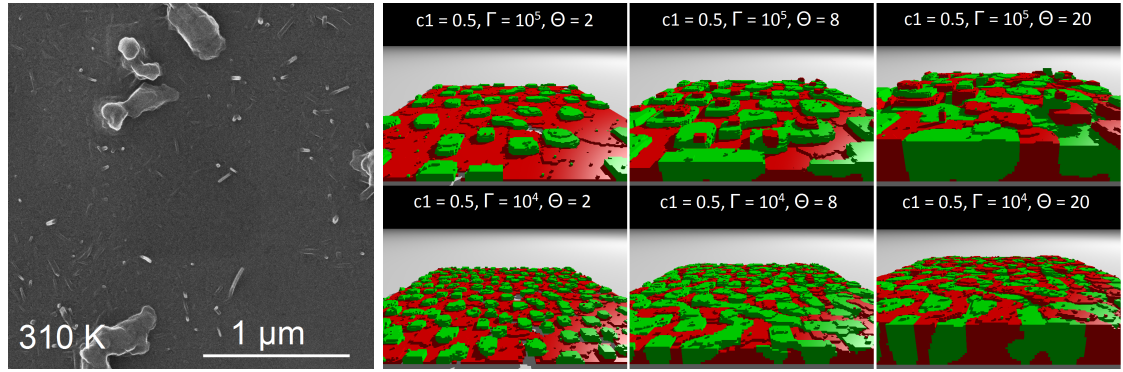


Figure 7.4.: Measured island densities after deposition in experiment and simulation. Experimental island densities were extracted using AFM. Figure by courtesy of B. Reisz.

these simulations is estimated to be 4 to 6 magnitudes lower than in experiments, and lower values of Γ lead to a higher island density (see Ch. 2.1).

In Fig. 7.5, the origin of the increased roughness and island densities for the blended film at high temperature is revealed. In the experimental HIM image, large protruding needles on top of the film are clearly visible. Similar protrusions are found in the simulations. From there we can conjecture a mechanism for the formation of these protrusions: First, species 2 will form islands on top of the wetting layer of species 1. These islands will then act as nucleation points for clusters of species 1, which in turn act as nucleation points for clusters of species 2 etc. This appears to occur due to the absence of the cross-species ES barrier.

These findings (increased roughness of the blended film at high T , increased island size in the blended film, and the formation of needles) indicate that a reduced cross-species ES barrier might indeed be the origin of certain phenomena observed. None of the aforementioned features could be produced in simulations with no or a species independent E_{ES} . However, the needles observed in experiments are thought to be composed entirely of CuPC, which cannot be accounted for using these simulations. Rather, we expect, and find, protrusions consisting of both species. In experiments, needles form due to ordering and alignment of the anisotropically shaped CuPC molecules. This cannot be mimicked using only cubic particles with isotropic interactions. Hence, a different approach seems necessary.



(a) Helium ion microscopy (HIM) image of CuPC:C₆₀ blend at 400 K. (b) Snapshots of 1:1 mixed film in simulations at different times

Figure 7.5.: Film morphology (a) after deposition of 20 nm in an experiment and (b) at $\Theta = 2, 8, 10$ in simulations, both for mixed films. Figure by courtesy of B. Reisz

7.2. Anisotropic interactions - preliminary results

In the previous section, we showed how a species-dependent E_{ES} can lead to morphologies of mixed films similar to those observed in experiments. However, the composition of such needles could not be modeled appropriately using the simple model of isotropically interacting particles. Due to this, we performed preliminary investigations of binary thin films incorporating anisotropically interacting particles. For the particle species, we chose a disc-like species growing in the LBL→3D mode (**Species 1**) and an isotropically interacting species growing in the ISL→3D mode (**Species 2**). These were again chosen in order to most faithfully model a mixture of CuPC and C₆₀. CuPC will initially show layer-by-layer growth before eventually roughening, and it is disc-shaped. C₆₀, on the other hand, will show a strong initial roughening before eventually going towards a more or less constant roughness, and its shape is more or less isotropic.

The simulation parameters are shown in Tab. 7.2. All shown values correspond to the

Parameter	Value
L	200
$\epsilon_1 = \epsilon_2$	-3
$\epsilon_{\text{sub},1}$	-4
$\epsilon_{\text{sub},2}$	-0.5
E_{ES}	0
η	3
D_{rot}	10

Table 7.2.: Parameters used for the simulations of binary systems

result of a single simulation run, respectively. The parameters were chosen guided by the results of the previous chapters, e.g. for species 1 to form needles (relatively strong η) and initial LBL growth (ϵ_{sub} relatively strong compared to ϵ) and for species 2 to initially form islands (ϵ_{sub} relatively weak compared to ϵ). Note that now $E_{\text{ES}} = 0$, in contrast to the results of the previous section. This was chosen in order to gain an initial understanding of the general behavior of such mixed films. Due to the fact that one species interacts anisotropically and one does not, there is now an anisotropy regarding the Ehrlich-Schwoebel barrier (see Sec. 6.2) in addition to the chosen values of E_{ES} .

For the diffusion constants, we investigated three combinations:

- **Set 1:** $D_1 = 10^4$, $D_2 = 10^4$
- **Set 2:** $D_1 = 10^5$, $D_2 = 10^5$
- **Set 3:** $D_1 = 10^4$, $D_2 = 10^5$

In general, one expects the film to grow smoother for larger values of D . Provided the two particle species can phase separate, a larger value of D_α will also lead to the corresponding species forming larger islands and consequently larger domains.

In Figs. 7.6, 7.7, and 7.8 we show four σ vs Θ plots for each parameter set, varying the value of ϵ' from 0 to -3 . From these plots it can be seen that upon increasing the strength of interaction between particle of different species, ϵ' , the roughness evolution of the 1:1 mixture will change, going from 3D at $\epsilon' = 0$ to ISL \rightarrow LBL at $\epsilon' = -3$. This behavior is observable in each of the three sets.

From Fig. 7.2 we find that a 1:1 mixture of CuPC and C_{60} will grow in the ISL \rightarrow LBL growth mode at 310 K, which best fits the simulation results for $\epsilon' = -3$ from e.g. Fig. 7.8(d). However, there the value of ϵ' is as strong as ϵ , which for isotropic interactions means that both particle species will show intermixing, while from experiments, it is known that CuPC and C_{60} will demix.

While the phase behavior in this four-component system is not immediately clear, the fact that the particle species intermix can be clearly seen from Fig. 7.9(a) (note that Fig. 7.9 is for parameter set 3). However, in Fig. 7.9(b) it can be seen that $\epsilon' = -2$ is already weak enough for the species to demix, while we have simultaneously chosen a value of η strong enough for the orientations of species 1 to demix. This then leads to a blended film which is smoother than the pure films of either component. Simultaneously, protrusions consisting purely of particles of species 1 form on top of the film. In App. B we show snapshots of mixed films for parameter sets 1 and 2. From these snapshots, it becomes clear that the size of these protrusions sensitively depends on the kinetic parameters of the system.

In Fig. 7.10 we show the simulated island densities after deposition for all three parameter sets. Island densities were determined as described in Ref. [143]. The pure species 2 films (isotropic particles, $c_1 = 0$) show an extremely low island density, due to the islands having coalesced into a relatively smooth film at this point, while in the pure species 1 film, the strong anisotropy means that the film will show non-equilibrium roughening and thus a large number of Z fibers. The island densities in the mixed

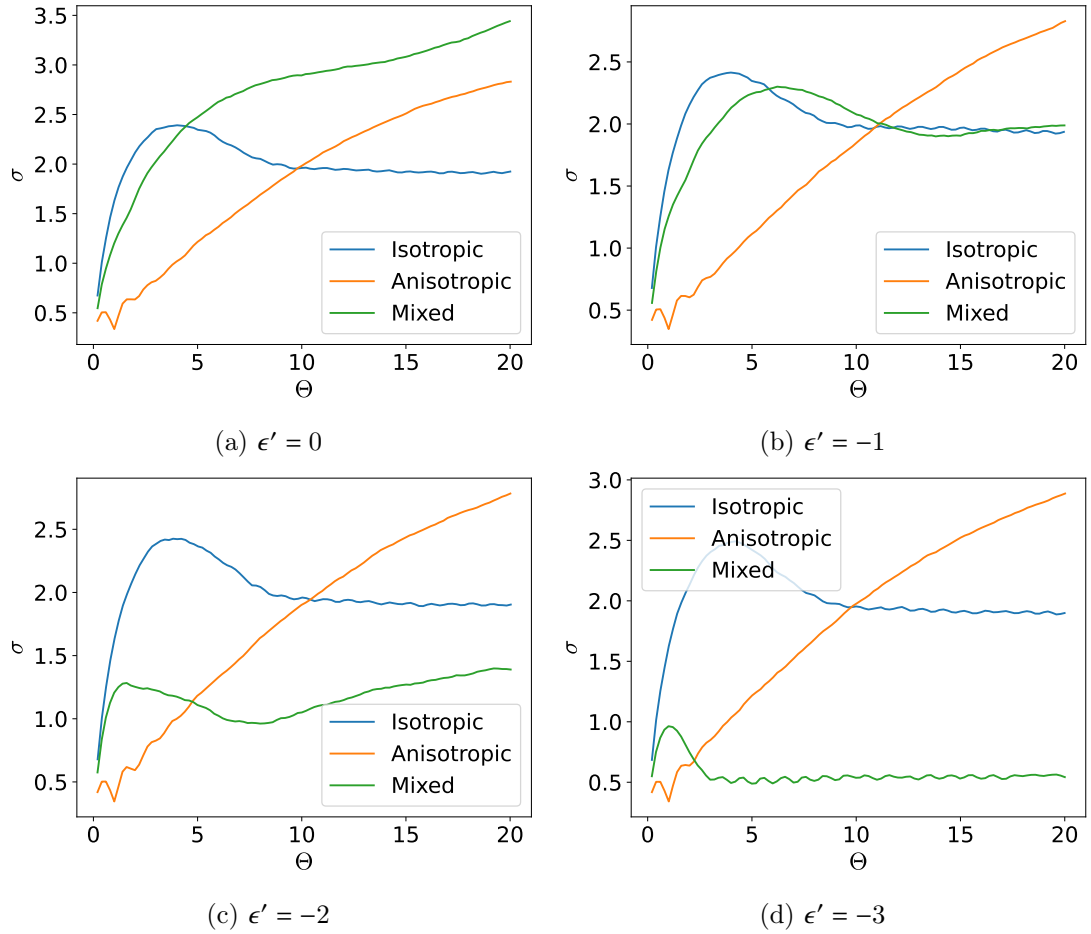


Figure 7.6.: σ vs Θ at different values of ϵ' and the parameters of set 1. Plotted are systems composed of only isotropic particles (blue), only disc-like particles (orange), and 1:1 mixtures of both (green)

films are highest at $\epsilon' = 0$ and lowest at $\epsilon' = 3$, coinciding with the decrease in film roughness seen in Figs. 7.6-7.8. For none of these parameter sets, however, we observe the significant increase in island densities for blend films found in experiments.

In the previous section, we showed that post-growth AFM studies at high temperatures found the roughness and island density for blend film grown at 400 K to be higher than those of the pure films. These values were, however, measured post-growth, allowing for re-ordering effects to significantly alter the morphology of the film after deposition. What is striking in the simulations presented here, is the formation of protrusions consisting purely of oriented particles of the disc-like species, a feature which we also suspect to occur in the co-deposition experiments.

7.2. Anisotropic interactions - preliminary results

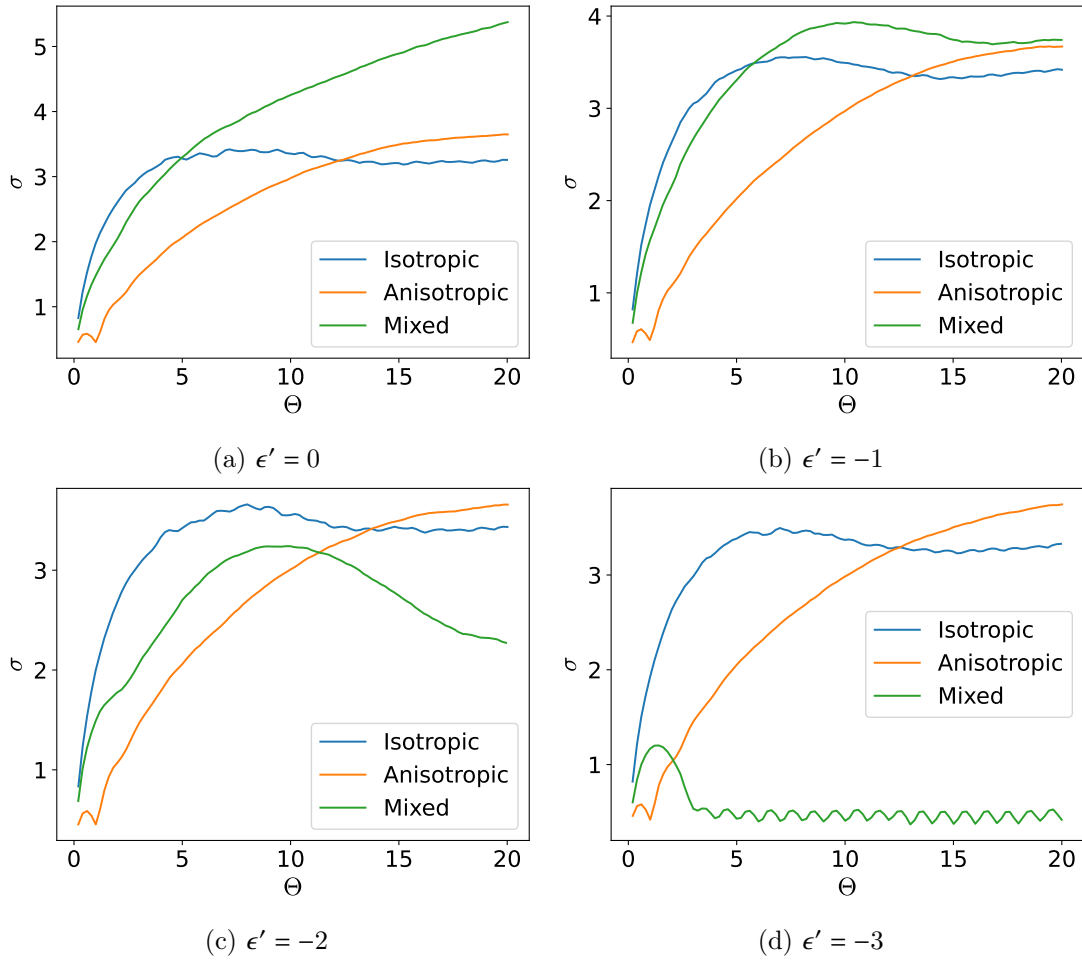


Figure 7.7.: Same as in Fig. 7.6 for set 2

Simultaneously, the fiber distributions of species A will show the effect of the particle species intermixing: In Fig. 7.11, the average length of particle fibers as well as the widths of the fiber distributions significantly decrease upon decreasing ϵ' from -2 to -3 , while for all $|\epsilon'| \leq 2$ the distributions of fiber lengths are more or less identical within each parameter set. Comparing the parameter sets, however, the influence of D_1 becomes visible. When compared to set 1 and 3 (where $D_1 = 10^4$), the average length of z fibers is significantly increased for $D_1 = 10^5$. This effect vanishes for $\epsilon' = -3$.

The fact that the mixing-demixing transition is clearly visible in the fiber distributions indicates that this observable can be used to quantitatively determine the transition point, instead of using visual inspection.

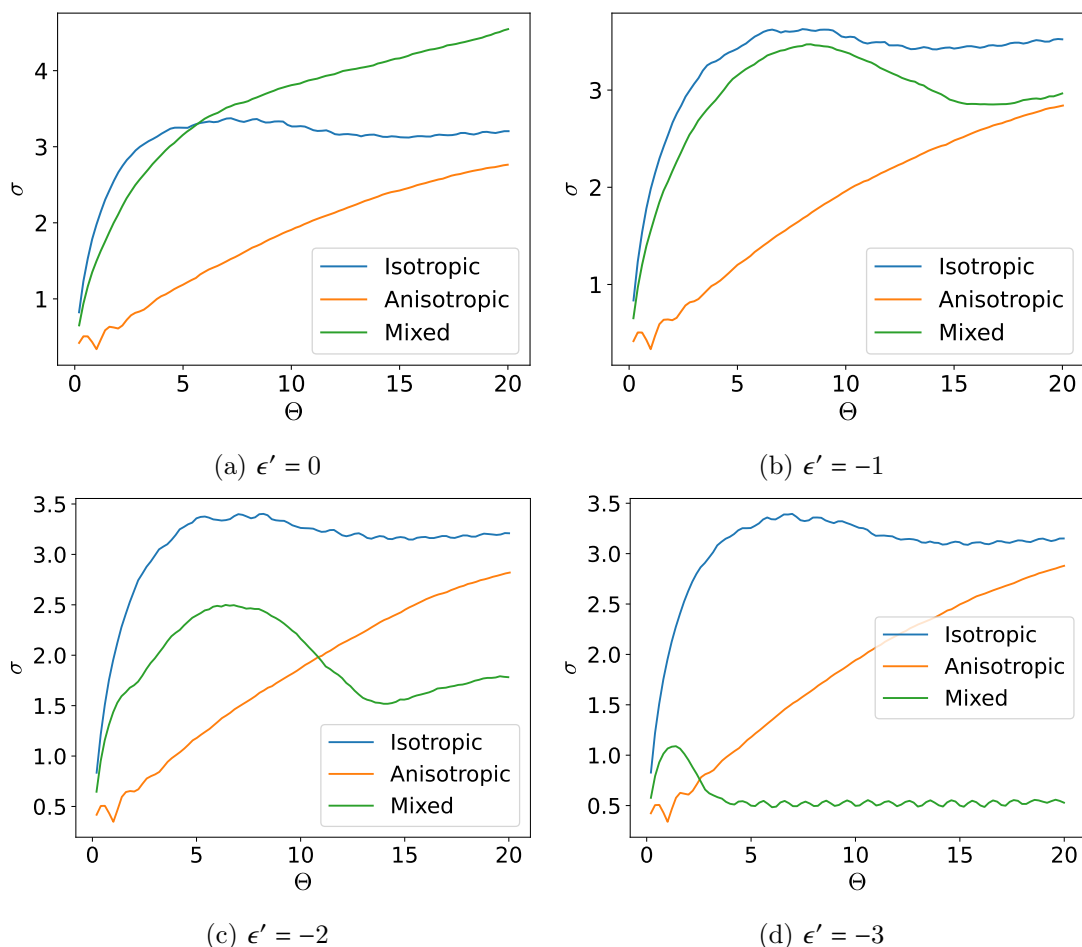


Figure 7.8.: Same as in Fig. 7.6 for set 3

7.3. Conclusions and outlook

In this chapter, we presented a preliminary investigation into the behavior of binary thin films in which one species interacts anisotropically and one does not. These films were simulated in order to gain a deeper understanding of mixed films of organic molecules, specifically mixed films of CuPC and C_{60} .

In Ref. [135], such films were grown under ambient conditions. There it was found that the 1:1 mixed film will show a significantly decreased roughness compared to pure films of the two components, and that large protrusions will form on top of the film which are thought to be comprised of CuPC needles. Additionally, it was found in earlier work that CuPC and C_{60} do not intermix.

In the simulations presented in this chapter, we have shown potential parameters which might be well-suited to simulate these films. Either of the three sets of diffusion constants leads to morphology similar to what we expect from experiments. The 1:1 mixed film

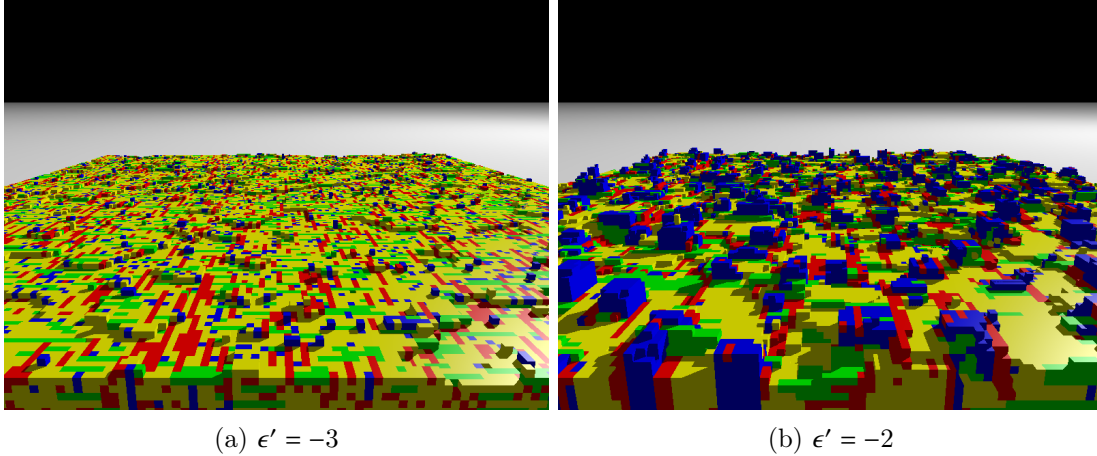


Figure 7.9.: Snapshots of a 1:1 mixture thin film after deposition of 20 monolayers at the parameters of Tab. 7.2 for **parameter set 3** at different values of ϵ' . Red, green, and blue particles are of species 1, oriented in the x , y , and z direction, respectively. Yellow particles are of species 2.

will grow more smoothly than either of the pure films if demixing is not too strong ($|\epsilon'| > 1$), while we simultaneously observe the formation of protrusions of z fibers on top of the film. For these protrusions to occur, the two particle species have to demix, which corresponds very well to experimental results where similar behavior was observed. The size of these protrusions then depends on the exact kinetic parameters. We found that the distributions of fiber lengths of species 1 provide a useful measure to determine whether the two particle species demix or not, since intermixing leads to a significant decrease in both fiber lengths and numbers.

One remaining inconsistency is the fact that from experiments, we would expect the roughness and island density of blended films compared to pure films grown at higher T (i.e. higher values of D) to be significantly increased. However, it is unclear what mechanism is at work here, since this might be the result of post-growth re-ordering.

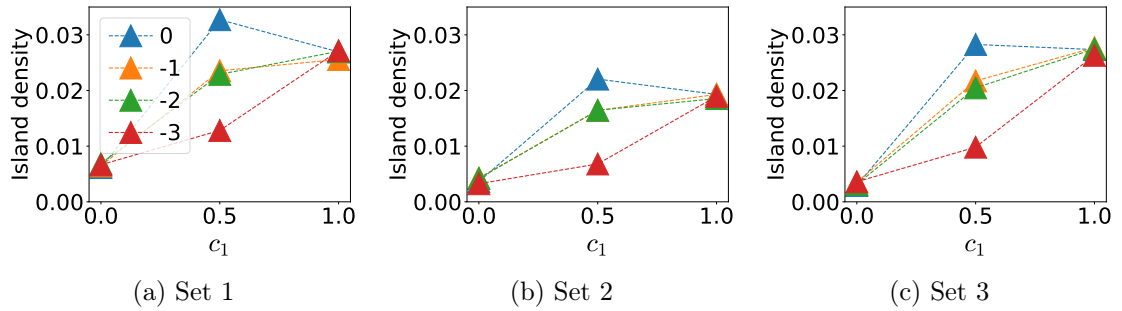


Figure 7.10.: Island densities after deposition of 20 ML vs. ratio of species 1 for all three parameter sets. Different colors denote different values of ϵ' . Increasing the strength of ϵ' decreases the island density at all parameter sets. The legend in Fig. (a) also applies to Figs. (b) and (c)

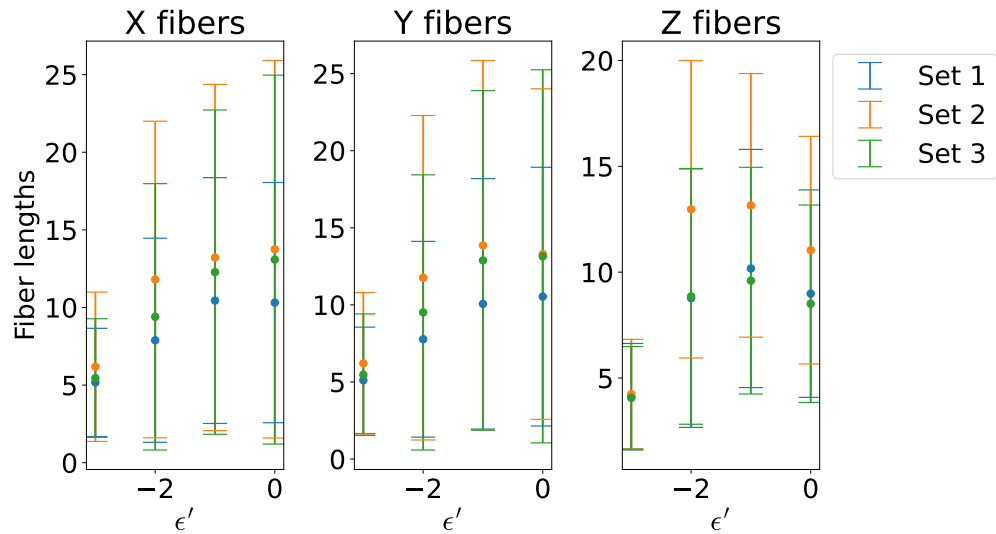


Figure 7.11.: Fiber lengths of species A in the 1:1 mixed system at different values of ϵ' . Between $\epsilon' = -2$ and -3 , a mixing transition occurs, leading to significantly shorter fibers at all parameter sets

All in all, these results indicate that simulating mixed films of an isotropically and an anisotropically interacting particle species could be a viable endeavor when trying to understand the exact mechanisms occurring during film growth in experiments. However, this entails now a large amount of parameters: ϵ_α , $\epsilon_{\text{sub},\alpha}$, D_α for each particle species, D_{rot} and η for the anisotropically interacting species, ϵ' for the inter-species interactions, and possibly an Ehrlich-Schwoebel barrier E_{ES} . Here it is necessary to use the results of Chs. 5 and 6 as guidance in finding the suitable parameters for desired behavior, as has been demonstrated in this chapter. In order to determine whether the two particle species intermix or not, the fiber distributions of species 1 can be used as guidance, since the mixing transition coincides with a significant decrease in fiber lengths and of the width of the length distribution. This method is of course preferable to visual inspection, and invites comparison to the method of measuring domain sizes as used in e.g. Ref. [32]. It would be of interest here whether a scaling relation can be found for fiber size distributions.

Of special interest here is also kinetically limited demixing behavior as found e.g. in Ref. [104]. There it was found that DIP and C_{60} , when co-deposited, will phase separate, forming domains which grow laterally in size as the distance from the substrate increases. It is speculated that this behavior is due to the kinetic nature of film growth, an assumption which could be adequately analyzed using simulations.

Chapter 8.

Outlook

Based upon the work presented in this thesis, several directions for continuing research are possible.

8.1. Rejection-free KMC

All simulations presented in this work have been performed using the so-called hybrid KMC algorithm, in which proposed moves are accepted with a probability depending on the change of internal energy they would cause.

The motivation for this choice was that in the CGM, a rejection-free implementation would be too costly, since there *in principle* each particle could be able to move at any given time (due to abolishing the solid-on-solid restriction). Since now a rich variety of moves was possible, it would make simulating this model using a rejection-free algorithm too costly.

However, in the study of anisotropic interactions we have only employed the SOS model. We did use the hybrid KMC algorithm there in order to be able to compare the results to those of the isotropic system. We suspect that in this model, either a rejection-free algorithm as e.g. used in Refs. [19, 144] or an adaptive method such as the one used in Ref. [89] would lead to a significant speed-up, allowing us to study larger systems and thicker films. This would enable us to study the long time roughness behavior, determining the roughness exponents and comparing them to other models.

8.2. No hop restrictions

In our SOS simulations, inter-layer hops were only allowed if the height difference between the sites was ≤ 1 layer. This restriction is however highly artificial and was implemented in order to inhibit unrealistically large jumps.

In Fig. 8.1 we show an example for the consequences of unrestricted hop heights in a system with anisotropic interactions. In this snapshot it is obvious that extremely high, narrow towers of z oriented particles start forming. This is due to the strong anisotropy, which leads to an effective Ehrlich-Schwoebel barrier for z particles hopping down from such a tower, while upwards hops are always energetically favorable.

A more realistic method to treat interlayer diffusion along larger steps was proposed in Ref. [145]. There, interlayer diffusion was treated as the diffusing particle performing

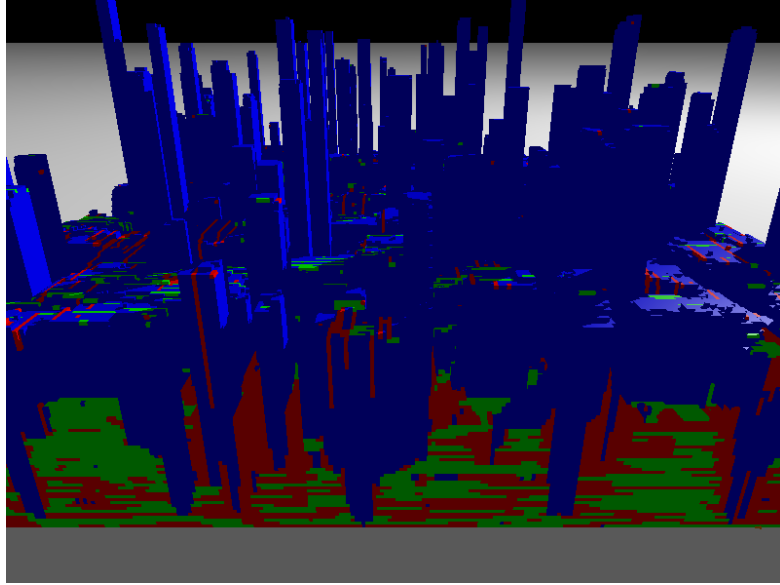


Figure 8.1.: Snapshot after deposition of 50 ML in the system with disc-like interactions and no restrictions for inter-layer hops at $\epsilon = -3, \epsilon_{\text{sub}} = -4, D = 10^4, D_{\text{rot}} = 100, \eta = 3.5$. Due to the strong anisotropy, large towers of z particles start forming.

a random walk along the side of the step. This leads to an acceptance probability of

$$P_{\text{cross}} = \frac{p}{1 + p \cdot (|\Delta h| - 1)} \quad (8.1)$$

where p is the Ehrlich-Schwobel factor $p = \exp(-E_{\text{ES}}/k_{\text{B}}T)$ and Δh the height difference between initial and target site. It is clear that for $\Delta h = 1$, this reduces to $P_{\text{cross}} = p$. For $E_{\text{ES}} = 0$, as we used in most of our simulations, this would yield

$$P_{\text{cross}} = \frac{1}{|\Delta h|} \quad (8.2)$$

The modified acceptance probability for inter-layer moves is then

$$P = P_{\text{cross}} \cdot \min(1, \exp(-\Delta E)) \quad (8.3)$$

Using this P would suppress the unrealistic mounding found in our implementation of the SOS model. It would be interesting to compare morphologies and growth modes between this model, our implementation of the SOS model, and the CGM.

8.3. Anisotropic particles

In addition to the anisotropic interactions studied in the present work, the KMC study of multilayer growth should eventually be expanded to anisotropically shaped particles in

order to capture steric effects, which can have a significant influence on the morphology evolution of a film.

Studies of anisotropically shaped particles so far have only been performed using MD and all-atom simulations for few layers[35, 146, 147, 148, 149], where the role of shape anisotropy has already been obvious: The rod-shaped particles will lie down at low coverages, but re-orient to stand up as the coverage increases, which cannot be re-created by only implementing anisotropic interactions.

As already indicated, multi-layer KMC studies of anisotropically shaped particles pose a significant challenge, however. Especially the choice of possible moves, which crucially influence the morphology, becomes more complicated. This problem might be alleviated by a combination of molecular dynamics and KMC simulations[150], where the MD simulations are performed to identify the possible moves and their respective rates, and the KMC simulation is then performed to find the behavior for thick films.

Due to the anisotropic shape of the particles, it might be impossible in such a simulation to impose the solid-on-solid restriction, meaning this would have to be simulated using the CGM.

8.4. Post-growth effects

Since film growth is a non-equilibrium process, it stands to reason that the morphology immediately after deposition might not be the final one, since there may be energetically more favorable configurations which take longer to reach.

It has indeed been found in many growth experiments[68, 151, 152, 153] that thin films will undergo significant changes in morphology after deposition, up to a timescale on the order of months later. Hence it is of great importance to understand the mechanisms guiding these re-ordering processes.

Some simulation work has been done regarding monolayer dewetting[154, 155, 156], however for thicker films an analysis is missing.

We assume such work would have to be performed using either the CGM or the SOS model with inter-layer hopping as described in Ref. [145], since restricting inter-layer hops to $|\Delta z| \leq 1$ will artificially restrict the system and inhibit possible relaxation paths (e.g. this might stop a thick film from fully dewetting from a weakly-interacting substrate).

In Fig. 8.2 we show a plot of roughness evolution in the binary system from Ch. 7. After deposition of 20 monolayers, the particle flux was shut off and existing particles were allowed to continue diffusing for a time corresponding to $\Theta = 10$. From this plot it seems that at least the roughness will not change significantly after deposition. However, a more in-depth study would be necessary to reliably confirm this suspicion.

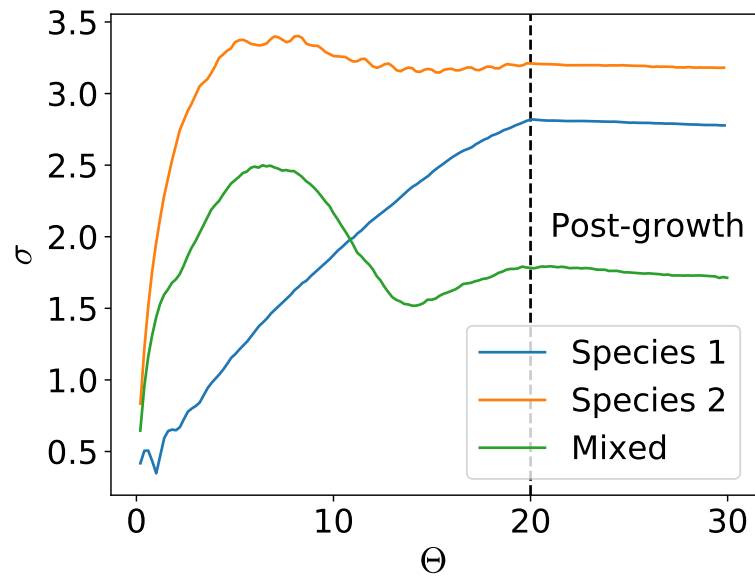


Figure 8.2.: σ vs. Θ in the binary system, for parameters, see Ch. 7. After $\Theta = 20$, no new particles are added to the system, but diffusion is still allowed. The film roughness shows no significant changes after deposition is shut off.

Apart from the ideas presented in this chapter, there is also a lot more to discover regarding structure formation in binary systems. Thus, a wide variety of possible pathways for future research exists, all of which could help in gaining a deeper understanding of structure formation during film growth.

Chapter 9.

Summary and conclusion

The simulation studies presented in this work were performed in order to understand more deeply the mechanisms governing the growth of thin films. We focused on films of intermediate thickness, since in this regime the formation of 3D structures commences. The structures formed during these stages of film growth will then in turn influence the subsequent evolution of the thin film.

We first presented a framework to analyze the roughness evolution of a film of isotropic particles growing on a substrate comprised of a different material. We found there that the roughness evolution of such films can be categorized into several modes, and were able to quantify the conditions necessary for each mode to occur. Most significantly, the transition from island to LBL growth is shifted to a lower value of ϵ_{sub} compared to the wetting transition in an equilibrium system. When comparing the standard SOS model to our newly developed colloidal growth model (in which the film is not restricted to be cavity-free), we found that both models in principle show the same behavior, with the exception of the ISL→CONST growth mode in the SOS model.

Expanding upon this, we introduced anisotropic interactions between particles in order to mimic the steric anisotropy of organic molecules. We found two ordering transitions upon increasing the anisotropy factor, an equilibrium and a non-equilibrium one. The equilibrium transition is from an unordered state to one in which all particles are oriented in parallel (perpendicular) to the substrate and is independent of the roughness evolution of the film, while the non-equilibrium transition coincides with a strong roughening of the film due to the formation of needles (sheets) perpendicular to the substrate for disk-like and rod-like interactions, respectively. We investigated these effects for weak and strong substrates, and were able to find experimental results in literature corroborating our findings.

Finally, we investigated the evolution of binary thin films. First, we studied the effect of a species-dependent hopping barrier. We found that making the interlayer hopping probability dependent on the local environment of a particle will lead to morphologies similar to those observed in blended films in experiments. Additionally, we studied the morphology of mixed films consisting of an isotropically and an anisotropically interacting species. There we found that such films can also show morphologies similar to those found in a C₆₀:CuPC blend film, offering a possible mechanism for the formation of needles in experiments.

The results presented in this thesis show that simulation of films of an intermediate thickness is a research area which has great potential to explain mechanisms of structure formation during film growth. We were able to find correspondences between our results and those found in experiments, finding e.g. possible mechanisms for needle formation in C₆₀:CuPC blend.

There are limitations regarding the interpretation of such simulation results. These systems are, after all, simplified models of reality which cannot capture many details. Most importantly, organic molecules are shaped anisotropically, while the particles used here only interact anisotropically. This steric anisotropy leads to many effects which we cannot capture using our model, but which might be relevant for structure formation (see e.g. the effects described in Ref. [149]). However, keeping these limitations in mind, such simplified models can be a useful tool for research. In a next step, this simple model could then be extended to incorporate more features of real molecules, allowing us to systematically study the effects of these.

Appendices

Appendix A.

Very strong anisotropies in model B

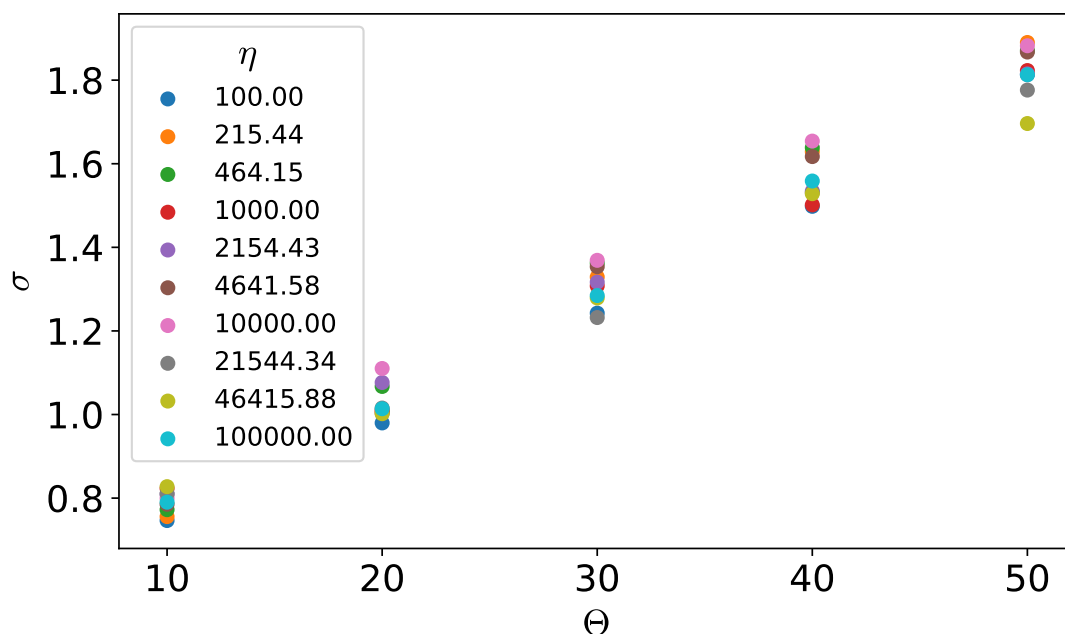


Figure A.1.: σ vs Θ for various η , $\epsilon = -3$, $\epsilon_{\text{sub}} = -4$, $D = 10^4$, $D_{\text{rot}} = 10^3$ in model B

As indicated in Ch. 6, if the kinetic parameters are high enough, the non-equilibrium transition in model B completely disappears. In Fig. A.1 we show a plot of σ vs Θ for values of η up to 10^5 . Even at these very strong anisotropies, there is no significant change in the roughness evolution. While there is an increase in roughness, the origin of this becomes clear in Fig. A.2: The bulk of the film is completely ordered in the X and Y directions and relatively smooth, but due to the restriction on inter-layer hops, scattered Z needles start forming. These are responsible for the increase in roughness. Since they are only on top of the film and will disappear when buried, this is distinct from the non-equilibrium transition described earlier.

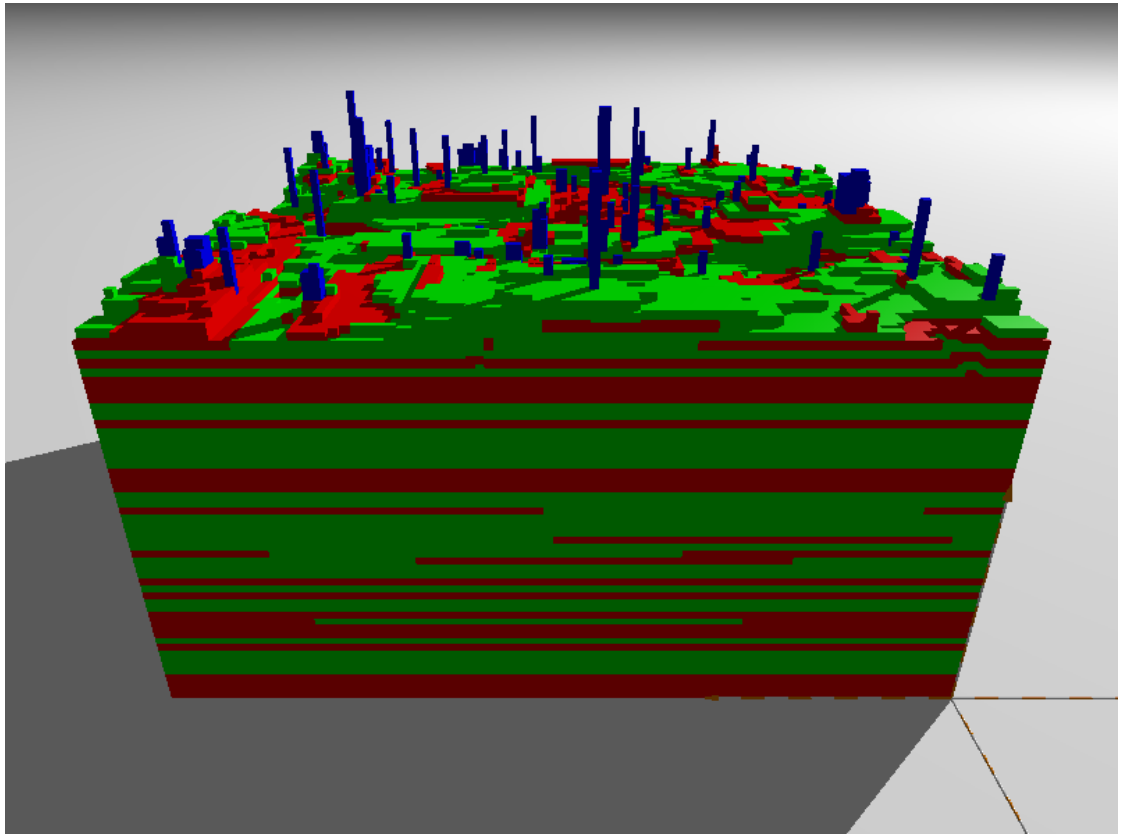


Figure A.2.: Snapshot of a film at $\eta = 10^5$ after deposition of 50 ML

Appendix B.

Binary system snapshots

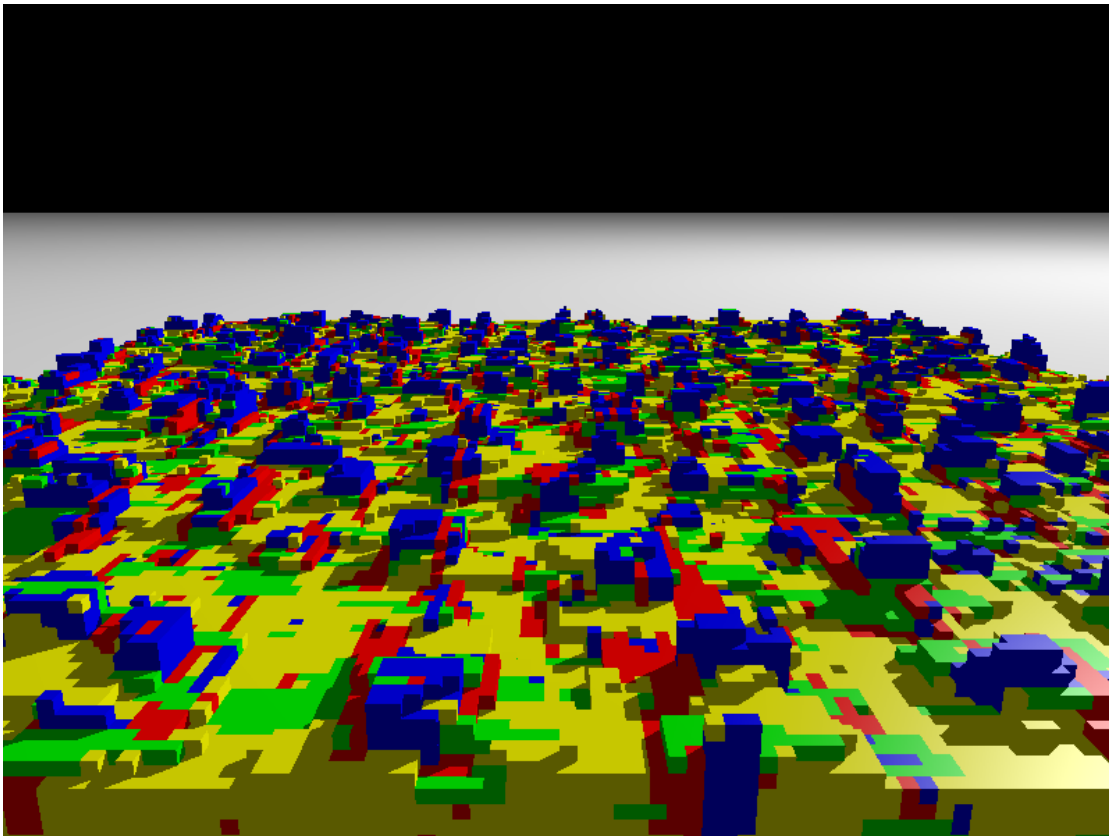


Figure B.1.: Snapshot of a 1:1 blended film after deposition of 20 monolayers for parameter set 1 from Sec. 7.2

In Figs. B.1 and B.2 we show snapshots of blend thin films after deposition of 20 ML for parameter sets 1 and 3, respectively. From these snapshots, the influence of D_α on the domain sizes becomes obvious: Larger values of D_α lead to larger domains and subsequently larger protrusions on top of the film. To illustrate this, we show in Figs. B.3-B.5 vertical slices through the film for each parameter set.

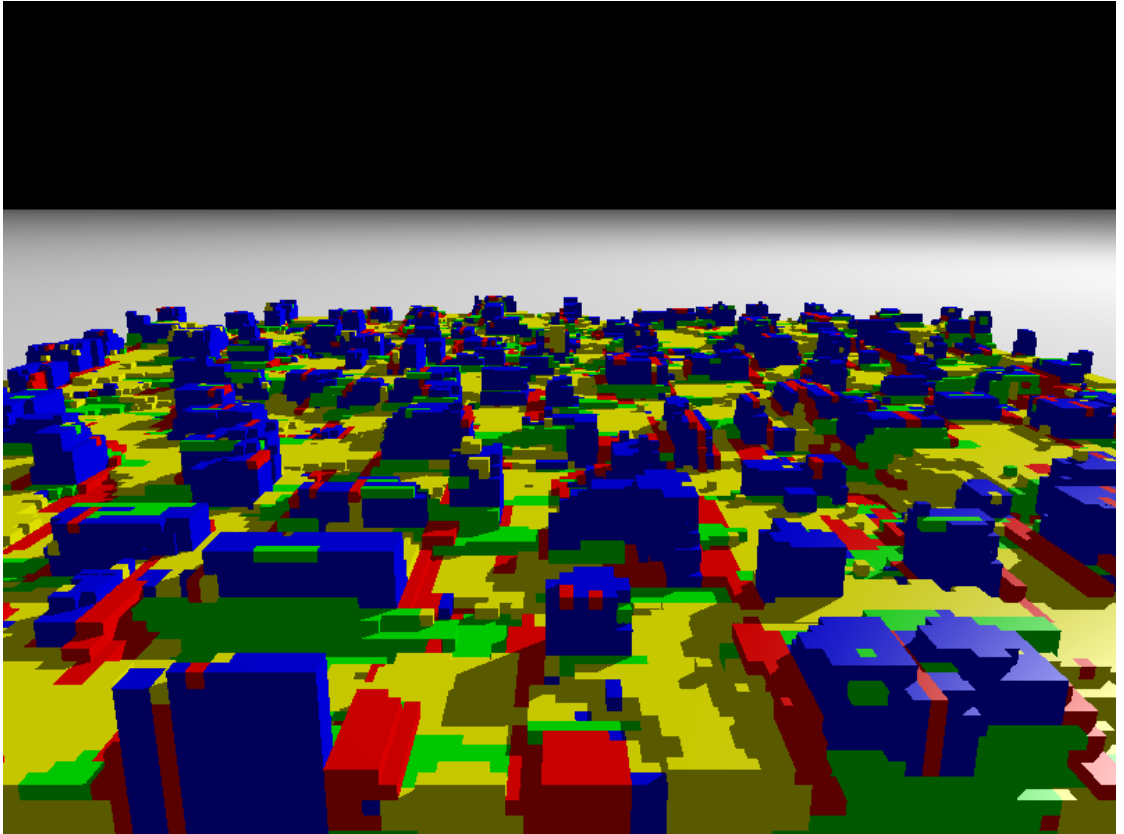


Figure B.2.: Same as Fig. B.1 but for parameter set 3

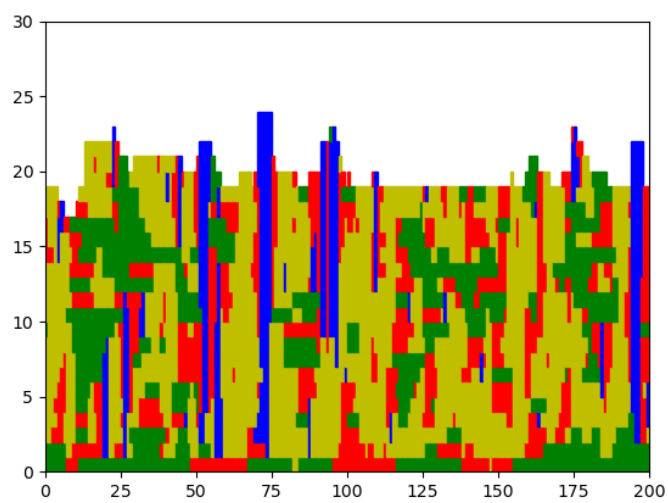


Figure B.3.: Vertical slice through a 1:1 blend after deposition of 20 monolayers for parameter set 1 from Sec. 7.2

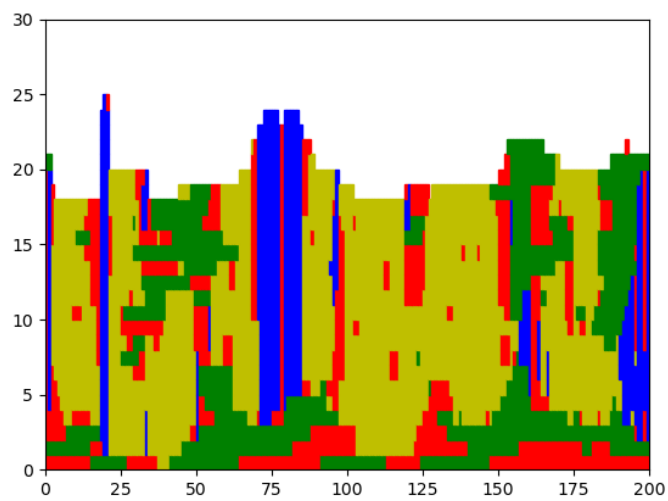


Figure B.4.: Same as Fig. B.3, but for parameter set 2

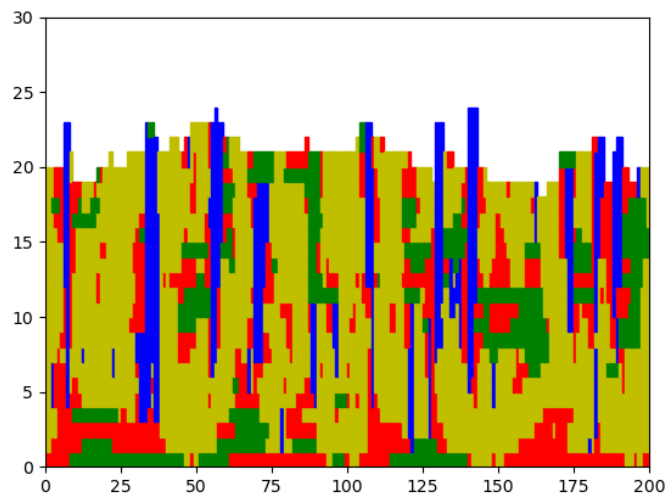


Figure B.5.: Same as Fig. B.3, but for parameter set 3

Appendix C.

Landau theory for a three-component system in 2D with an external field

As indicated in Sec. 6.4, the mean-field free energy for a three-component system on a 2D lattice where z particles interact differently from x and y particles is reminiscent of that of a three-component system with completely isotropic interactions and an applied external field. The mixing energy of such an isotropic system is:

$$\begin{aligned}\Delta E_{\text{mix}} &= -\epsilon_0(n_{xx} + n_{yy} + n_{zz}) - \epsilon'_0(n_{xy} + n_{xz} + n_{yz}) \\ &= (\epsilon_0 - \epsilon'_0)(n_{xy} + n_{xz} + n_{yz}) - 2\epsilon_0(N_x + N_y + N_z) \\ &= N(k_B T \chi(x_x x_y + x_x x_z + x_y x_z) - 2\epsilon_0)\end{aligned}$$

where $\chi \equiv \frac{z}{k_B T}(\epsilon_0 - \epsilon'_0)$. This leads to a free energy:

$$f(x_z) = \chi \left(\frac{(1-x_z)^2}{4} + x_z(1-x_z) \right) - 2\epsilon_0 + x_z \log x_z + (1-x_z) \log \left(\frac{1-x_z}{2} \right) \quad (\text{C.1})$$

Rewriting this as a function of ζ and expanding around $\zeta = 0$ up to the fourth order then yields:

$$f(\zeta) \approx \left(-2\epsilon_0 + \frac{\chi}{3} - \log(3) \right) + \left(1 - \frac{\chi}{3} \right) \zeta^2 - \frac{\zeta^3}{3} + \frac{\zeta^4}{2} \quad (\text{C.2})$$

which is identical to Eq. 6.10, apart from the factor $-2\epsilon_0$. This factor stems from the fact that the bulk energy was not subtracted here.

Appendix C. Landau theory for a three-component system in 2D with an external field

Applying an external field which specifically promotes/suppresses z particles adds another term $-h\zeta$, where h is the strength of the external field. This yields:

$$f(\zeta) \approx \left(-2\epsilon_0 + \frac{\chi}{3} - \log(3)\right) - h\zeta + \left(1 - \frac{\chi}{3}\right)\zeta^2 - \frac{\zeta^3}{3} + \frac{\zeta^4}{2} \quad (\text{C.3})$$

Eq. 6.16 had the form

$$f(\zeta) \approx -\frac{2}{9}(2\eta + 7)\epsilon - \log(3) - \frac{4}{9}(\eta - 1)\epsilon\zeta + \left(1 - \frac{10}{9}(\eta - 1)\epsilon\right)\zeta^2 - \frac{\zeta^3}{3} + \frac{\zeta^4}{2} \quad (\text{C.4})$$

which is strikingly similar.

These findings indicate that when restricting the three-component system to a 2D lattice, the anisotropic interactions act similarly to an external field proportional to χ , effectively suppressing the first order transition.

Bibliography

- [1] S. R. Forrest, “The path to ubiquitous and low-cost organic electronic appliances on plastic,” *Nature*, vol. 428, pp. 911–918, Apr 2004.
- [2] M. Eslamian, “Inorganic and organic solution-processed thin film devices,” *Nano-Micro Lett.*, vol. 9, p. 3, Sep 2016.
- [3] M. Riede, D. Spoltore, and K. Leo, “Organic solar cells—the path to commercial success,” *Adv. Energy Mater.*, vol. 11, no. 1, p. 2002653, 2021.
- [4] S.-S. Sun and N. S. Sariciftci, *Organic Photovoltaics: Mechanisms, materials, and devices*. CRC Press, 2005.
- [5] V. I. Trofimov, I. V. Trofimov, and J.-I. Kim, “Modelling of layer epitaxial growth: surface morphology and growth mode transitions,” *Comput. Mater. Sci.*, vol. 33, no. 1, pp. 362–368, 2005. Proceedings of the E-MRS 2004 Spring Meeting; Symposium H: Atomic Materials Design: Modelling and Characterization.
- [6] J. Evans, P. Thiel, and M. Bartelt, “Morphological evolution during epitaxial thin film growth: Formation of 2D islands and 3D mounds,” *Surf. Sci. Rep.*, vol. 61, no. 1-2, p. 1, 2006.
- [7] M. Pelliccione and T.-M. Lu, *Evolution of thin film morphology: Modeling and simulations*. Springer, 2008.
- [8] M. J. Vold, “Sediment volume and structure in dispersions of anisometric particles,” *J. Phys. Chem.*, vol. 63, no. 10, pp. 1608–1612, 1959.
- [9] M. J. Vold, “A numerical approach to the problem of sediment volume,” *J. Colloid Sci.*, vol. 14, no. 2, pp. 168–174, 1959.
- [10] T. Michely and J. Krug, *Islands, Mounds and Atoms: Patterns and Processes in Crystal Growth Far from Equilibrium*. Springer, 2004.
- [11] M. Eden, “A two-dimensional growth process,” in *Proceedings of the Fourth Berkeley Symposium on Mathematical Statistics and Probability: Held at the Statistical Laboratory, University of California, June 20-July 30, 1960*, vol. 2, p. 223, Univ of California Press, 1960.
- [12] P. Meakin and J. Krug, “Scaling structure in simple screening models for columnar growth,” *Phys. Rev. A*, vol. 46, no. 8, p. 4654, 1992.

Bibliography

- [13] D. E. Wolf and J. Villain, "Growth with surface diffusion," *EPL*, vol. 13, no. 5, p. 389, 1990.
- [14] S. Das Sarma and P. Tamborenea, "A new universality class for kinetic growth: One-dimensional molecular-beam epitaxy," *Phys. Rev. Lett.*, vol. 66, p. 325, 1991.
- [15] J. W. Evans, D. E. Sanders, P. A. Thiel, and A. E. Depristo, "Low-temperature epitaxial growth of thin metal films," *Phys. Rev. B*, vol. 41, no. 8, p. 5410, 1990.
- [16] K. J. Caspersen and J. W. Evans, "Metal homoepitaxial growth at very low temperatures: Lattice-gas models with restricted downward funneling," *Phys. Rev. B*, vol. 64, p. 075401, 2001.
- [17] S. Clarke and D. D. Vvedensky, "Growth kinetics and step density in reflection high-energy electron diffraction during molecular-beam epitaxy," *J. Appl. Phys.*, vol. 63, no. 7, p. 2272, 1988.
- [18] M. Siegert and M. Plischke, "Solid-on-solid models of molecular-beam epitaxy," *Phys. Rev. E*, vol. 50, p. 917, 1994.
- [19] T. A. de Assis and F. D. A. A. Reis, "Dynamic scaling and temperature effects in thin film roughening," *J. Stat. Mech.: Theory Exp.*, vol. 2015, no. 6, p. P06023, 2015.
- [20] F. F. Leal, T. J. Oliveira, and S. C. Ferreira, "Kinetic modelling of epitaxial film growth with up- and downward step barriers," *J. Stat. Mech.: Theory Exp.*, vol. P09018, 2011.
- [21] A. Baskaran, J. Devita, and P. Smereka, "Kinetic Monte Carlo simulation of strained heteroepitaxial growth with intermixing," *Contin. Mech. Thermodyn.*, vol. 22, no. 1, p. 1, 2010.
- [22] T. P. Schulze and P. Smereka, "Simulation of three-dimensional strained heteroepitaxial growth using Kinetic Monte Carlo," *Commun. Comput. Phys.*, vol. 10, no. 5, p. 1089, 2011.
- [23] T. P. Schulze and P. Smereka, "Kinetic Monte Carlo simulation of heteroepitaxial growth: Wetting layers, quantum dots, capping, and nanorings," *Phys. Rev. B*, vol. 86, p. 235313, 2012.
- [24] Y. M. Acevedo, R. A. Cantrell, P. G. Berard, D. L. Koch, and P. Clancy, "Multiscale Simulation and Modeling of Multilayer Heteroepitaxial Growth of C60 on Pentacene," *Langmuir*, vol. 32, no. 12, p. 3045, 2016.
- [25] S. J. Jiang, M. Y. Yu, Y. W. Wei, and J. J. Tang, "Monte Carlo simulation of sculptured thin films growth of SiO₂ on Si for applications," *Chinese Phys. Lett.*, vol. 25, pp. 4456–4458, 12 2008.

- [26] M. Klawtanong, C. Srinitiwara Wong, and P. Chatraphorn, “Uniformity of strained islands in heteroepitaxial thin film growth with patterned substrates: A fast kinetic Monte Carlo study,” *Thin Solid Films*, vol. 645, pp. 431–435, 1 2018.
- [27] W. Tewes, O. Buller, A. Heuer, U. Thiele, and S. V. Gurevich, “Comparing kinetic Monte Carlo and thin-film modeling of transversal instabilities of ridges on patterned substrates,” *J. Chem. Phys.*, vol. 146, 3 2017.
- [28] L. Nurminen, A. Kuronen, and K. Kaski, “Kinetic Monte Carlo simulation of nucleation on patterned substrates,” *Phys. Rev. B*, vol. 63, p. 035407, 12 2001.
- [29] S. F. Hopp and A. Heuer, “Kinetic Monte Carlo study of nucleation processes on patterned surfaces,” *J. Chem. Phys.*, vol. 133, p. 204101, 11 2010.
- [30] P. Moskovkin and S. Lucas, “Computer simulations of the early-stage growth of ge clusters at elevated temperatures on patterned Si substrate using the kinetic Monte Carlo method,” *Thin Solid Films*, vol. 536, pp. 313–317, 6 2013.
- [31] S. Dietrich, M. N. Popescu, and M. Rauscher, “Wetting on structured substrates,” *J. Phys. Condens. Matter*, vol. 17, pp. 577–593, 3 2005.
- [32] T. B. To and F. D. A. A. Reis, “Domain formation in the deposition of thin films of two-component mixtures,” *J. Alloys Compd.*, vol. 835, p. 155093, 2020.
- [33] T. Martynec and S. H. L. Klapp, “Impact of anisotropic interactions on nonequilibrium cluster growth at surfaces,” *Phys. Rev. E*, vol. 98, p. 042801, Oct 2018.
- [34] X. Zhang, Z. Zhang, and S. C. Glotzer, “Simulation study of dipole-induced self-assembly of nanocubes,” *Phys. Chem. C*, vol. 111, no. 11, pp. 4132–4137, 2007.
- [35] M. Klopotek, H. Hansen-Goos, M. Dixit, T. Schilling, F. Schreiber, and M. Oettel, “Monolayers of hard rods on planar substrates. II. Growth,” *J. Chem. Phys.*, vol. 146, no. 8, p. 084903, 2017.
- [36] K. Seshan, *Handbook of thin film deposition processes and techniques*. William Andrew Publishing, second ed., 2001.
- [37] M. Elimelech, J. Gregory, X. Jia, and R. Williams, *Particle deposition and aggregation: Measurement, modelling and Simulation*. Butterworth Heinemann, 1998.
- [38] S. Kowarik, A. Gerlach, and F. Schreiber, “Organic molecular beam deposition: fundamentals, growth dynamics, and *in situ* studies,” *J. Phys. Condens. Matter*, vol. 20, no. 18, p. 184005, 2008.
- [39] J.-P. Bucher, E. Hahn, P. Fernandez, C. Massobrio, and K. Kern, “Transition from One- to Two-Dimensional Growth of Cu on Pd(110) Promoted by Cross-Exchange Migration,” *EPL*, vol. 27, pp. 473–478, aug 1994.

Bibliography

- [40] M. Sparenberg, A. Zykov, P. Beyer, L. Pithan, C. Weber, Y. Garmshausen, F. Carlá, S. Hecht, S. Blumstengel, F. Henneberger, and S. Kowarik, “Controlling the growth mode of para-sexiphenyl (6P) on ZnO by partial fluorination,” *Phys. Chem. Chem. Phys.*, vol. 16, no. 47, p. 26084–26093, 2014.
- [41] M. Einax, W. Dieterich, and P. Maass, “Colloquium: Cluster growth on surfaces: Densities, size distributions, and morphologies,” *Rev. Mod. Phys.*, vol. 85, pp. 921–939, Jul 2013.
- [42] G. Ehrlich and F. G. Hudda, “Atomic view of surface self-diffusion: Tungsten on tungsten,” *J. Chem. Phys.*, vol. 44, no. 3, pp. 1039–1049, 1966.
- [43] R. L. Schwoebel, “Step motion on crystal surfaces. II,” *J. Appl. Phys.*, vol. 40, no. 2, pp. 614–618, 1969.
- [44] H. Eyring, “The activated complex in chemical reactions,” *J. Chem. Phys.*, vol. 3, no. 2, pp. 107–115, 1935.
- [45] C. Ratsch and M. Scheffler, “Density-functional theory calculations of hopping rates of surface diffusion,” *Phys. Rev. B*, vol. 58, pp. 13163–13166, Nov 1998.
- [46] S. Clarke and D. D. Vvedensky, “Origin of reflection high-energy electron-diffraction intensity oscillations during molecular-beam epitaxy: A computational modeling approach,” *Phys. Rev. Lett.*, vol. 58, pp. 2235–2238, May 1987.
- [47] A. Sauter, F. Roosen-Runge, F. Zhang, G. Lotze, A. Feoktystov, R. M. Jacobs, and F. Schreiber, “On the question of two-step nucleation in protein crystallization,” *Faraday discussions*, vol. 179, pp. 41–58, 2015.
- [48] V. I. Kalikmanov, *Nucleation Theory*, pp. 17–41. Dordrecht: Springer Netherlands, 2013.
- [49] C. Riccardi and H. E. Roman, eds., *Fluctuation effects in kinetic thin film growth*, p. 211–243. Research Signpost, 2008.
- [50] D. Walton, “Nucleation of vapor deposits,” *J. Chem. Phys.*, vol. 37, no. 10, pp. 2182–2188, 1962.
- [51] M. A. Herman, W. Richter, and H. Sitter, *Epitaxy: Physical principles and technical implementation*. Springer, 2004.
- [52] E. Bauer, “Phänomenologische Theorie der Kristallabscheidung an Oberflächen. I,” *Zeitschrift für Kristallographie - Crystalline Materials*, vol. 110, no. 1-6, pp. 372–394, 1958.
- [53] T. S. Chow, “Wetting of rough surfaces,” *J. Phys. Condens. Matter*, vol. 10, pp. L445–L451, jul 1998.

- [54] X. Zeng, L. Wang, L. Duan, and Y. Qiu, "Homoepitaxy growth of well-ordered rubrene thin films," *Cryst. Growth Des.*, vol. 8, pp. 1617–1622, May 2008.
- [55] V. Kalihari, D. J. Ellison, G. Haugstad, and C. D. Frisbie, "Observation of unusual homoepitaxy in ultrathin pentacene films and correlation with surface electrostatic potential," *Adv. Mater.*, vol. 21, no. 30, pp. 3092–3098, 2009.
- [56] H. Gao and W. D. Nix, "Surface roughening of heteroepitaxial thin films," *Annu. Rev. Mater. Sci.*, vol. 29, no. 1, pp. 173–209, 1999.
- [57] Z. Bao, A. J. Lovinger, and A. Dodabalapur, "Highly ordered vacuum-deposited thin films of metallophthalocyanines and their applications in field-effect transistors," *Adv. Mater.*, vol. 9, no. 1, pp. 42–44, 1997.
- [58] K. Hänel, S. Söhnchen, S. Lukas, G. Beernink, A. Birkner, T. Strunskus, G. Witte, and C. Wöll, "Organic molecular-beam deposition of perylene on Cu(110): Results from near-edge X-ray absorption spectroscopy, X-ray photoelectron spectroscopy, and atomic force microscopy," *J. Mater. Res.*, vol. 19, pp. 2049–2056, 7 2004.
- [59] P. Beyer, T. Breuer, S. Ndiaye, A. Zykov, A. Viertel, M. Gensler, J. P. Rabe, S. Hecht, G. Witte, and S. Kowarik, "Lattice matching as the determining factor for molecular tilt and multilayer growth mode of the nanographene hexa-perihexabenzocoronene," *ACS Appl. Mater. Interfaces*, vol. 6, no. 23, pp. 21484–21493, 2014.
- [60] P. Ruffieux, O. Gröning, M. Biemann, C. Simpson, K. Müllen, L. Schlapbach, and P. Gröning, "Supramolecular columns of hexabenzocoronenes on copper and gold (111) surfaces," *Phys. Rev. B*, vol. 66, p. 073409, Aug 2002.
- [61] H. Yuan, K. Gibson, D. R. Killelea, and S. Sibener, "Alignment of benzene thin films on self-assembled monolayers by surface templating," *Surf. Sci.*, vol. 609, pp. 177–182, 2013.
- [62] S. Kwon, T. G. Kim, W. K. Choi, S. O. Kang, and J. W. Kim, "Order–disorder transition in the molecular orientation during initial growth of organic thin film," *ACS Appl. Mater. Interfaces*, vol. 5, pp. 1896–1901, 3 2013.
- [63] A. Dürr, B. Nickel, V. Sharma, U. Täffner, and H. Dosch, "Observation of competing modes in the growth of diindenoperylene on SiO₂," *Thin Solid Films*, vol. 503, no. 1, pp. 127–132, 2006.
- [64] X. Zhang, E. Barrena, D. de Oteyza, and H. Dosch, "Transition from layer-by-layer to rapid roughening in the growth of DIP on SiO₂," *Surf. Sci.*, vol. 601, no. 12, pp. 2420–2425, 2007.
- [65] S. Kowarik, A. Gerlach, W. Leitenberger, J. Hu, G. Witte, C. Wöll, U. Pietsch, and F. Schreiber, "Energy-dispersive X-ray reflectivity and GID for real-time growth studies of pentacene thin films," *Thin Solid Films*, vol. 515, no. 14, p. 5606, 2007. The Ninth International Conference on Surface X-Ray and Neutron Scattering.

Bibliography

- [66] S. Kowarik, A. Gerlach, M. W. A. Skoda, S. Sellner, and F. Schreiber, “Real-time studies of thin film growth: Measurement and analysis of X-ray growth oscillations beyond the anti-Bragg point,” *Eur. Phys. J. Spec. Top.*, vol. 167, pp. 11–18, Feb 2009.
- [67] H. Zhu, Q. L. Li, X. J. She, and S. D. Wang, “Surface roughening evolution in pentacene thin film growth,” *Appl. Phys. Lett.*, vol. 98, no. 24, p. 243304, 2011.
- [68] A. C. Dürr, N. Koch, M. Kelsch, A. Rühm, J. Ghijsen, R. L. Johnson, J.-J. Pireaux, J. Schwartz, F. Schreiber, H. Dosch, and A. Kahn, “Interplay between morphology, structure, and electronic properties at diindenoperylene-gold interfaces,” *Phys. Rev. B*, vol. 68, p. 115428, Sep 2003.
- [69] J. Krug, “Origins of scale invariance in growth processes,” *Adv. Phys.*, vol. 46, no. 2, pp. 139–282, 1997.
- [70] F. Family and T. Vicsek, “Scaling of the active zone in the eden process on percolation networks and the ballistic deposition model,” *J. Phys. A: Math. Gen.*, vol. 18, pp. L75–L81, feb 1985.
- [71] M. Kardar, G. Parisi, and Y.-C. Zhang, “Dynamic scaling of growing interfaces,” *Phys. Rev. Lett.*, vol. 56, pp. 889–892, Mar 1986.
- [72] L. Bertini and G. Giacomin, “Stochastic Burgers and KPZ Equations from Particle Systems,” *Commun. Math. Phys.*, vol. 183, pp. 571–607, Feb 1997.
- [73] J. M. López, M. Castro, and R. Gallego, “Scaling of local slopes, conservation laws, and anomalous roughening in surface growth,” *Phys. Rev. Lett.*, vol. 94, p. 166103, Apr 2005.
- [74] A. F. Voter, “Introduction to the kinetic Monte Carlo method,” in *Radiation Effects in Solids* (K. E. Sickafus, E. A. Kotomin, and B. P. Uberuaga, eds.), (Dordrecht), pp. 1–23, Springer Netherlands, 2007.
- [75] S. Friedli and Y. Velenik, *Statistical Mechanics of Lattice Systems: A Concrete Mathematical Introduction*. Cambridge University Press, 2017.
- [76] Barrat, J.-L. and Vuilleumier, R., “A guide to statistical physics issues in molecular simulations,” *JDN*, vol. 12, pp. 15–30, 2011.
- [77] M. H. Kalos and P. A. Whitlock, *Monte Carlo Methods*. Wiley, 1986.
- [78] N. Metropolis, A. W. Rosenbluth, M. N. Rosenbluth, A. H. Teller, and E. Teller, “Equation of state calculations by fast computing machines,” *J. Chem. Phys.*, vol. 21, no. 6, p. 1087, 1953.
- [79] K. Binder, “Applications of Monte Carlo methods to statistical physics,” *Rep. Prog. Phys.*, vol. 60, p. 487, 5 1997.

- [80] N. Van Kampen, “Chapter IV - Markov processes,” in *Stochastic Processes in Physics and Chemistry (Third Edition)* (N. Van Kampen, ed.), North-Holland Personal Library, pp. 73–95, Amsterdam: Elsevier, third edition ed., 2007.
- [81] B. Cichocki and K. Hinsen, “Dynamic computer simulation of concentrated hard sphere suspensions: I. simulation technique and mean square displacement data,” *Phys. A: Stat. Mech. Appl.*, vol. 166, no. 3, pp. 473–491, 1990.
- [82] E. Sanz and D. Marenduzzo, “Dynamic Monte Carlo versus Brownian dynamics: A comparison for self-diffusion and crystallization in colloidal fluids,” *J. Chem. Phys.*, vol. 132, no. 19, p. 194102, 2010.
- [83] W. M. Young and E. W. Elcock, “Monte Carlo studies of vacancy migration in binary ordered alloys: I,” *Proc. Phys. Soc.*, vol. 89, pp. 735–746, nov 1966.
- [84] A. Bortz, M. Kalos, and J. Lebowitz, “A new algorithm for Monte Carlo simulation of Ising spin systems,” *J. Comput. Phys.*, vol. 17, no. 1, pp. 10–18, 1975.
- [85] W. Janke and T. Speck, “Modeling of epitaxial film growth of C₆₀ revisited,” *Phys. Rev. B*, vol. 101, p. 125427, 2020.
- [86] M. Andersen, C. Panosetti, and K. Reuter, “A Practical Guide to Surface Kinetic Monte Carlo Simulations,” *Front. Chem.*, vol. 7, 2019.
- [87] A. F. Voter, “Classically exact overlayer dynamics: Diffusion of rhodium clusters on Rh(100),” *Phys. Rev. B*, vol. 34, pp. 6819–6829, Nov 1986.
- [88] P. A. Maksym, “Fast Monte Carlo simulation of MBE growth,” *Semicond. Sci. Technol.*, vol. 3, pp. 594–596, jun 1988.
- [89] E. Adam, L. Billard, and F. Lançon, “Class of Monte Carlo algorithms for dynamic problems leads to an adaptive method,” *Phys. Rev. E*, vol. 59, no. 1, p. 1212, 1999.
- [90] L. Devroye, *Non-uniform random variate generation*. Springer-Verlag, 2013.
- [91] E. Ising, “Beitrag zur Theorie des Ferromagnetismus,” *Z. Phys.*, vol. 31, pp. 253–258, Feb 1925.
- [92] L. Onsager, “Crystal Statistics. I. a Two-Dimensional Model with an Order-Disorder Transition,” *Phys. Rev.*, vol. 65, pp. 117–149, Feb 1944.
- [93] K. Huang, *Statistical mechanics. 2. ed.* Wiley XIV, 1987.
- [94] K. Binder and D. P. Landau, “Wetting and layering in the nearest-neighbor simple-cubic Ising lattice: A Monte Carlo investigation,” *Phys. Rev. B*, vol. 37, no. 4, p. 1745, 1988.
- [95] K. Binder and D. P. Landau, “Wetting versus layering near the roughening transition in the three-dimensional Ising model,” *Phys. Rev. B*, vol. 46, p. 4844, 1992.

Bibliography

- [96] H.-O. Heuer, “Critical crossover phenomena in disordered Ising systems,” *J. Phys. A*, vol. 26, pp. L333–L339, mar 1993.
- [97] L. D. Landau, “Zur Theorie der Phasenumwandlungen I,” *Phys. Z. Sowjetunion*, vol. 11, no. 545, pp. 26–35, 1937.
- [98] E. F. Gramsbergen, L. Longa, and W. H. de Jeu, “Landau theory of the nematic-isotropic phase transition,” *Phys. Rep.*, vol. 135, no. 4, pp. 195–257, 1986.
- [99] P. J. Flory, “Thermodynamics of high polymer solutions,” *J. Chem. Phys.*, vol. 10, no. 1, pp. 51–61, 1942.
- [100] E. Empting, M. Klopotek, A. Hinderhofer, F. Schreiber, and M. Oettel, “Lattice gas study of thin-film growth scenarios and transitions between them: Role of substrate,” *Phys. Rev. E*, vol. 103, p. 023302, Feb 2021.
- [101] R. Ganapathy, M. R. Buckley, S. J. Gerbode, and I. Cohen, “Direct measurements of island growth and step-edge barriers in colloidal epitaxy,” *Science*, vol. 327, no. 5964, p. 445, 2010.
- [102] O. Auciello and A. R. Krauss, “In situ real-time characterization of thin films,” *Meas. Sci. Technol.*, vol. 13, pp. 644–644, mar 2002.
- [103] B. Voigtländer, *Atomic Force Microscopy*. Springer international, 2019.
- [104] R. Banerjee, J. Novák, C. Frank, C. Lorch, A. Hinderhofer, A. Gerlach, and F. Schreiber, “Evidence for kinetically limited thickness dependent phase separation in organic thin film blends,” *Phys. Rev. Lett.*, vol. 110, p. 185506, May 2013.
- [105] S. Bommel, N. Kleppmann, C. Weber, H. Spranger, P. Schäfer, J. Novak, S. Roth, F. Schreiber, S. Klapp, and S. Kowarik, “Unravelling the multilayer growth of the fullerene C60 in real time,” *Nat. Commun.*, vol. 5, no. 1, p. 1, 2014.
- [106] R. Cantrell and P. Clancy, “A computational study of surface diffusion of C60 on pentacene,” *Surf. Sci.*, vol. 602, no. 22, p. 3499, 2008.
- [107] L. A. Girifalco, “Molecular properties of fullerene in the gas and solid phases,” *J. Phys. Chem.*, vol. 96, no. 2, p. 858, 1992.
- [108] T. Martynec, C. Karapanagiotis, S. H. L. Klapp, and S. Kowarik, “Machine learning predictions of surface migration barriers in nucleation and non-equilibrium growth,” *Commun. Mater.*, vol. 2, p. 90, Sep 2021.
- [109] V. I. Trofimov and V. G. Mokerov, “Homoepitaxial growth kinetics in the presence of a Schwoebel barrier,” *Comput. Mater. Sci.*, vol. 17, p. 510, 2000.
- [110] E. Chason and P. R. Guduru, “Tutorial: Understanding residual stress in polycrystalline thin films through real-time measurements and physical models,” *J. Appl. Phys.*, vol. 119, no. 19, p. 191101, 2016.

- [111] C. V. Thompson, "Structure evolution during processing of polycrystalline films," *Annu. Rev. Mater. Sci.*, vol. 30, no. 1, p. 159, 2000.
- [112] J. Venables, *Introduction to surface and thin film processes*. Cambridge Univ. Press, 2006.
- [113] A. E. Lita and J. E. Sanchez, "Microstructure and surface structure evolution in alcu polycrystalline thin films," *MRS Proceedings*, vol. 562, p. 135, 1999.
- [114] A. E. Lita and J. E. Sanchez, "Effects of grain growth on dynamic surface scaling during the deposition of al polycrystalline thin films," *Phys. Rev. B*, vol. 61, p. 7692, 2000.
- [115] F. Ruffino, V. Torrisi, G. Marletta, and M. G. Grimaldi, "Growth morphology of nanoscale sputter-deposited Au films on amorphous soft polymeric substrates," *Appl. Phys. A*, vol. 103, no. 4, p. 939, 2011.
- [116] Y. Zhu, W. Wang, W. Yang, H. Wang, J. Gao, and G. Li, "Nucleation mechanism for epitaxial growth of aluminum films on sapphire substrates by molecular beam epitaxy," *Mater. Sci. Semicond. Process.*, vol. 54, p. 70, 2016.
- [117] I. Levine, A. Yoffe, A. Salomon, W. Li, Y. Feldman, and A. Vilan, "Epitaxial two dimensional aluminum films on silicon (111) by ultra-fast thermal deposition," *J. Appl. Phys.*, vol. 111, no. 12, p. 124320, 2012.
- [118] N. Mrkývková, M. Hodas, J. Hagara, P. Nadazdy, Y. Halahovets, M. Bodík, K. Tokar, J. W. Chai, S. J. Wang, D. Z. Chi, A. Chumakov, O. Konovalov, A. Hinderhofer, M. Jergel, E. Majková, P. Siffalovic, and F. Schreiber, "Diindenoperylene thin-film structure on MoS₂ monolayer," *Appl. Phys. Lett.*, vol. 114, no. 25, p. 251906, 2019.
- [119] M. Hodas, P. Siffalovic, P. Nádaždy, N. Mrkývková, M. Bodík, Y. Halahovets, G. Duva, B. Reisz, O. Konovalov, W. Ohm, M. Jergel, E. Majková, A. Gerlach, A. Hinderhofer, and F. Schreiber, "Real-Time Monitoring of Growth and Orientational Alignment of Pentacene on Epitaxial Graphene for Organic Electronics," *ACS Appl. Nano Mater.*, vol. 1, no. 6, p. 2819, 2018.
- [120] R. Ruiz, D. Choudhary, B. Nickel, T. Toccoli, K.-C. Chang, A. C. Mayer, P. Clancy, J. M. Blakely, R. L. Headrick, S. Iannotta, and G. G. Malliaras, "Pentacene Thin Film Growth," *Chem. Mater.*, vol. 16, no. 23, p. 4497, 2004.
- [121] T. V. Desai, E. R. Kish, A. R. Woll, and J. R. Engstrom, "Hyperthermal Growth of N,N'-Ditridecylperylene-3,4,9,10-tetracarboxylic Diimide on Self-Assembled Monolayers: Adsorption Dynamics and Sub- and Multilayer Thin Film Growth," *J. Phys. Chem. C*, vol. 115, no. 37, p. 18221, 2011.

Bibliography

- [122] A. Zykov, S. Bommel, C. Wolf, L. Pithan, C. Weber, P. Beyer, G. Santoro, J. P. Rabe, and S. Kowarik, "Diffusion and nucleation in multilayer growth of PTCDI-C8 studied with in situ X-ray growth oscillations and real-time small angle X-ray scattering," *J. Chem. Phys.*, vol. 146, no. 5, p. 052803, 2017.
- [123] S. Kowarik, A. Gerlach, S. Sellner, F. Schreiber, J. Pflaum, L. Cavalcanti, and O. Konovalov, "Anomalous roughness evolution of rubrene thin films observed in real time during growth," *Phys. Chem. Chem. Phys.*, vol. 8, p. 1834, 2006.
- [124] R. K. Nahm, H. J. Bullen, T. Suh, and J. R. Engstrom, "Faster is smoother and so is lower temperature: The curious case of thin film growth of tetracene on SiO," *J. Phys. Chem. C*, vol. 121, no. 15, p. 8464, 2017.
- [125] J. Shi and X. R. Qin, "Flux dependence of the morphology of a tetracene film on hydrogen-passivated Si(100)," *Phys. Rev. B*, vol. 73, p. 121303, 2006.
- [126] M. A. Fusella, F. Schreiber, K. Abbasi, J. J. Kim, A. L. Briseno, and B. P. Rand, "Homoeptaxy of crystalline rubrene thin films," *Nano Lett.*, vol. 17, no. 5, p. 3040, 2017.
- [127] A. Gerlach, S. Sellner, S. Kowarik, and F. Schreiber, "In-situ X-ray scattering studies of OFET interfaces," *Phys. Status Solidi (a)*, vol. 205, no. 3, pp. 461–474, 2008.
- [128] S. Chiodini, A. Straub, S. Donati, C. Albonetti, F. Borgatti, P. Stoliar, M. Murgia, and F. Biscarini, "Morphological transitions in organic ultrathin film growth imaged by in situ step-by-step atomic force microscopy," *J. Phys. Chem. C*, vol. 124, no. 25, p. 14030, 2020.
- [129] E. Empting, N. Bader, and M. Oettel, "Interplay of orientational order and roughness in simulated thin film growth of anisotropically interacting particles," *Phys. Rev. E*, vol. 105, p. 045306, Apr 2022.
- [130] D. Choudhary, P. Clancy, R. Shetty, and F. Escobedo, "A computational study of the sub-monolayer growth of pentacene," *Adv. Func. Mat.*, vol. 16, no. 13, p. 1768, 2006.
- [131] M. A. Bates, "Computer simulation study of the phase behavior of a nematogenic lattice-gas model," *Phys. Rev. E*, vol. 64, p. 051702, Oct 2001.
- [132] P. Quiring, M. Klopotek, and M. Oettel, "Nematic and gas-liquid transitions for sticky rods on square and cubic lattices," *Phys. Rev. E*, vol. 100, p. 012707, Jul 2019.
- [133] Z. Ma, H. Geng, D. Wang, and Z. Shuai, "Influence of alkyl side-chain length on the carrier mobility in organic semiconductors: Herringbone vs. pi-pi stacking," *J. Mater. Chem. C*, vol. 4, no. 20, p. 4546–4555, 2016.

- [134] K. Ishii, H. Nakayama, T. Yoshida, H. Usui, and K. Koyama, “Amorphous state of vacuum-deposited benzene and its crystallization,” *Bull. Chem. Soc. Jpn.*, vol. 69, no. 10, pp. 2831–2838, 1996.
- [135] B. Reisz, E. Empting, M. Zwadlo, M. Hodas, G. Duva, V. Belova, C. Zeiser, J. Hagenlocher, S. Maiti, A. Hinderhofer, A. Gerlach, M. Oettel, and F. Schreiber, “Thin film growth of phase-separating phthalocyanine-fullerene blends: A combined experimental and computational study,” *Phys. Rev. Mater.*, vol. 5, p. 045601, Apr 2021.
- [136] J. Yang, S. Yim, and T. S. Jones, “Molecular-orientation-induced rapid roughening and morphology transition in organic semiconductor thin-film growth,” *Sci. Rep.*, vol. 5, p. 9441, Mar 2015.
- [137] S. Kowarik, A. Gerlach, W. Leitenberger, J. Hu, G. Witte, C. Wöll, U. Pietsch, and F. Schreiber, “Energy-dispersive X-ray reflectivity and GID for real-time growth studies of pentacene thin films,” *Thin Solid Films*, vol. 515, no. 14, pp. 5606–5610, 2007.
- [138] A. Hinderhofer, C. Frank, T. Hosokai, A. Resta, A. Gerlach, and F. Schreiber, “Structure and morphology of coevaporated pentacene-perfluoropentacene thin films,” *J. Chem. Phys.*, vol. 134, no. 10, p. 104702, 2011.
- [139] B. Reisz, S. Weimer, R. Banerjee, C. Zeiser, C. Lorch, G. Duva, J. Dieterle, K. Yonezawa, J.-P. Yang, N. Ueno, and et al., “Structural, optical, and electronic characterization of perfluorinated sexithiophene films and mixed films with sexithiophene,” *J. Mater. Res.*, vol. 32, no. 10, p. 1908–1920, 2017.
- [140] R. Banerjee, A. Hinderhofer, M. Weinmann, B. Reisz, C. Lorch, A. Gerlach, M. Oettel, and F. Schreiber, “Interrupted growth to manipulate phase separation in DIP:C60 organic semiconductor blends,” *J. Phys. Chem. C*, vol. 122, no. 3, pp. 1839–1845, 2018.
- [141] C. Lorch, J. Novák, R. Banerjee, S. Weimer, J. Dieterle, C. Frank, A. Hinderhofer, A. Gerlach, F. Carla, and F. Schreiber, “Influence of C60 co-deposition on the growth kinetics of diindenoperylene—from rapid roughening to layer-by-layer growth in blended organic films,” *J. Chem. Phys.*, vol. 146, no. 5, p. 052807, 2017.
- [142] A. Hinderhofer and F. Schreiber, “Organic–organic heterostructures: Concepts and applications,” *Chem. Phys. Chem.*, vol. 13, no. 3, pp. 628–643, 2012.
- [143] B. Reisz, *Structure Formation during Organic Molecular Beam Deposition*. PhD thesis, Universität Tübingen, 2021.
- [144] T. B. To, R. Almeida, S. O. Ferreira, and F. D. Aarão Reis, “Roughness and correlations in the transition from island to film growth: Simulations and application to cdte deposition,” *Appl. Surf. Sci.*, vol. 560, p. 149946, 2021.

Bibliography

- [145] F. F. Leal, S. C. Ferreira, and S. O. Ferreira, “Modelling of epitaxial film growth with an Ehrlich–Schwoebel barrier dependent on the step height,” *J. Phys. Condens. Matter*, vol. 23, no. 29, p. 292201, 2011.
- [146] L. Muccioli, G. D’Avino, and C. Zannoni, “Simulation of vapor-phase deposition and growth of a pentacene thin film on C60 (001),” *Adv. Mater.*, vol. 23, no. 39, p. 4532, 2011.
- [147] O. M. Roscioni, G. D’Avino, L. Muccioli, and C. Zannoni, “Pentacene crystal growth on silica and layer-dependent step-edge barrier from atomistic simulations,” *J. Phys. Chem. Lett.*, vol. 9, no. 23, p. 6900, 2018.
- [148] S. Chiodini, G. D’Avino, L. Muccioli, L. Bartolini, D. Gentili, S. Toffanin, and C. Albonetti, “Self-organization of complete organic monolayers via sequential post-deposition annealing,” *Prog. Org. Coat.*, vol. 138, p. 105408, 2020.
- [149] M. Miletic, K. Palczynski, and J. Dzubiella, “Influence of partial fluorination on growth modes of organic molecules on amorphous silicon dioxide,” *Phys. Rev. Mat.*, vol. 6, p. 033403, Mar 2022.
- [150] E. C. Neyts and A. Bogaerts, “Combining molecular dynamics with Monte Carlo simulations: implementations and applications,” *Theor. Chem. Acc.*, vol. 132, p. 1320, Dec 2012.
- [151] A. C. Dürr, F. Schreiber, K. A. Ritley, V. Kruppa, J. Krug, H. Dosch, and B. Struth, “Rapid roughening in thin film growth of an organic semiconductor (diindenoperylene),” *Phys. Rev. Lett.*, vol. 90, no. 1, p. 016104, 2003.
- [152] B. Krause, A. Dürr, F. Schreiber, H. Dosch, and O. Seeck, “Late growth stages and post-growth diffusion in organic epitaxy: PTCDA on Ag(111),” *Surf. Sci.*, vol. 572, no. 2, pp. 385–395, 2004.
- [153] A. Hinderhofer, T. Hosokai, K. Yonezawa, A. Gerlach, K. Kato, K. Broch, C. Frank, J. Novák, S. Kera, N. Ueno, and F. Schreiber, “Post-growth surface smoothing of thin films of diindenoperylene,” *Appl. Phys. Lett.*, vol. 101, no. 3, p. 033307, 2012.
- [154] O. Pierre-Louis, A. Chame, and Y. Saito, “Dewetting of a solid monolayer,” *Phys. Rev. Lett.*, vol. 99, p. 136101, 2007.
- [155] O. Pierre-Louis, A. Chame, and M. Dufay, “Atomic step motion during the dewetting of ultra-thin films,” *Eur. Phys. J. B*, vol. 77, no. 1, p. 57, 2010.
- [156] A. Chame, Y. Saito, and O. Pierre-Louis, “Orientation and morphology of solid-state dewetting holes,” *Phys. Rev. Mat.*, vol. 4, p. 094006, Sep 2020.

Acknowledgments

Firstly, I want to express my deepest gratitude to my supervisor Prof. Martin Oettel for allowing me to pursue this PhD and for his advice and support during my PhD study. It has been an extremely interesting time, during which I learned a lot and could always count on his advice and expertise.

I would also like to thank my second supervisor, Prof. Frank Schreiber, for his many helpful comments and insights regarding my research, as well as his group members Alexander Hinderhofer and Berthold Reisz for the fruitful collaboration on several projects.

Special thanks go to Miriam Klopotek for her help and guidance during the work for my master's thesis and PhD research. I also thank my other (former) colleagues, especially Frank, Michael, Alessandro, Paul, Sam, and Malte, for helpful comments during the writing of this thesis and a very pleasant work environment during these last four years.

Finally, I want to thank my friends, family and my partner Franzi for their support through all these years in Tübingen.